UNIVERSITY OF SOUTHAMPTON

DEPARTMENT OF PHYSICS AND ASTRONOMY

Quantum, Light & Matter

Integrated sources and detectors of nonclassical states of light in Silicon Nitride

by

Robert Cernansky

Thesis for the degree of Doctor of Philosophy

August 2019

UNIVERSITY OF SOUTHAMPTON

ABSTRACT

DEPARTMENT OF PHYSICS AND ASTRONOMY
Quantum, Light & Matter

Doctor of Philosophy

INTEGRATED SOURCES AND DETECTORS OF NONCLASSICAL STATES OF LIGHT IN SILICON NITRIDE

by Robert Cernansky

The work presented in this thesis aims to integrate sources and detectors of nonclassical states of light into a single photonic chip. Correlated pairs of single photons are among the most used sources in many quantum optics and quantum information experiments but their integration with detectors still remains a challenging task. In the first part of the thesis we exploit the generation of correlated pairs of photons in the visible spectrum using an integrated Silicon Nitride microring resonator. As the fabrication process of our sources is fully compatible with back-end CMOS technology, we also discuss the unique possibility of integration with silicon avalanche photodectors to provide a platform for commercially available, fully integrated, analogue quantum simulator working at room temperature. The drawback of universal quantum computation with single photons is its probabilistic nature that increases the technological complexity to obtain complete on chip integration of all necessary components to prepare, manipulate and measure quantum states of light. On the other hand, quantum information processing with continuous variables is completely deterministic. Therefore, in the second part of this work we report design, fabrication and experimental verification of an integrated source of broadband squeezed state of light on a photonic chip. We numerically investigate the amount of obtained squeezing and spurious noise that prevents us to observe shot noise reduction at short sideband frequencies. Additionally, we propose a design to extend our work towards hybridization with discrete variables to obtain qubits that can be protected against errors.

Contents

List of Figures

List of Tables

Declaration of Authorship

I, Robert Cernansky , declare that the thesis entitled *Integrated sources and detectors of nonclassical states of light in Silicon Nitride* and the work presented in the thesis are both my own, and have been generated by me as the result of my own original research. I confirm that:

- this work was done wholly or mainly while in candidature for a research degree at this University;
- where any part of this thesis has previously been submitted for a degree or any other qualification at this University or any other institution, this has been clearly stated;
- where I have consulted the published work of others, this is always clearly attributed;
- where I have quoted from the work of others, the source is always given. With the exception of such quotations, this thesis is entirely my own work;
- I have acknowledged all main sources of help;
- where the thesis is based on work done by myself jointly with others, I have made clear exactly what was done by others and what I have contributed myself;
- parts of this work have been published as: [8]

Signed:.....

Date:.....

Acknowledgements

Completing a PhD degree was probably the most challenging goal in my life that I decided to go through. The level of mental challenge that one has to surpass is quite astonishing and requires a strong mind and a lot of support from surrounding people. Therefore, I could not thank enough to my supervisor Alberto Politi, for his invaluable support and guidance along the way that can be considered far beyond a standart supervision. He gave me the opportunity to undergo the most intense training process to learn new scientific skills and abilities. That also gave me the possibility to explore my intellectual limits of understanding nature. His discussions are an invaluable knowledge that I will carry on in my mind for a long time. I am very grateful to our group members ,big Francesco, Ioannis and little Francesco for all the work that we have done together as a team. Especially I can not thank enough to big Francesco for his support during the first two years of my PhD and the invaluable help in the beginnings of my cleanroom work. The never ending arguments we pursued, will always form a great memory to remember.

During my studies I had the opportunity to collaborate with Simone De Liberato, Stefan Maier, Jonathan Matthews, Roberto Leoni, Harold Chong and many other great scientific minds in their field of research. Furthermore, working in a such a complex enviroment as the Southampton Nanofabrication center, I have the need to thank all the technical staff starting from Zondy, Kian, Mike, Owain, Libe and more for their knowledge and help during my work in the cleanroom. There are many more people I have the need to thank for keeping my sanity in order. First of all, I have to thank Rafidah for being my cleanroom buddy after Francesco left. I must thank Ali for always making me laugh with his never ending enthusiasm. Giacomo, Orestis and Vaggelis for being the best housemates one can imagine. The tsipouro nights are surely unforgettable. I would also like to thank the whole "Pavlos" group for always have the possibility to join them for a coffe, lunch or dinner. I also have to thank Pavlos himself for his support during the last six months of my PhD. I would like to thank Mirko, Michal and the whole department of Optics at Palacky University for the support and education that prepared me for this incredible journey.

Finally, I can not forget to thank my family for always being there for me. Whether I would fail or succeed in life they would always support me no matter what. Especially, my parents Alena and Jozef who always listened to my problems and whenever I came back home to Slovakia for holidays, they made clear that my happiness is always their priority. I surely could not do it without them.

List of Publications

Peer-reviewed journal articles

(1) **R. Cernansky**, F. Martini, A. Politi. "Complementary metal-oxide semiconductor compatible source of single photons at near-visible wavelengths". *Optics Letters*, 43, 4, February 2018

(2) I. Razdolski, N. Ch. Passler, Ch. R. Gubbin, Ch. J. Winta, **R. Cernansky**, F. Martini, A. Politi, S. A. Maier, M. Wolf, A. Paarmann, and S. De Liberato. "Second harmonic generation from strongly coupled localized and propagating phonon-polariton modes". *Physical Review B*, 98, 125425 , September 2018

(3) R. Petra, S. Z. Oo, A. Tarazona, **R. Cernansky**, S. Reynolds, A. Z. Khokhar, V. Mittal, D. J. Thomson, A. Politi, G. Z. Mashanovich, G. T. Reed, and H. M. H. Chong. "HWCVD a-Si:H Interlayer Slope Waveguide Coupler for Multilayer Silicon Photonics Platform". *Optics Express*, in press 2019

Manuscripts under review

(4) A. Gaggero, F. Martini, F. Mattioli, F. Chiarello, **R. Cernansky**, A. Politi, R. Leoni. "Amplitude-Multiplexed readout of single photon detectors based on superconducting nanowires". *arXiv:1811.12306*, November 2018

(5) I. Chatzopoulos, F. Martini, **R. Cernansky** and A. Politi. "High-Q/V two-dimensional photonic crystal cavities in 3C-SiC". *arXiv:1812.01548*, December 2018

Chapter 1

Quantum Technologies: An Overview

In 1965 the co-founder of Intel Gordon Moore predicted that the number of transistors on a single silicon chip would double every year per an integrated circuit [9]. After ten years he modified the prediction of the doubling process as a two year trend. As the increased integration is given by the reduction of transistors size, researchers estimated that the end of an silicon era would come at some point between the first 20-25 years of the new millennium. At that point quantum mechanics was well understood and scientists knew that pushing the size of the transistor technology to a 5 nm scale would result to a break of classical theories that did govern the computational mechanics of classical computers. Therefore, over the past several decades, quantum information science has emerged to seek answers to the question: Is there a way to store, transmit and encode information into quantum systems that would process information dictated by the rules of quantum mechanics? The answer is, Yes.

1.0.1 Computational complexity

A classical deterministic computer (Turing machine) addresses specific set of mathematical problems that can be efficiently solved in polynomial time. These types of problems fall within P-class of complexity. Unfortunately, it is not known whether having the same amount of resources a universal quantum computer (UQC) can solve the same type of problems much more efficiently (exponentially). But, assuming a strong believe among computer scientists of

$$P \neq NP(?), \tag{1.1}$$

where NP are class of problems whose solutions can be checked by a classical Turing machine within a polynomial time, the UQC can address some (not all) problems which

are strongly believed to be outside of the P complexity. Factorizing big numbers, optimizing a mathematical path, graph isomorphism, solving sets of linear equations and simulating quantum systems are important numerical problems with high impact applications that are known to be solved efficiently using a UQC while there are (so far) no known algorithms to obtain a polynomial solution using a classical Turing machine. These problems belong to a class of called the BQP (bounded error, quantum, polynomial time), whose boundaries in the complexity space is not well understood, shown in Fig. 1.1. It is defined as the set of problems solvable with a polynomial time using a quantum algorithm, where a bounded probability of error is allowed. Thus, a quantum computer is said to "solve" a problem if, for every instance, its answer will be right with high probability. Overall, it is important to remind us that because of the unknown boundaries of individual complexity classes, the ultimate computational power of UQC is not well understood, yet.

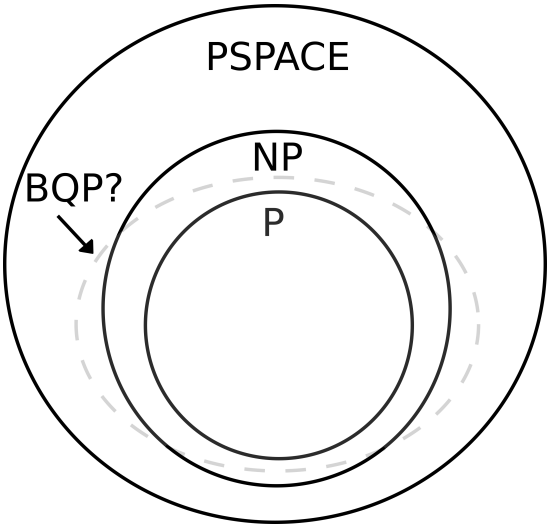

Figure 1.1: Diagram of computational complexity [1]. For the purpose of this thesis we do not need to define the PSPACE. It is only used for illustration of the complexity diagram.

1.0.2 Quantum computation

The fundamental concept behind classical and quantum computation is an idea of a bit of information which we assign a logical state. In classical computation a bit of information is an abstract mathematical object represented by 0's and 1's. Its physical interpretation is realized for example by measuring the current that flows in a copper wire of a transistor. When the measured voltage is above 5V the result is represented by logical state 1 (True) otherwise its logical state is 0 (False). In similar sense there is a quantum mechanical counterpart of a classical bit called quantum bit or "qubit". The difference between a bit and a qubit is that the logical state can be not just 0 or 1 but

any linear combination of states called "superposition"

$$|\psi\rangle = \alpha|0\rangle + \beta|1\rangle, \tag{1.2}$$

where α and β are complex numbers which upon a measurement have to fulfil a well known condition $|\alpha|^2+|\beta|^2 = 1$. This means that the measurement result of a single qubit is probabilistic. In other way, $|\psi\rangle$ is a vector in a two-dimensional complex vector space, called Hilbert space, where $|0\rangle$,$|1\rangle$ form an orthonormal basis. A useful interpretation about qubits is the following geometrical representation. Since, $|\alpha|^2 + |\beta|^2 = 1$ we can rewrite Eq. 1.2 as

$$|\psi\rangle = \cos\frac{\theta}{2}|0\rangle + e^{i\phi}\sin\frac{\theta}{2}|1\rangle, \tag{1.3}$$

where numbers θ and ϕ define a point on three-dimensional sphere, called the "Bloch sphere", shown in Fig. 1.2.

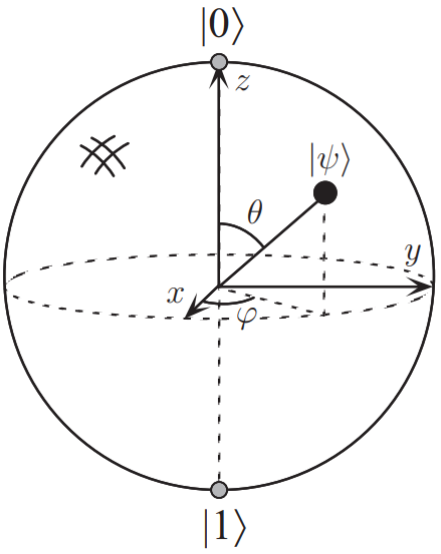

Figure 1.2: Represenation of a qubit on a Bloch sphere. The picture is taken from [1]

.

This is just a intuitive representation of a single qubit that by no means has a simple generalization when multiple qubits are performing the computation.

Physical systems and DiVincenso's criteria

So far there have been several physical systems proposed to encode information as a quantum superposition of two physical bits of information and therefore be a strong candidate for the first quantum computer. But first, according to David DiVincenzo such technology needs to satisfy several strict criteria [10]:

1. Initialization

We start with an obvious criterion that refers to qubit preparation in an initial input state that will be evolved during an computation. Depending on the specific technology it usually means the ability to cool down a quantum system to a low entropy state or generate single photons in specific spatial mode etc.

2. Measurement

In this case DiVincenzo refers to an ability to determine the output state fast with high fidelity.

3. Scalability

Understanding this criterion can be quite tricky. In the first place, the resources of the UQC have to scale linearly while the complexity space increases exponentially. This means that ultimately the computational power arises from the fact that quantum mechanics allows information to be entangled, therefore the dimensions of the Hilbert space available on an quantum system of N entangled qubits increases exponentially meanwhile the complexity of an unentangled counterpart of classical information scales polynomially. On the other hand, from an engineering perspective, it is not just the computational scalability that needs to be satisfied but also the scalability of the physical qubits where the information is encoded. Such as a space on a microchip, classical microwave electronics, coherence time of a laser etc.

4. Universal logic

There are several models to perform logical operations on a quantum computer. One of them is the Gate model, which is sufficient to perform universal quantum computation only with an arbitrary single qubit rotation and almost any two qubit entangling operation such as a controlled-NOT gate. Another example is the Measurement-based (One way) quantum computation where a fully entangled cluster state of all possibilities is prepared and by changing the measurement basis, different logical operations are realized and a specific computational path on the cluster state is performed.

5. Decoherence time of a qubit is much longer the computation time

Each physical representation of qubits for different technologies have a different decoherence times of that qubit being in a quantum superposition. It is called the T_2 coherence time. Decoherence takes place continuously due to unwanted environmental effects destroying the coherent information carried within the computational time. Therefore, it is in our most interest to have coherence time T_2 much longer than the time of the computation.

Scalable Quantum Technologies

Cold ions on chip

One of the first physical systems that was proposed to encode quatum information was based on cold ions [11], [12]. Even though the fidelity of single and two qubit operations are highly above the error correcting threshold for fault tolerant quantum computation [13], [14], until now ion trap QC did not have a proposal for a scalable architecture due to the enormous difficulty to initialize, manipulate and protect individual single ions. Recently, there was introduced a blueprint [2] based on microwave ion trap QC [15]. The basic difference between optically addressed ions is the idea of initialization, control and protection of "Dressed" ions using static magnetic field gradients with external microwave source. The architecture shown in Fig. 1.3, can hold more than 2.2 million physical qubits on a 20.3 m^2 modulus that can be connected to different moduli provides an undeniable scaling possibilities. Unfortunately, because of its (still) quite big size, there are several difficult engineering challenges regarding the vacuum system, nitrogen cooling system and the alignment of the global laser beam that is used for detection of the quantum state.

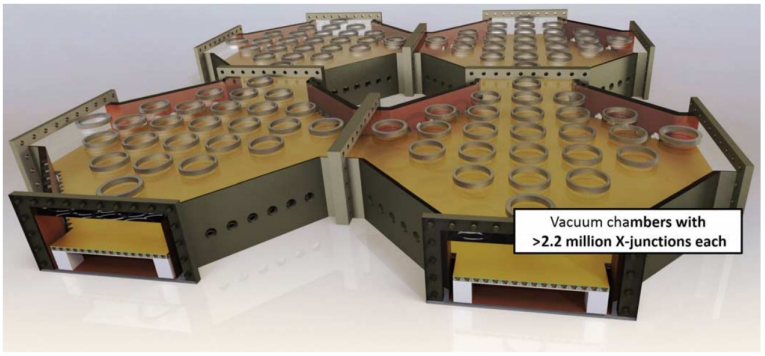

Figure 1.3: Schematic illustration of several connected moduli of vacuum chambers to form a scalable platform for microwave ion trap quantum computing. Picture taken from [2]

.

Superconducting circuits

Another promising technology to provide a fully scalable architecture is based on superconducting qubits. Recently, a blueprint to demonstrate quantum supremacy, an idea to implement an algorithm (such as Boson sampling [16]) that can not be efficiently solved on a classical computer, has been proposed with superconducting circuits [3]. Such a platform demonstrates relatively high Ramsey dephasing time of $5\mu s$ providing hundreds of operations within the time of the computation. High fidelity operations [15], [17], [18] with low error rate and robust nanofabrication techniques makes superconducting qubits very attractive architecture to achieve the desired quantum supremacy with $50 - 100$ physical qubits. Unfortunately, it is not enough to build a fault tolerant UQC. In order

to scale it up, the architecture requires thousands of physical qubits to construct a single logical qubit with low error rate to implement one of the most resilient error correcting codes, the Surface code [19]. This would mean that the small space in a cryostat (or wafer) would at some point limit the architecture to few thousands of logical qubits (if not less). Even though there are recent impressive experimental improvements in state transfer between different moduli, the fidelity of the operation is so far only 80 % [20].

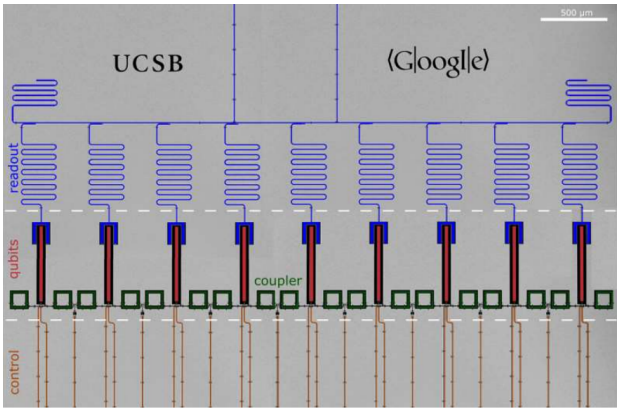

Figure 1.4: Optical image of several coupled superconductive "gmon" qubits integrated on a silicon chip. Picture taken from [3].

Semiconductor quantum dots and P doped silicon

The last technology we mention is based on semiconductor quantum dots [21] (Fig. 1.5) and phosphorus doped silicon [22]. In the first case the information is encoded in the spin of a quantum dots, which are produced from a 2D fermionic cloud, by cleverly applied electric fields. Two such excitons can interact through an overlap of their wavefunctions achieving relatively high fidelity of two qubit operation. In the second case, phosporus ions are implanted within 5nm precision and can be controlled with high precision via electric and magnetic fields. Even though the qubits are encoded in different physical systems the overall engineering architecture is quite similar. So far the biggest problem with this architectures is the fidelity of two qubit gates not being able to exceed 85% [23], [24].

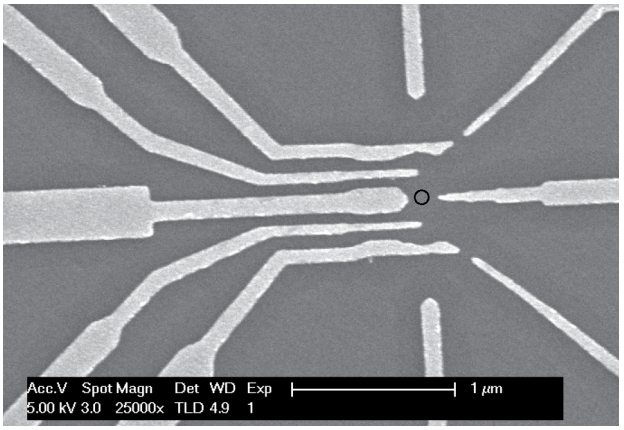

Figure 1.5: SEM image of a gate for manipulation of a semiconductor QD shown with black circle. Picture taken from [4].

1.0.3 Quantum communication

So far we discussed different ways of encoding information into stationary qubits like ions or semiconductor quantum dots. The disadvantage of such platforms is clearly the impossibility to distribute entanglement for long distances. For that purpose we can use single photons. Quantum information can be encoded into different degrees of freedom such as polarization, space, time or frequency of a single photon. In the next section we will further discuss the possibility to use light as information carrier for UQC. But for now single photons can be used as flying qubits across few hundreds of kilometres of low loss optical fibre network [25] (Fig. 1.6) to distribute quantum entanglement.

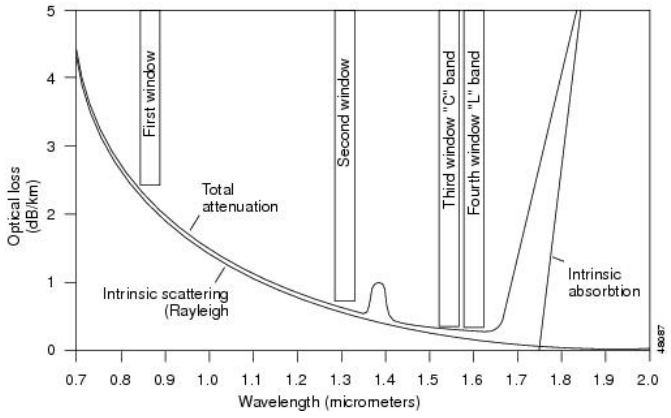

Figure 1.6: Optical fibers with low loss as 0.2 dB/km at the telecomunication C band provide a perfect tool to distribute entanglement over long distances for secure communication. [5].

Entanglement is a very strong feature of quantum mechanics that does not have a classical counterpart. One of the first applications of photons distributing entanglement was a proposal for secure communication through any of the quantum key distribution (QKD) protocols. In the heart of such protocols is the fact that any eavesdropping activity would affect the distributed quantum system which would give notice of its intruding presence.

1.1 Integrated quantum photonics

Another platform that potentially meets all DiVincenzo's criteria is based on integrated quantum photonics [26]. As it was mentioned before, nonclassical states of light can be used to encode information that harness a great potential to implement secure communication. Their long coherence time and easy manipulation makes them highly attractive physical system. On the other hand, two photon interaction requires strong optical nonlinearities to obtain a π phase shift. To overcome this obstacle, a breakthrough paper by Knill, Lafflame and Milburn [27] showed that single photon sources, detectors and linear optics are enought to perform single and two qubit operations, necessary for UQC. As a consequence, there has been an enormous effort to integrate all these crutial components on a small chip to build a UQC [28].

1.1.1 Sources

Nonclassical states of light are crucial for quantum technologies. Together with the development of low loss optical structures, the integration of highly indistinguishable, deterministic single photon sources is the most challenging task to achieve in a photonic architecture. Photonic sources can be categorized into two classes: spontaneous and deterministic. First, are based on nonlinear effects of the material such as Spontaneous Parametric Down Conversion [29] (SPDC) and Spontaneous Four Wave Mixing [30] , [31], [32], [33] (SFWM). Correlated pairs are produced as a frequency conversion of two pump photons into signal and idler photon that conserve the energy and momentum of the process. The benefit of such source is that it can be found in pratically any material since these can be cathegorized as crystalline, polycrystalline or amorphous which exhibits either χ_2 or χ_3 nonlinear process. The big disadvatage is that such source is probabilistic. One way to make it near-deterministic is to perform either spatial [34], or time-domain multiplexing [35]. That would require integrate several sources, herald single photons from each generated pair, delay them in a quantum memory (this essentially means that each photon would have to propagate in a long waveguide with fast low loss optical switch and electronics) and then time synchronize them all together. Such an architecture is quite complex and takes up a lot of space. So far there has been few demonstration of multiplexing but none one of them was fully integrated.

The second type of nonclassical source are atom-like emitters such as self-assembled quantum dots and solid state point defects. Quantum dots (QD) have shown remarkable performances with high purity, brightness and indistinguishably [36], [37], [38], [39]. QD emmit in all directions, therefore having sources integrated on a single photonic platform where the emmited photons are coupled to a waveguides is reachable but a challenging task [40]. Furthermore, the stochastic nature of their growth results in random spatial and spectral properties, making two sources less indistinguishable and at the same less compatible with standard nanofabrication processes. On the contrary to QD, point defects can be created with great precision [41] using ion implantation method [42]. The most studied defects are based on nitrogen-vacancy [43], [44] (NV) and silicon-vacancy [45] [46] (SiV) in diamond, that emit at the visible wavelengths. High quality diamond is grown homoepitaxially in sizes between 2-5 mm which strongly limits its scalability. Furthermore in order to achieve high indistinguishability with either QDs or point defects, they must be operated under cryogenic temperatures which further limits the scalability of the architecture.
Additionally, information can be encoded into squeezed states of light to form a qubit for continuous variable UQC (CVUQC) [47]. The quantum states can be prepared deterministically by either χ_2 [48] or χ_3 [49] nonlinear process. The downside of CV is its infinite-dimensional (analog) encoding in Hilbert space that requires high levels of squeezing and hybridization with discrete variables for fault tolerant UQC [50].

1.1.2 Linear circuits

In 2001 Knill, Lafflame and Milburn [27] showed that a non-deterministic UQC can be performed with linear optics. In the heart of the scheme is the experimental realization realization of a two qubit control-NOT (CNOT) gate [51], [52] where a nonlinear phase shift with a probability of 1/16, between two qubits encoded in two photons, is realized via conditional postselection from a single photon measurement. The CNOT operation works in the following way: Two qubits, the control and target qubits, serve as a logical input of the gate. Depending on the state of the control qubit, the target qubit either does or does not flip its logical bases. If the control qubit is in the state $|0\rangle$ the target qubit does not change its logical value. Otherwise, if the control qubit is $|1\rangle$ the target flips its basis.
Photonics has a great ability to fabricate linear circuitry on a micro chip which makes this platform very attractive. First demonstration of Hong Ou Mandel interference effect, realization of a CNOT gate [26] and first integrated version of Shor's factoring algorithm [53] opened a new era of quantum optics experiments performed in a silica on silicon photonic chips. The initial motivation behind the KLM scheme was an understandable concern about achieving strong nonlinear interaction between single photons to demonstrated deterministic CNOT operation. Alternatively, integrated photonics provide an efficient way to fabricate resonators with small modal volume and high quality factor

[54], [55] to achieve strong coupling conditions with individual atoms to perform logical operations on a single photon level [56], [57].
Apart of logical circuits, additional classical components also need to be integrated on the chip [58]. In order to avoid blinding the single photon detectors, the pump needs to be filtered out by more than 100 dB. This can be quite a challenging task, particularly in case when the sources are based on SFWM, as the pump is spectraly very close with the generated single photons. Furthermore, any residual scattering in the chip limits the signal to noise ratio as more accidental photons can be detected. Reconfigurability of optical circuits is also highly desirable. Depending on the material, phase shifters can be implemented by either thermal [59], mechanical [60], Pockels effect [61] or even Kerr effect [62]. For most proof of principle demonstrations thermal phase shifters have been used. These are very slow for any scalable application, therefore proposals of hybrid platforms [63], [64] with different materials will possibly solve this problem.

1.1.3 Detectors

In order to measure the output state in many quantum optics experiments, researchers use either superconductive single photon detectors (SSPD) or silicon single photon avalanche photodiodes (SPAD). SSPD's have proven to be very usefull in many protocols operating at telecom wavelenght. Their detection efficiency exceeds 90% [65] with a ultra low dark count and dead time, which makes them highly desirable. Unfortunately, there are several drawbacks to this technology. First, the necessity to operate at cryogenic temperatures makes scaling up photonics a challenging task. Apart of that, their performance is highly sensitive to fabrication tolerances as the detector is composed of a 5 nm thick and 80 nm wide nanowire. On the other hand, SPAD's have been proven to have all the desired qualities of an efficient detector. In contrast to SSPD's, they are used in experiments regarding visible wavelengts. Commercial devices are cheap, have a quantum efficiency of more than 70%, with low dark counts and jitter [66]. Most importantly they work at room temperature and they are very robust against fabrication tolerances making this technology highly uniform on a full wafer scale. In order to avoid additional losses from outcoupling light into an optical fiber, it would be desirable to integrate single photon detectors on the photonic chip. This feature has been already demonstrated for SSPD's [67] but not for SPAD's.

1.1.4 Materials

There are many materials that have been proposed as a potential platform for integrated quantum photonic technologies [68]. But as it is hard to fulfil all the strict requirements to be a fully on chip based technology, hybridization of several materials might be taken into consideration. Here, we review some of the most common materials.

Silicon is a material with a mature fabrication due to existing microelectronic industry. Therefore, it has been just a matter of time when first silicon based quantum photonic microelectronic chip would occur, taking advantage of the commercial 45 nm complementary metal-oxide semiconductor (CMOS) technology [69]. Silicon (Si) has high refractive index of 3.6 that provides the possibility to confine and guide light in sub micrometer waveguide structures. The material exhibits high χ_3 nonlinearity which has been used to produced correlated pairs of photons at telecom wavelength via SFWM process in either straight waveguides [70], [71] or microring resonators [72], [73]. However due to small energy bandgap of 1.12 eV, silicon is plagued by two photon absorption which limits the generation rate of nonclassical states of light. Applying a reverse voltage in a p-i-n junction can slighty mittigate the effect of free carriers [74] but still does not fully remove the saturation effect of the two photon absorption. So far, most phase modulations have been achieved with thermorefractive effect which are slow for large scale quantum information processing (QIP). Silicon is a centrosymmetric material which is lacking the Pockel's effect for fast modulation. Additionally, nonlinear absorption prevents the use of Kerr effect for switching due to increase losses. Solution might be found in hybrid integration with a χ_2 material but due to high confinement of Si the overlap for efficient application is still questionable.

Lithium Niobate (LiNb) has been considered for a very long time as a limited technology for scaling quantum nanophotonics due to its challenging waveguide fabrication. In conventional method waveguides were fabricated with proton ion beam lithography. This process produces optical channels with low confinment that would result to bending limitation of few milimeters. But recent results show fabrication of ridge waveguides with losses as low as 3 dB/m [75] measured with a ring resonator cavity (80 μm radius). Later, fast, low loss Pockels modulation of 230 GHz has been achieved with a 5 mm long device driven with CMOS compatible voltages [71]. These results made LiNb to be reconsidered as one of the most promising platforms for both quantum [76], [77] and classical integrated photonic technologies.

Silicon Nitride is another CMOS material with highly matured nanofabrication procedures [78]. The energy band of 4 eV promises low loss integrated photonics ranging from visible to mid infrared spectrum. Unlike Si, Silicon Nitride (SiN) does not suffer from two photon absorption enabling both ,integration of efficient sources of time bin entangled photons and fast modulation via Kerr effect (cross-phase modulation) [62]. SiN is a amorphous that is well known for its wideband Raman spectrum that can potentially limit the performance of the single photon source due to unwanted generation of spurious Raman photons [79]. Solution to this problem is undergoing the experiments in cryogenic or liquid nitrogen temperatures in order to decrease the population phonons in the material. This is not necessarily inconvenient since these chips might already be at cryogenic temperatures to allow SSPDs, integrated into the same chip, to function.

Together with advanced photonic circuits, SiN is considered to be interesting candidate for QIP.

1.2 Quantum Simulation

Before building a full scale universal quantum hardware, applications of simple quantum algorithms will be first to come due to their more lenient requirements on the resources [80]. One example concerns the temporal evolution of a quantum system where the Hilbert space is described by a number of parameters which rise exponentialy in size with the number of resources, therefore simulating the amplitudes of all classical configurations is considered to be a hard task even for modern supercomputers. In 1982 Richard Feynman proposed an idea where an intracable dynamics of one quantum system can be solved using dynamics of another quantum system - analog quantum simulator [81].

1.2.1 Analogue quantum simulator

To emulate/mimic the evolution of a quantum state $|\phi(0)\rangle \xrightarrow{U} |\phi(t)\rangle$ one can use a Hamiltonian of an accessible physical system P that exhibits correlation between the quantum state of the physical system $|\psi(0)\rangle$ and the emulated state $|\phi(0)\rangle$ in such a way that [82]

$$|\phi(0)\rangle = f|\psi(0)\rangle, \tag{1.4}$$

where f is an invertible map that determines the correspondence between all the operators and states of the physical system P and emulated system E (Fig. 1.7).

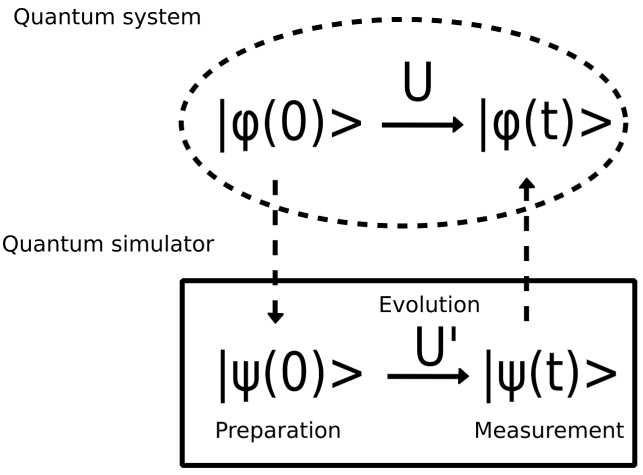

Figure 1.7: Quantum simulation of an unreachable quantum system $|\phi(t)\rangle$ that is emulated by initializing an input state $|\psi(0)\rangle$ that we evolve via unitary evolution U' to obtain a measurement output of the evolved state $|\psi(t)\rangle$ from which we can reconstruct the unknown unitary.

The universal quantum computation theorem [83] guarantees that any operator can be composed of natural evolutions in P and external interaction defined by sufficient class of logical gates implemented in the system. In this way, the Hamiltonian of the physical system H_P and Hamiltonian of the emulated system H are also correlated

$$H = f^{-1} H_P f \tag{1.5}$$

and the Unitary evolution U of the emulated system S can be identified as Unitary evolution U' of the physical system P

$$U = U', \tag{1.6}$$

$$e^{-i\hbar H t} = e^{-i\hbar f H_P f^{-1} t}. \tag{1.7}$$

1.2.2 Quantum walk

One example of analogue quantum emulator is based on a quantum walk algorithm. One way to describe a quantum walk is by its continuous model [84]. The idea is based on the continuous time classical Markov chains. Imagine a graph that consists of a vertex set V such as in Fig. 1.8.

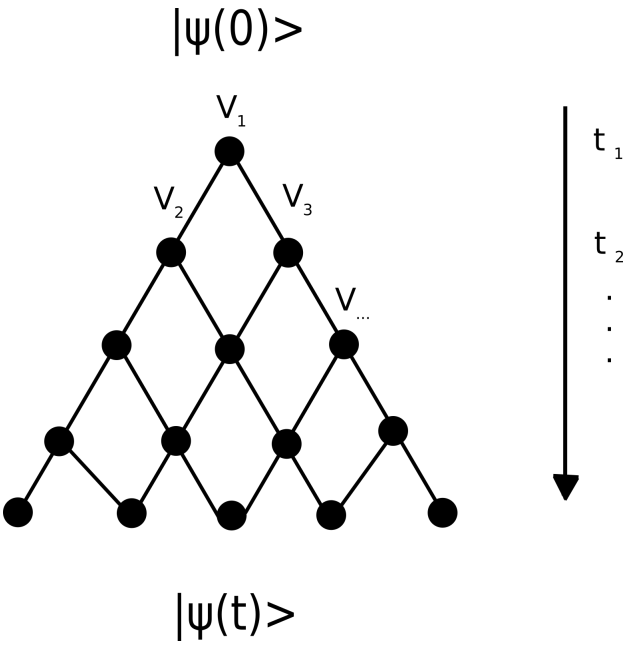

Figure 1.8: Schematic representation of quantum walk on a set of vertices where an initial input state $|\psi(0)\rangle$ evolves over discrete time to an output state $|\psi(t)\rangle$ whose simulation we are interested in.

A step in classical random walk can be described by a matrix M that describes the transformation of the propability distribution over the vertices from set V. The elements of the matrix $M_{i,j}$ give the propability of a one step from vertex i in time t to vertex j at time $t+1$. Essentially the propability distribution p_i^{t+1} given in time $t+1$ is

$$p_i^{t+1} = \sum_j M_{i,j} p_j^t \tag{1.8}$$

$$\vec{p}_{t+1} = M\vec{p}_t. \tag{1.9}$$

This is a discrete-time quantum walk model. In order to be continuous we have to assume that transitions occur at all times and the jumping rate from a vertex i to its neighbour j is given by a fixed, time-independent constant γ. The infinitesimal generator matrix H and its elements $H_{i,j}$ of such a process is given by:
$H_{i,j} = -\gamma$ if $i \neq j$ and they are connected.
$H_{i,j} = 0$ if $i \neq j$ and they are not connected.
$H_{i,j} = d_i\gamma$ if $i = j$ and they are connected,
where d_i is the degree of i.
Given the generator matrix H the Eq. 1.8 can be rewritten as

$$\frac{dp_i(t)}{dt} = -\sum_j H_{i,j} p_j(t) \tag{1.10}$$

with a solution given as $\vec{p}(t) = \exp(-Ht)\vec{p}(0)$.
The extension to continuous quantum random walk is given by the idea of Farhi and Gutmann [85] to interchange the generator matrix for a Hamiltonian H of the process that describes the evolution $U(t)$ as

$$U(t) = \exp(-iHt) \tag{1.11}$$

Measuring the positions of an evolved quantum state after time t will results in a reconstruction of the unitary evolution $U(t)$ which depends on the initial state as opposed to Markov chain which is state independent. The absolute advantage of quantum random walk over its classical counterpart [86] is given by the ability to quadratically decrease the expected hitting time of a walker on a specific position given by the vertex in the position space. Using the time evolution of a quantum walk described by Eq. 1.11 one can emulate a time evolution of another physical system (Eq. 1.7) just by implementing a Hamiltonian of the quantum walk that corresponds to the simulated system.

1.2.3 Quantum simulation on a photonic chip

Quantum walks have been demonstrated using different technologies ranging from trapped ions [87] , superconducting circuits [88], nuclear spin resonances [89] up to atomic gases [90] and optical lattices [91] to provide a successful realization of a quantum simulator. Although, the experimental demonstrations are very impressive most of the technologies nowadays are expensive due to their operation at low temperatures and high vacuum, which restrict their possible commercialization. On the other hand, integrated photonics offers the possibility to integrate small scale quantum simulator that can work at room temperature.
Quantum walk can be realized on a photonic chip using photons that are propagating in a coupled waveguided arrays. It has been shown that one photon quantum walk is not sufficient enough to provide a non-classical advantage since such dynamincs can be perfectly explained as a classical wave phenomenon [92]. Thus, to first observe the quantum speedup and harness the power of entanglement, atleast two particles need to be present in the walk [93]. The first realization of a quantum walk of correlated photons has been done by Perruzzo [94] with an exclusive experimental proof on nonclassicality of bosonic statistics. Afterwards, a boom of experiments of nonclassical walks in integrated structures arrised. So far, there has been a demonstration of analog quantum simulation of fermionic and bosonic statistics using anyons [95], [96], simulating enviroment assisted quantum transport in biological complexes with controlable decoherence [97] and transport efficiency in a quantum maze [98], Anderson localization [99] and 3D walks [100]. But so far, none of these experiments provided integrated sources and detectors to realize a fully integrated quantum simulator.
As it was mentioned before, the wide bandgap of SiN offers the possibility to fabricate

low loss waveguides at visible wavelengths with a back in the end CMOS compatible process which offers to fully integrate efficient SPAD detectors, fast electronics and optical channels operating at room temperature making SiN very attractive for near future applications in quantum technology.

1.3 Outline of the thesis

In the first chapter we discussed why it is important to build a new type of computer based on quantum mechanical principles. We mentioned several conditions what such a platform requires to be truly universal and scalable. We especially focused on the photonic architecture that can be also useful for large distance quantum communication. The scope of this thesis is to develop possible sources and detectors of nonclassical states of light in a SiN photonic chip that can be used for quantum computation, communication or metrology.
The thesis is organized in a following way:
In Chapter 2 we introduce the basics theory of Snells law in optics, light propagation in optical waveguides in ray picture that is later expanded into electromagnetic theory. Then we describe the simulation software that is used to design crucial parts of photonic components such as couplers, waveguides and ring resonators. Afterwards, in Chapter 3 we develop fabrication techniques like material deposition and etching requirements to prepare the photonic chip. The first experiments regarding linear characterisation of optical waveguides is performed in Chapter 4, where we measure losses via the cut-back method and using the transmission line of the ring resonator. We discuss several conditions to obtain the best, low loss ring resonators to enhance the generation of non-classical resource. Chapter 5 then describes the four wave mixing process that lies in the heart of all following experiments regarding the generation of twin beams and squeezed states of light. In the same chapter, we describe the experiment to measure the generation rate in the near visible spectrum. Afterwards, we discuss integration of single photon detectors and describe an architecture to provide a fully integrated platform for small scale quantum simulator working at room temperature. Since single photons are very hard to scale up due to their probabilistic nature, in Chapter 6 we move towards on chip generation of continuous variable qubits where we discuss its advantages and disadvantages for QIP. Finally, we measure squeezed states of light and we expand the discussion for potential future work.

Chapter 2

Fabrication Of Si_3N_4 Photonic Chip

In this chapter, we describe the fabrication process to produce a SiN photonic structures developed in the Southampton Nanofabrication center. For this reason a study and realization of a Plasma-Enhanced Chemical Vapor Deposition (PECVD) process of SiN was performed. Generally, SiN is a well known material to fabricate nanoelectronics and photonic components, therefore the process itself is not as complicated as in the case of other materials such as Silicon Carbide or Lithium Niobate.

2.1 PECVD deposition for low loss SiN material in the visible

The aim of this thesis is to develope low loss SiN photonic structures in the visible spectrum. Low loss optical waveguides has already been fabricated using the low-pressure chemical vapour depositon technique (LPCVD) [101]. However good the optical properties of LPCVD waveguides are, one can not truly fabricate them in a fully CMOS compatible manner. This is because the high temperatures of more than 700°C can damage the CMOS electronics. On the other hand, PECVD depositon requires temperatures of 350°C and lower to obtain high quality thin films [102]. This makes PECVD deposition CMOS friendly and therefore highly attractive for commercial purposes.
The chemistry that is involved in the Si_xN_y deposition is generaly based on mixing the folowing gasses: SiH_4,NH_3 and N_2. Proper combination of individual ratios of the gas flows determines many important material properties such as index of refraction, absorbtion spectrum, stress and deposition rate. Another important parameter to consider is the excitation frequency of the PECVD machine: High frequency (HF-PECVD) at 13.56 MHz and low frequency (LF-PECVD) at 50 kHz. The main difference between these

two regimes is that in the LF-PECVD condition the low mass hydrogen ions follow the applied radio frequency and therefore the kinetic energy during the bombardment of the substrate material is less destructive which results in a smoother bottom roughness. Not trying to reinvent the wheel we follow the steps published in [103] which resulted in a SiN material well suited for our purposes.

2.2 Lithography

Lithography is the process of transferring a designed pattern to the device layer. There are two distinct types of lithography processes: electron beam lithography (e-beam) and optical lithography. Generally, in optical lithography a photomask made out of quartz reticle with a chrome pattern is needed. The mask is made in such a way that it has alternating transparent and blocked regions for exposure. The feature size is limited by the diffraction limit of the wavelength used therefore the resolution is not better than 300 nm. The advantage of using optical lithography is the fast speed and small cost associated with transferring a pattern from a mask to a wafer. The downside is the use of different mask for different pattern design. On the other hand e-beam lithography does not require a mask. The e-beam resist is exposed by the means of collimated beam of electrons to write the pattern directly which allows a great amount of flexibility with the patterned design. Resolution of the e-beam lithography is limited by the wavelength of the accelerated electrons, and even though the minimum feature size depends on the resists itself it is possible to achieve resolution down to 10 nm. However, the writing times for e-beam can vary a lot depending on the patterning area, dose and current used. This can lead to very high production costs and potential drift in tool performance during the course of a single write. We used the e-beam because of the feature size and resolution advantages over optical lithography.
To design the pattern for the e-beam lithography we used a "Computer Aided Design" (CAD) software to draw waveguides as rectangles or rings as circles which are composed of many individual polygons. We used an University available commercial software L-Edit. We then exported the layout in the Graphic Data System II (GDSII) format. The GDSII file has been later used as a input for the BEAMER software to generate the v30 file which contains the information about the dose distribution for the pattern which has been corrected by possible back and second order electron scattering processes (proximity error correction - PEC). We used the JEOL-9300 tool which is a 100 keV e-beam writer. The current can be adjusted from 100 pA to 10 nA. Larger currents led to larger spot size for the tool and worse resolution. We set the current for our fabrication to 10 nA with an e-beam aperture of 200 μm which results of a spot size of 20-24 nm. Generally, the rule of thumb is that higher spot size and shorter shot steps results to an overlapped beam spots which decreases the waveguide roughness. The field of view of the e-beam tool determined the writing window. At the boundaries of the writing window

the least sensitive features were placed to avoid stitching errors when the e-beam is moving to the next field of view causing a misalignment of the pattern at these points. The JEOL-9300 had a field of view 1x1 mm^2. In our fabrication process we used a positive e-beam resist CSAR62. It is a cheaper alternative to another e-beam resist ZEP, that can reach analogous results in terms of resolution, development and etching stability. Depending on the etching thickness of the SiN we used different spinning speed to obtain different thickness of the resist. The spinning curve of CSAR62 is shown in Fig. 2.1.

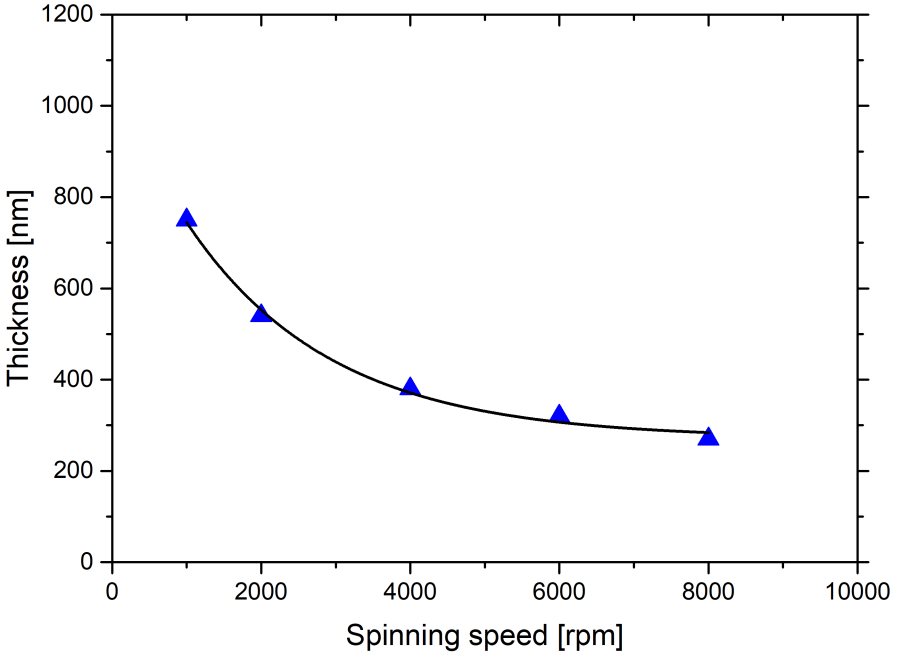

Figure 2.1: Spinning curve of positive resist CSAR62

Most of the times we spun the resist at 5000 rotations per minute (rpm) for 60 seconds to obtain a thickness around 400 nm. We then baked it at a hotplate at 150 °C for 3 minutes and spun e-spacer on the sample at 3500 rpm for 90 seconds to mitigate charging at the field boundaries. We used a variety of doses between 150-300 μC for the exposure to estimate the lowest sidewall roughness from the lithography process. After the dose test we used a dose of 260 μC

2.3 SiN etch

Photonic structures are generally patterned by the means of either optical or e-beam lithography systems with a requirement for highly anisotropic etch. As mentioned above,

SiN is well characterised material, therefore obtaining an anisotropic profile with little or almost none sidewall roughness is not highly time consuming. The standard etching tool for SiN is the ICP RIE (*Inductively Coupled Plasma Reactive Ion Etching*). In the chamber the reactive ions impact the surface with high energy which results in a combined chemical and physical etch process. Strong RF sources generate the reactive plasma from gas precursors meanwhile additional RF induction magnetic coils control the plasma density, providing supplementary advantages in term of process control over standard RIE tools. The ICP RIE technology offers great versatility in the choice of the parameters and its potentials in the nanofabrication of SiN has been widely investigated. The optimal condition of the etch is strongly dependent on the exact properties of the plasma and chamber configuration. In order to not reinvent the wheel we developed our process starting from several available recipes either in the SNC RIE/IPC RIE machines or from the University of California, Santa Barbara (UCSB) online library. The principal etch gases for SiN are the fluorine containing gasses such as CHF_3, CF_4 and SF_6. Usually, the gases can be combined with levels of O_2, CO_2 or H_2 to adjust the process etch rates or selectivity. First recipe we tried was in the RIE machine which reguired a gas mixture of 50 sccm of CHF_3 and 5 sccm of O_2. The RF power was set to be 150 W while the pressure was set at 55 mT.

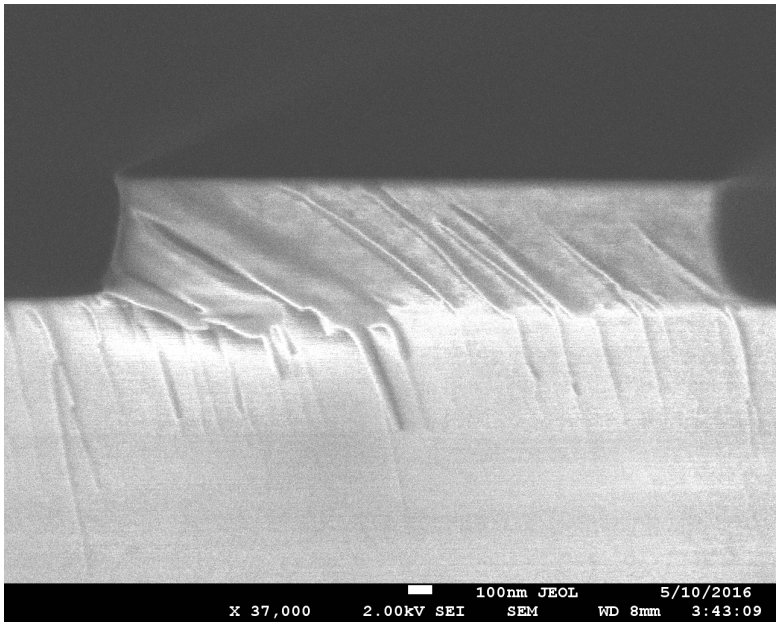

Figure 2.2: SEM image of a highly isotropic RIE etch for SiN waveguides.

We can see from Fig. 2.2 that the etch is highly isotropic which is propably a result of low RF power and high chamber pressure. Such a waveguide profile is highly undesirable therefore we started to use the IPC RIE machine instead. The next recipe we used was a one that was avalible from the UCSB online library [104]. This recipe was quite standard having again a combination of 40 sccm CHF_3 and 10 sccm of O_2 with a RF

power of 50 W ,ICP power of 1000 W and a chamber pressure of 5 mT. The profile is shown at Fig. 2.3.

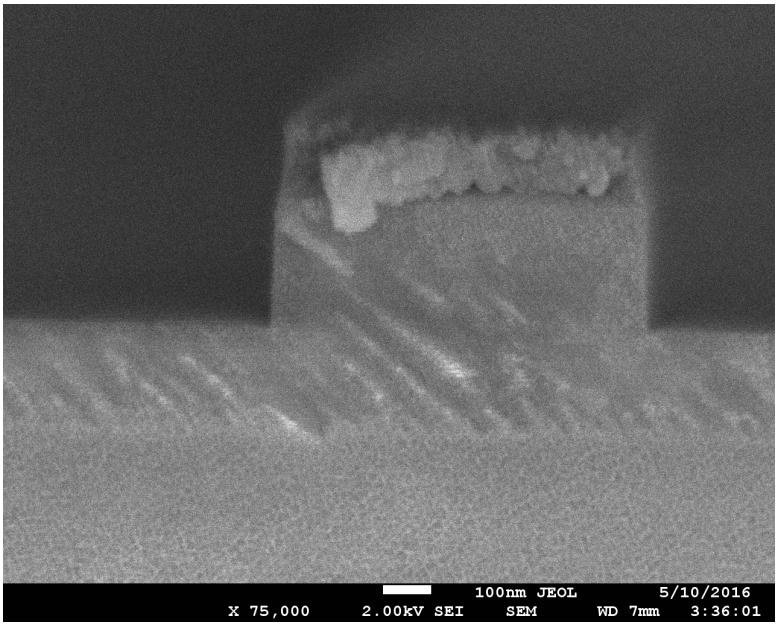

Figure 2.3: SEM image of a highly anisotropic etch from UCSB library.

Even though the verticality of the profile is practically 90° we found out that the selectivity, which is a ratio between the etching rate of the CSAR62 and the etching rate of SiN, is below 1. This limits the possible thickness of 300 nm that we can etch without leaving a burned residues on top of the SiN waveguide. Therefore, the last recipe we tried was one that was already available in the ICP RIE machine. This recipe was quite unconventional. It had a gas mixture of 22 sccm of SF_6 and 44 sccm of C_4F_8 which means that during the etch process two fluorine based gasses are mixed without an additional gas to adjust the selectivity. The RF power was 21 W, the ICP power was 1000 W and the pressure was 5 mT. As it turned out this recipe was most suitable for our applications. The selectivity was above 1 and the etched profile was highly anisotropic, see Fig. 2.4 and Fig. 2.5.

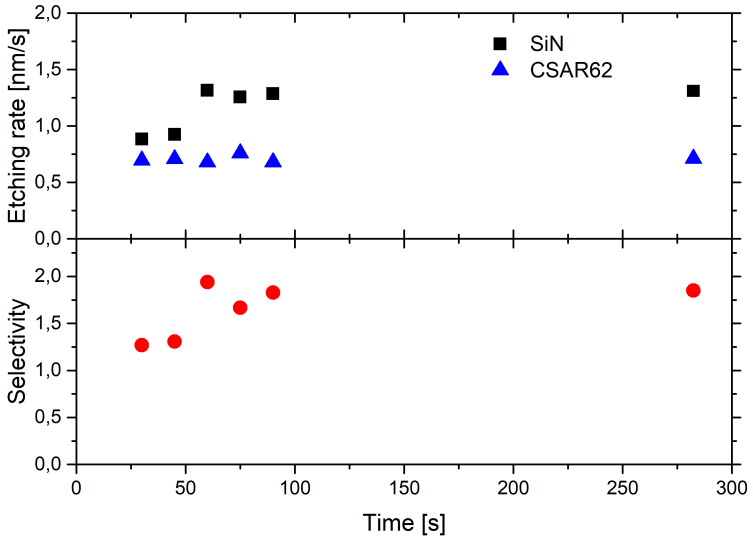

Figure 2.4: Selectivity of SiN/CSAR. Top picture shows the etching rates of SiN and CSAR while the bottom showns the selectivity for different times.

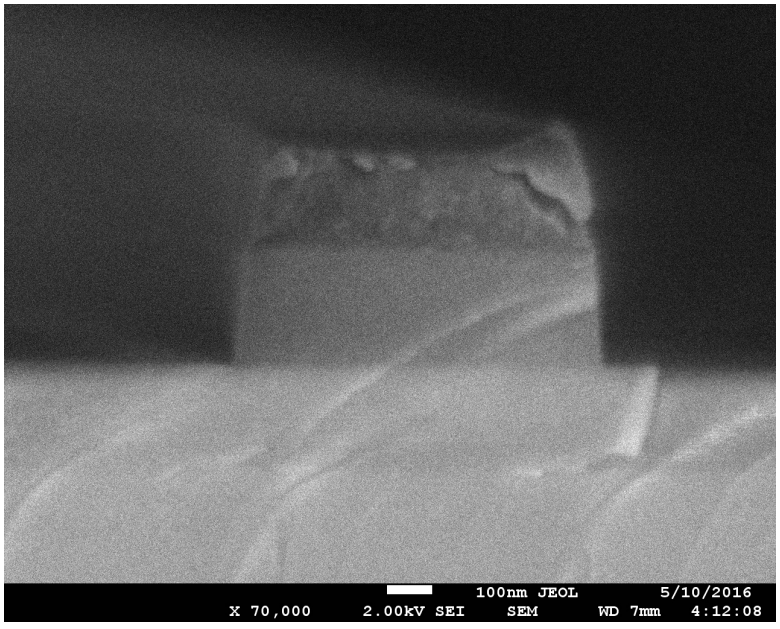

Figure 2.5: SEM image of an anisotropic etch available from the ICP RIE in the University of Southampton nanofabrication facility.

2.4 Top cladding

After etching we had to remove the leftover resist. For that purposes we used the O_2 plasma from the RIE machine. To further ensure no particles are left we clean the

sample in the NMP/Aceton/IPA sonification process. Afterwards, we were left with exposed SiN waveguide. In order to form buried, symmetric channel waveguides we had to clad the SiN with a material which refractive index is as close as possible as the one from the bottom thermally grown SiO_2. For this purpose we had available three different materials. First was Poly(methyl methacrylate) (PMMA) which we used to characterise the roughness losses of the specific etches and dose tests presented in Sec.4. This polymer can be easily spun as a top cladding without creating additional roughness. Its refractive index of 1.48 is close to the one of SiO_2 and low material absorption makes it perfect for the purpose to use it as a reference cladding. The second used material was PECVD SiO_2. It has a refractive index of 1.45, much closer to the thermal oxide, to form symmetric channel waveguide. Unfortunately, it turned out that this cladding tends to create air voids during deposition which affected the coupling efficiency of our gratings. Also, its material absorption was much higher than expected. For that reason we mainly used Tetraethyl orthosilicate (TEOS) SiO_2 which has a great conformality and does not create voids but more importantly, its dielectric properties are comparable to those of thermal SiO_2. In Sec.4 we present all the optical characterisation to decide which fabrication process is most suitable for specific application presented in the thesis.

Chapter 3

Theory And Simulation Of Light Propagation In Optical Waveguides

In this chapter, we introduce the basics of light propagation in optical waveguide structures. In the first section, we derive the Snell's law and we explain the conditions for total internal reflection in a one dimensional waveguide interpretation. In the second section, we expand the 1D ray theory to 2D case of channel waveguide, where we need to introduce Maxwell's equations for light propagation in dielectric media. We continue to show simulations of photonic components such as multi mode (MM) waveguides, tapers and grating couplers in the Lumerical Solution. Furthermore, we describe the theory of ring resonators and explain how varying the gap between the bus and the fabricate ring resonators can be used to estimate the coupling condition and hence retrieve the optical loss of the waveguide structure.

3.1 Snell's law and total internal reflection

Imagine a situation where a monochromatic plane wave is incident on two distinct optical media with a refractive index of n_1 and n_2, see Fig. 3.1

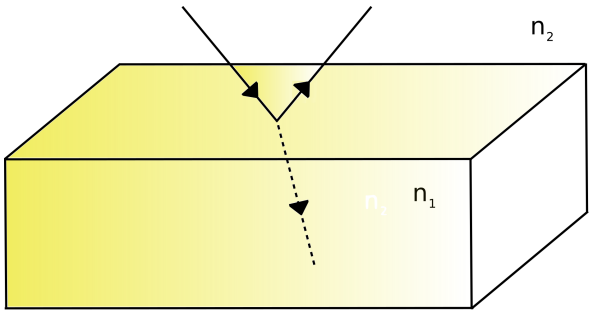

Figure 3.1: Illustrative image of light incident on two distinct dielectric media where part of the beam gets reflected and part is getting transmitted at the interface.

The incident wave coming from the optical medium 1 has a frequency ω, position vector $\vec{r}$, wave vector $\vec{k}$ and can be described

$$\vec{E} = \vec{E_0} e^{\left[-i\left(\omega t - \vec{k}\cdot\vec{r}\right)\right]} \tag{3.1}$$

After the incident wave interacts with the second optical medium it can be decomposed as a reflected R and transmitted T wave which we described as

$$\vec{E_R} = \vec{E}_{0R} e^{\left[-i\left(\omega_R t - \vec{k_R}\cdot\vec{r}\right)\right]} \tag{3.2}$$

$$\vec{E_T} = \vec{E}_{0T} e^{\left[-i\left(\omega_T t - \vec{k_T}\cdot\vec{r}\right)\right]} \tag{3.3}$$

At the moment of interaction of the incident wave with the second optical medium all three waves, the incident, reflected and transmitted exists in one point at the same time resulting that their phases must be equivalent which can be written with a condition

$$\omega t - \vec{k}\cdot\vec{r} = \omega_R t - \vec{k_R}\cdot\vec{r} = \omega_T t - \vec{k_T}\cdot\vec{r} \tag{3.4}$$

in a special case of $t = 0$ we can write

$$\vec{k}\cdot\vec{r} = \vec{k_R}\cdot\vec{r} = \vec{k_T}\cdot\vec{r}. \tag{3.5}$$

The directions of reflected and transmitted wave can be determined from the condition found in Eq. 3.5. Knowing that the vector $\vec{r}$ lies in the plane of the interface, the wave vectors of reflected k_R and transmitted k_T waves lie in the plane of incidence. From a geometric construction we obtained a relationship between the incident and reflected wave as

$$kr\cos\left(90^\circ + \theta\right) = k_R r\cos\left(90^\circ + \theta_R\right) \tag{3.6}$$

Because the incident and reflected wave travel in the same environment the $k_R = k$ we concluded

$$\theta_R = \theta, \tag{3.7}$$

that the angle of incidence θ and the angle of reflection θ_R are the same. This is the well known law of reflection. Analogously, in the case of transmitted wave

$$kr\cos(90^\circ + \theta) = k_T r\cos(90^\circ + \theta_T)\,. \tag{3.8}$$

and since

$$k = \frac{\omega}{c} n_1 \tag{3.9}$$

and

$$k_T = \frac{\omega}{c} n_2 \tag{3.10}$$

we get the well known Snell's law (see Fig. 3.2)

$$n_1 \sin(\theta) = n_2 \sin(\theta_T) \tag{3.11}$$

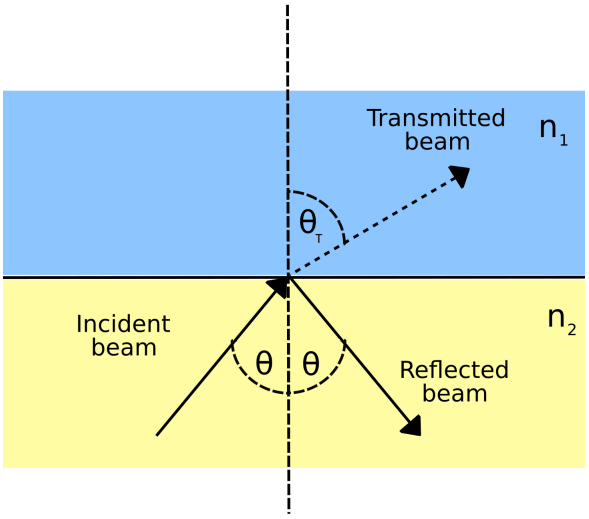

Figure 3.2: Incident light on the interface of two optical gets reflected and transmitted. The reflected light follows the law of reflection where the angle of reflection θ_R is the same as the angle of incident θ. While the transmitted light is governed by the Snell's law with the angle of transmission θ_T.

In the case of optical waveguide such as in Fig. 3.3, where the index of refraction of the core (in our case n_1) is bigger then index of refraction of the cladding (n_2), the Snell's law can be used to determine the critical angle

$$\theta_c = \sin^{-1}\left(\frac{n_2}{n_1}\right) \tag{3.12}$$

above which the condition for total internal reflection is satisfied and optical modes can propagate in dielectric medium.

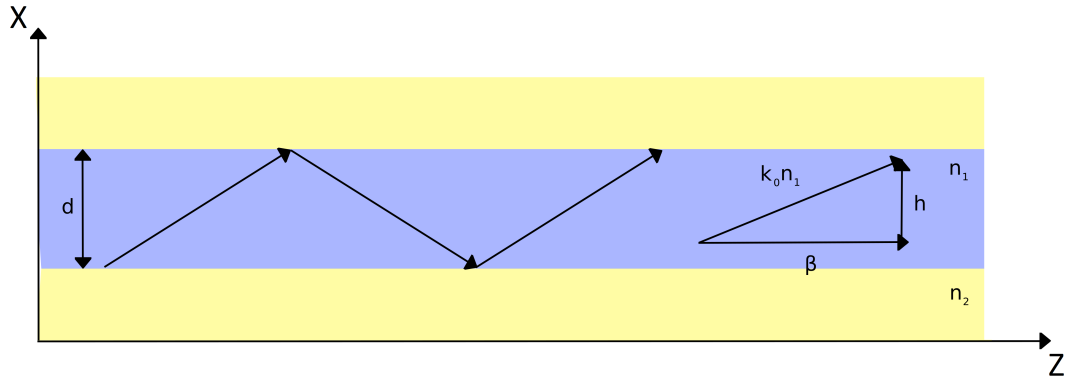

Figure 3.3: Light propagation due to total internal reflection in a 1D optical waveguide.

However, not all waves that travel under total internal reflection can be considered as mode of a waveguide. In such a 1D waveguide structure ,the mode must have a well defined amplitude at each point during propagation and time with a unique propagation constant β [105]. In a optical waveguide with thickness d a propagating wave along the z direction can be defined using expression

$$E(x,z) = E_0(x)\, e^{[i(\omega t - \beta z - hx)]} \tag{3.13}$$

where the $E_0(x)$ is the amplitude profile of the electric field and h is the transverse propagation constant. During its propagation the mode accumulates an additional phase shift ϕ_r. The total acquired phase shift can be expressed as

$$\phi_{tot} = \omega\Delta t - \beta\Delta z - 2hd + 2\phi_r \tag{3.14}$$

where Δt and Δz are incremental changes in time and propagation direction. The additional phase shift ϕ_r can be explained by Fresnel theory for the reflected and transmitted amplitudes of waves at the interface between two optical media. Therefore, the second important requirement for a wave to be a mode of the waveguide is the condition to achieve constructive interference after two reflections at the interface between the core and the cladding

$$-2hd + 2\phi_r = 2m\pi \tag{3.15}$$

where m denotes the ordering of the mode of the structure. Following the threatment reported in [105], ϕ_r can be directly linked to

$$h = \sqrt{(n_1 k_0)^2 - \beta^2} \tag{3.16}$$

$$q = \sqrt{\beta^2 - (n_2 k_0)^2} \tag{3.17}$$

where q denotes the evanescent decay of the mode in the waveguide cladding while h drives the profile behaviour of the transverse electric (TE) field in the core

$$E_m = \begin{cases} A\sin(h\,x) + B\cos(h\,x) & \text{if } |x| < d/2 \\ C\exp(-q\,x) & \text{if } x > d/2 \\ D\exp(q\,x) & \text{if } x < d/2 \end{cases} \tag{3.18}$$

where A, B, C and D are constants that can be derived from the boundary conditions. In the case of m=0 the mode is fundamental. For higher m we have higher order modes with different amplitude distribution. Each mode has a unique propagation constant β_m which is related to the angle of incidence θ for the total internal reflection as

$$\beta_m = k_0 n_1 \sin(\theta_m), \tag{3.19}$$

where $n_1 \sin(\theta_m)$=$n_e(\theta_m)$ is the much used effective index of the propagating mode.

3.2 Channel waveguide

In reality the fundamental structure of any photonic device is an extended (in 3D) 2D channel waveguide. As shown in Fig. 3.4 the structure is composed of its rectangular core embedded in a lower index cladding material.

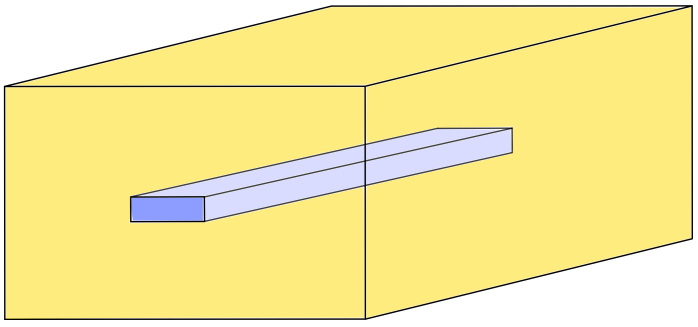

Figure 3.4: 2D channel waveguide embedded in an environment with a lower index of refraction.

At this point we are confined in two dimensions so the solutions are not just pure TE or TM (transverse magnetic) modes. There can also be a solution containing quasi-TE/TM mode where there can be a superposition of both. There are two main practical methods to understand and look up a mode solution for arbitrary waveguide analysis: Effective index method and software mode solvers. For the purposes of this thesis we will discuss only the mode solver method.

3.3 Maxwell's equation for light propagation in dielectric media

Maxwell's equation in a form of a free charge and current are described by the set of differential equations as follows:

$$\nabla \cdot \vec{D} = \rho \tag{3.20}$$

$$\nabla \times \vec{E} = -\frac{\partial \vec{B}}{\partial t} \tag{3.21}$$

$$\nabla \cdot \vec{B} = 0 \tag{3.22}$$

$$\nabla \times \vec{H} = \vec{J} + \frac{\partial \vec{D}}{\partial t} \tag{3.23}$$

where $\vec{E}$ is the electric field, $\vec{H}$ is the magnetic field, $\vec{D}$ and $\vec{B}$ are the electric and magnetic flux density, respectively. The constitutive equations relating the amplitudes of the field to the flux densities are

$$\vec{D} = \varepsilon_0 \vec{E} + \vec{P} \tag{3.24}$$

$$\vec{B} = \mu_0 \vec{H} + \vec{M} \tag{3.25}$$

where ε_0 and μ_0 is the vacuum permittivity and permeability, respectively. Since the materials we worked with were strictly non magnetic, the magnetic polarization $\vec{M}$ was considered to be zero.
$\vec{P}$ is the electric polarization field which in the most cases, when the higher order terms are negligible, can be described by the linear approximation as

$$\vec{P} = \varepsilon_0 \chi^{(1)} \vec{E} \tag{3.26}$$

where $\chi^{(1)}$ is the first order material susceptibility with a direct relationship with relative permittivity of the material

$$\varepsilon = 1 + \chi^{(1)} \tag{3.27}$$

Strictly speaking the material permittivity and permeability are tensor values but in a case of isotropic medium they can be treated as scalar values.
In case when the intensity of the electric field starts to be too strong the higher order terms for the material susceptibility start to be non-negligible and the electric polarization takes a form of

$$\vec{P} = \varepsilon_0 \left[\chi^{(1)} \vec{E} + \chi^{(2)} \vec{E^2} + \chi^{(3)} \vec{E^3} ... \right] \tag{3.28}$$

where $\chi^{(2)}$ and $\chi^{(3)}$ are the second and third order of the material susceptibility, respectively. Under these conditions the polarization vector can be decomposed as a linear part $\vec{P}_L = \varepsilon_0 \chi^{(1)} \vec{E}$ and nonlinear part $\vec{P}_{NL} = \varepsilon_0 \chi^{(2)} \vec{E^2} + \varepsilon_0 \chi^{(3)} \vec{E^3} ...$ which forms the basis for nonlinear optical phenomena.

3.4 Lumerical mode solutions

In order to find a mode of a realistic 2D channel waveguide we had to solve the Maxwell's equations of a wave propagating in a dielectric medium. Unfortunately, finding an analytical solution outside of the ideal example of spherical symmetry, such as in case of a optical fibre where the solutions are Bessel's functions, is impossible. Therefore numerical solutions are the next best option. In order to calculate the field distribution in our SiN waveguides we used a mode solver called Lumerical mode solutions. It uses finite difference method (FDM) as a numerical solver. Imagine a waveguide structure as shown in Fig. 3.5. that is divided into uniform rectangular grids. Now the FDM discretizes the Maxwell's equations for each grid where the spatial increments are defined by the resolution of the mesh. The grids can be reconstructed in a form of a matrix where each eigenvalue corresponds to the propagation constants. Using this matrix reconstruction technique we could obtain the field distribution and the propagation constant where the resolution depends on the size and numbers of the grids.

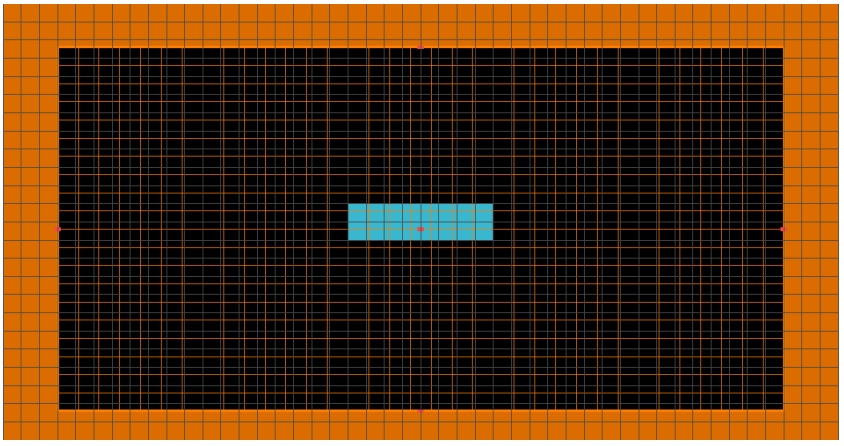

Figure 3.5: Simulation window of Lumerical Mode Solutions for SiN waveguide.

3.4.1 Designing integrated components

There are several considerations that needed to be taken into account when designing a photonic chip. Depending on the purpose of the chip, whether it concerns careful dispersion engineering, maximizing the nonlinear enhancement, minimizing the optical losses or coupling efficiency careful judgement had to be taken into account when deciding the dimensions of the waveguide.
In order to build a photonic chip, these were the main parts that had to be designed
(i) Waveguide
(ii) Inverted taper
(iii) Grating coupler

(iv) Ring resonator
Lumerical Solutions provides both tools for designing the waveguide structure (Mode Solutions) and 3D/2D solver for Maxwell's equation (FDTD Solutions) which were being used to design more complex photonic structures.

3.4.2 Waveguide design

We designed photonic chips to minimize the propagation losses of the waveguide. This decision is justified by the fact that all nonlinear effects strongly depend on the optical losses which will further described in Sec. 5 and Sec. 6.
There are few requirements to design an optimal, low loss waveguide structure:
(i) Sidewall roughness - unlike the fixed material losses, the roughness losses are somewhat controllable. This is due to the possibility of controlling the amount of evanescent field interacting with the sidewall by optimizing the width and height of the structure, and changing the effective index of the TE mode propagating in the waveguide
(ii) Effective index - depends on the dimensions of the waveguide which as mentioned above affects both the propagation losses and nonlinear enhancement. Higher effective index provides higher modal confiment. On the other hand, large dimensional structures tend to be multimoded. This is not an ideal situation because there is a possibility of a power exchange between different modes of the structure, limiting the efficiency of nonlinear processes.

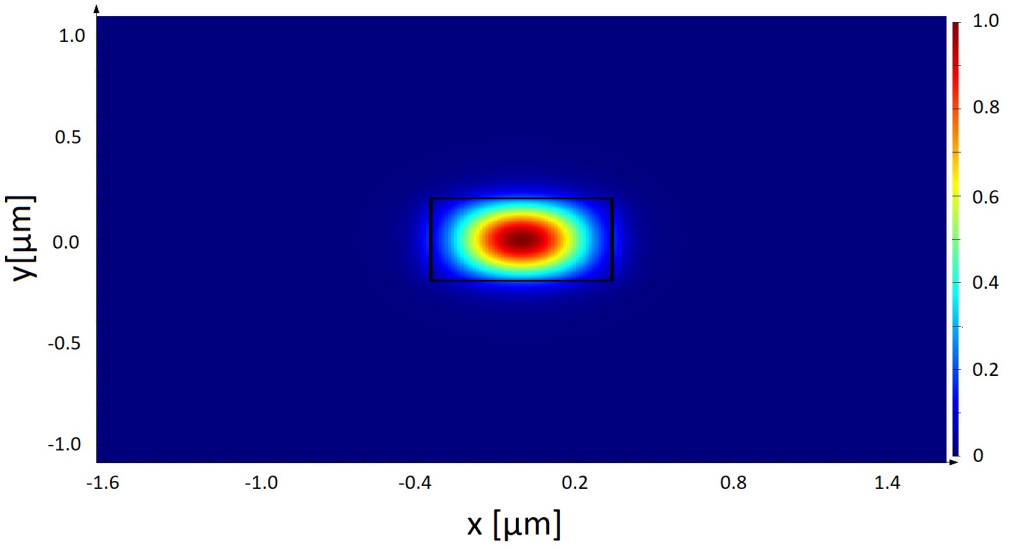

Figure 3.6: Field distribution of the mode in a waveguide with dimensions of 400x700 nm.

Following this conditions, as a starting point, we decided to simulate SiN waveguides with SiO_2 top and bottom cladding design with following properties:
(i) Fixed wavelength at 785 nm.
(ii) The dimensions of our waveguides were 400 nm height times 700 nm width
(iii) The effective index of the first TE mode is 1.82 and second TE mode is 1.64
(iv) Low group velocity dispersion for efficient single photon generation through third order non-linear processes.
The third property (iii) allows us to build two TE moded waveguide structure for higher confined and negligible modal power exchange due to the orthogonality of the solutions of Maxwell equations of our structure. The big difference of the effective indices is enough to prevent any intermode coupling even when the perturbations of the structure like bending is presented. The structure and the mode distribution is shown in Fig. 3.6.

3.4.3 Taper design

To couple light from optical fibres to our Si_3N_4 chip we used gratings and taper sections [106]. The goal of the taper is to reshape the optical mode between two different cross sections of the coupler and the waveguide. This is done by adiabatically change of the size of the mode (Fig. 3.7). From the transverse size of the coupler (13 μm) to the size of the waveguide (700 nm) the taper should be long enough to achieve unit transmission. Following the simulation results shown in Fig. 3.8 we designed the length of the taper to be 350 μm.

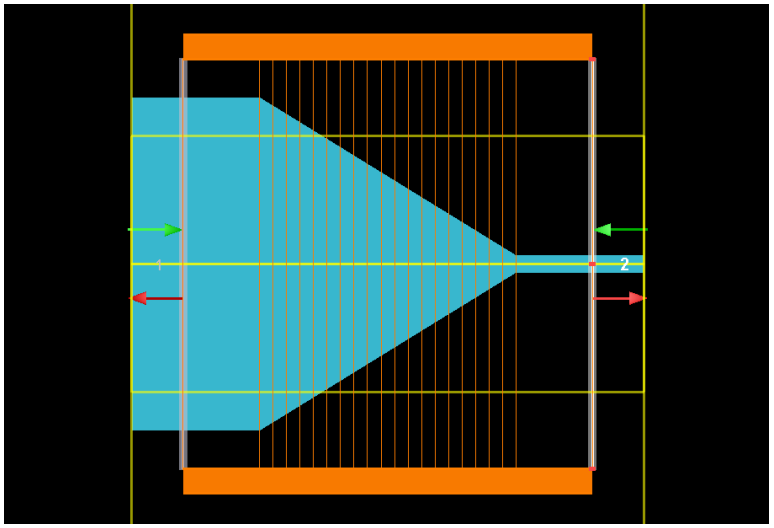

Figure 3.7: Simulation window of a Mode Solutions software to design an efficient taper structure.

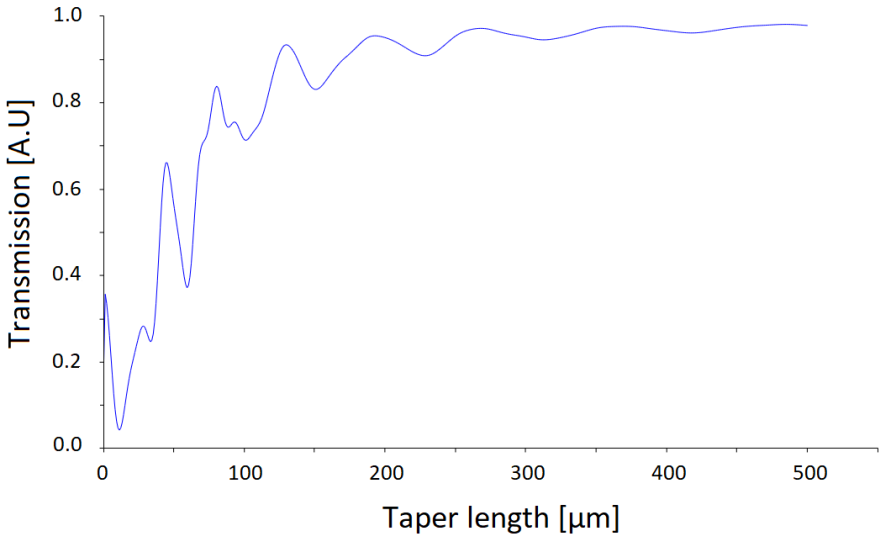

Figure 3.8: Transmission of the fundamental TE mode from the multimode part of the taper to the waveguide structure. While the taper is short the transmission oscillates due to mode coupling to the radiative and higher order modes. When the taper length reaches 350 μm the TE mode is coupled to the waveguide with near unit efficiency.

3.4.4 Grating coupler design

In order to efficiently couple light from the single mode fibre to the waveguide we decided to design a grating coupler [107], [108], [109] shown in Fig. 3.9. It has several advantages over the conventional butt-coupling technique such as the comparable coupling efficiency, wide bandwidth and obviation of polishing or anti-reflection coating. The mode matching condition for grating couplers is defined as

$$-\frac{n_c}{\lambda}\sin(\theta)+\frac{n_W}{\lambda}=\frac{1}{\Lambda}, \tag{3.29}$$

where n_c is the index of refraction of top cladding, n_W is the index of refraction of the waveguide, λ is wavelength in vacuum and Λ is period of the grating, θ is the angle of the single mode fibre. Simulation results are shown in Fig. 3.10

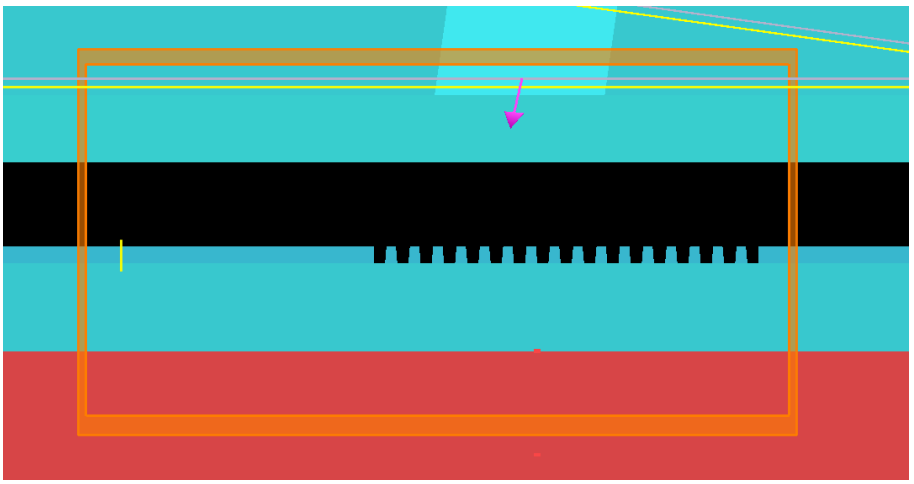

Figure 3.9: Simulation window of a FDTD software to design an efficient grating coupler.

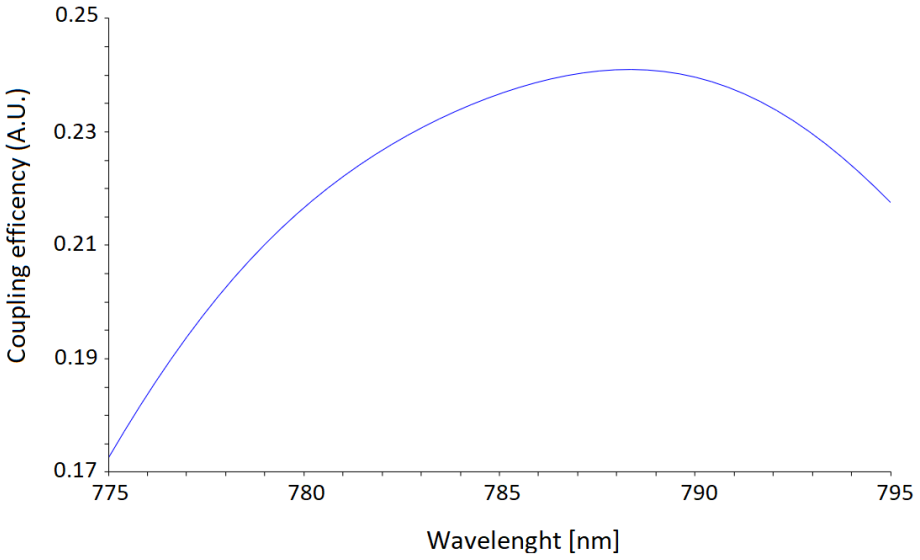

Figure 3.10: Coupling efficiency of a 400 nm thick grating coupler with a period $\Lambda = 0.554$ μm, incident angle $\theta = 8°$. Bottom blue rectangle is SiO_2 with thickness of 2 μm while the top blue rectangle is air. The rest is black filling with a refractive index of oxide.

3.4.5 Ring resonator design

The range of applications where ring resonators play a key role is enormous. They were used as a high rejection filters, modulators, sources of nonclassical light and a key component to estimate propagation losses of the waveguide structure. Therefore, designing and understanding the properties of a microring resonators are essential. A

ring resonator is an optical cavity where the travelling wave circulates around bended waveguide. Suppose we have a optical field with an amplitude A_1 in the bus waveguide such as shown in Fig. 3.11.

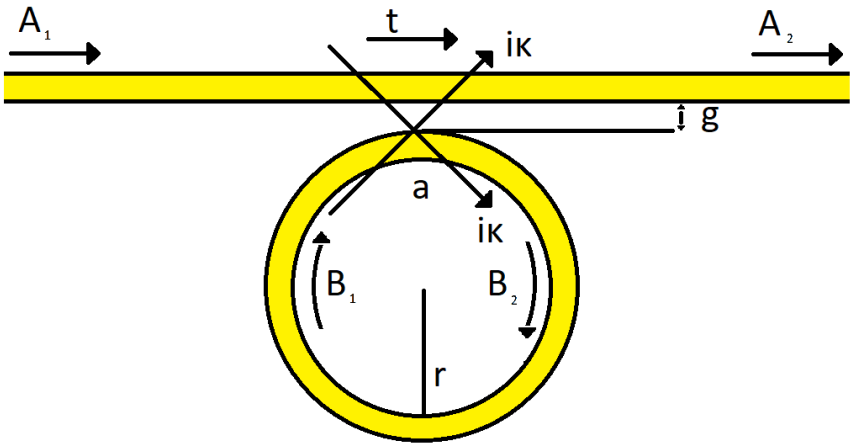

Figure 3.11: Ring resonator and bus waveguide.

The distance g between the bus and the the ring defines the transmission coefficient t and coupling coefficient κ. Therefore the amplitude of the transmitted wave is $A_2 = tA_1$ and the amplitude of the coupled wave is $B_2 = i\kappa A_1$. The travelling wave B_2 in the ring feels internal ring losses from the material, bending of the waveguide and scattering from the sidewall roughness. Therefore, the amplitude of the travelling wave at the end of one round trip is $B_1 = ae^{i\phi(\lambda)}B_2$, where the round trip losses are $a = e^{\alpha\pi r}$ identified with the intrinsic loss α of the ring resonator structure.
We describe the resonance condition in a case when the travelling wave A_1 constructively interferes with the travelling wave B_1 that made one round trip in the ring. In this condition the phase of both waves are identical and can be described as

$$\phi(\lambda) = \frac{2\pi n_e(\lambda)}{\lambda} 2\pi r \tag{3.30}$$

where r is the radius of the ring resonator, $n_e(\lambda)$ is the effective index of the bend waveguide and λ is the operating wavelength. From this equation we can conclude that a resonance condition can occur whenever the ϕ is a multiple integer of 2π. The spacing between the neighbour resonances as free spectral range

$$FSR(\lambda) = \frac{\lambda^2}{2\pi r n_g(\lambda)}, \tag{3.31}$$

where $n_g(\lambda)$ is the group index of the material. The transmission spectrum of the ring resonator can be obtained by following the mathematical treatment in [110], [111], [112], [105]

$$P_T(\lambda) = \left|\frac{A_2}{A_1}\right|^2 = \frac{a^2 + t^2 - 2at\cos(\phi(\lambda))}{1 + a^2t^2 - 2at\cos(\phi(\lambda))}, \tag{3.32}$$

When the resonance condition is met the transmitted power is

$$P_T(\lambda_0) = \frac{(a-t)^2}{(1-at)^2} \tag{3.33}$$

From Eq. 3.33 we can see that we have zero power transmission for the case when the round trip losses are equal to the transmission coefficient. This condition is called critical coupling.

In order to measure the losses (coupling and ring) from the transmission spectrum of the ring resonator we have to define its quality factor Q. Q-factor shows how well our resonator stores energy inside of the ring. We can write it as

$$Q = \frac{\lambda_0}{\Delta\lambda_{FWHM}}, \tag{3.34}$$

where λ_0 is the resonance wavelength and $\Delta\lambda_{FWHM}$ is the wavelength interval of the full width half maximum. The Q-factor defined in Eq. 3.34 contains all losses from the microring system, therefore we reinterpret the Q as

$$Q_L^{-1} = Q_i^{-1} - Q_c^{-1}, \tag{3.35}$$

where $Q = Q_L$ is the Q-factor from the measured linewidth of the resonance, Q_i is the intrinsic Q-factor of the ring resonator without the account of any additional losses and Q_c is are coupling losses from the waveguide to the ring. From the matrix formalism [111] we could further obtain

$$Q_L = \frac{\sqrt{ta}L\pi n_g}{(1-at)\lambda_0}, \tag{3.36}$$

where n_g is the group index and L is the circumference of the ring resonator. If the coupling gap g is engineered in such a way that we are close to the critical coupling and the round trip losses are negligible we could describe the intrinsic quality factor as

$$Q_i \approx \frac{k_0 n_g}{\alpha}. \tag{3.37}$$

In other cases than the critical coupling condition, we were still able to obtain the losses of the ring resonator following these relations

$$Q_c = \begin{cases} \frac{2Q_L}{1-\sqrt{T_{min}}} & \text{for undercoupled regime } a < t \\ \frac{2Q_L}{1+\sqrt{T_{min}}} & \text{for overcoupled regime } a > t \end{cases} \tag{3.38}$$

where T_{min} is the relative minimum of the measured resonance. There are two solutions to Eq. 3.36 The first scenario describes the undercoupling condition where the internal loss is smaller than the transmission coefficient. On the other hand, whenever the loss is bigger than the transmission coefficient, we refer to it as overcoupling condition. To estimate the propagation losses it is most convenient to measure a resonance in critical coupling condition, where $T_{min} = 0$. This condition is experimentally very unlikely and usually we obtain condition where $T_{min} \neq 0$. Thus, when designing a photonic chip, we fabricated several ring resonators with varying size of the gap, to estimate the coupling condition and therefore retrieve the loss of the structure. Further, in the next Chapter, we shown some measurements and loss estimation using equations from above.

Chapter 4

Silicon Nitride Waveguide And Ring Resonator Losses

4.1 Introduction

In this chapter we discuss several important characteristic properties of SiN. We introduce ellipsometry as a effective way to measure refractive index that is related to the material dispersion which defines the phase matching condition for efficient realization of nonlinear optical phenomena. Then we describe several measurement methods to retrieve the propagation losses at both visible and telecom wavelengths that are an important aspect of any photonic technology.

4.2 Ellipsometer measurements

Ellipsometry is a must have tool in any nanofabrication center. It is an interferometric technique that measures a polarization change from an initially linearly polarized light beam, reflected from the surface of the tested film. The acquired phase difference depends on the film's thickness and refractive index contrast between the substrate and the material of interest. Therefore, the most common choice of substrate is Silicon. The collected data are afterwards fitted with a particular model from which we can retrieve several parameters. These are then used to obtain optical properties of the dielectric material that are necessary for the fabrication process. The ellipsometer Woolham M-2000, in particular, offers a quick evaluation of layer thickness and it has been vastly used together with the ICP RIE to determine etching rates and selectivities with respect to the resist. Very important parameter that can be easily extracted is the index of refraction. Using the Cauchy model in the transparent window of the material

$$n(\lambda) = A + \frac{B}{\lambda^2} + \frac{C}{\lambda^4}, \tag{4.1}$$

we can reconstruct the material dispersion of SiN shown in Fig. 4.1 and obtain the important index of refraction. The parameters A, B, C are retrieved from the ellipsometry measurement.

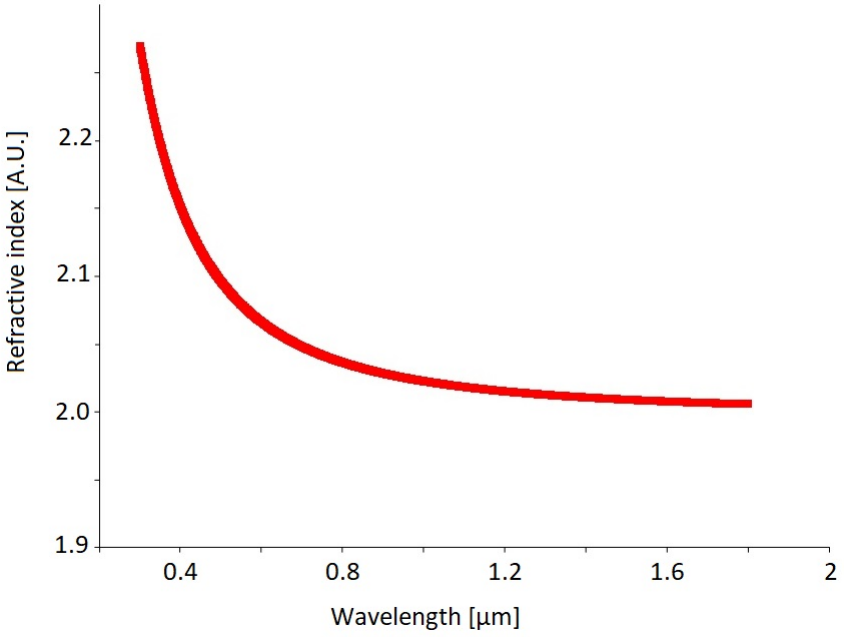

Figure 4.1: Dispersion relation of 400 nm thick SiN deposited by PECVD machine on top of a SiO_2.

4.3 Material and waveguide losses

The contribution to propagation losses in optical waveguides could arise from several distinct sources. Scattering losses are a result of an overlap between the evanescent field with the sidewall roughness at the interface of the core and the cladding. As the field overlap scales exponentially with size it can be assumed that for a very thick and wide device the losses are approximated to the one of the bulk material. Unfortunately, such waveguides are highly multimoded and therefore possible losses from mode coupling between fundamental and higher order modes could arise in the presence of any surface inhomogeneity. Even though it is slightly impractical it is possible to smoothen out the top and bottom roughness by chemical mechanical polishing (CMP). Also, there are several techniques to improve the sidewall roughness such as resist reflow, oxidation and well characterised etching chemistry. The absorption loss originates from the defects of the material and the surface states at the interface between the core and the cladding. It is entirely possible to engineer the absorption properties by adequately choosing the deposition parameters. For PECVD SiN it has been measured that losses down to 0.1 dB/cm at visible wavelengths could be achievable in planar waveguides.

Finally, when light propagates in a bent waveguide it is exposed to two types of loss. First, it increases the scattering loss due to higher overlap with the sidewall roughness. Second, a possible field leakage in radiative modes can occur as a result of smaller mode confinement in sharp bends or mode mismatch at the interface between the straight and bent section of the waveguide. Ultimately, radiation losses are major restriction to the size of the ring resonator. They are described by equation

$$\alpha_R \approx e^{-\Delta n_{eff} R} \tag{4.2}$$

where R is the radius of the ring and Δn_{eff} is the difference between the effective index of the mode in the waveguide and refractive index of the cladding. Therefore, we can conclude from Eq. 4.2 that overall size of the photonic device is govern by Δn_{eff}. As the refractive index contrast gets bigger, more components can be integrated on a single wafer.

4.4 Setup

In order to measure the the waveguides propagation losses and the performances of the ring resonators we build an experimental setup which helps us to couple light in and out of the photonic chip to measure the transmitted power. As a source for our measurement we used tunable, fiber-coupled 785 nm DBR laser diode from Thorlabs. Its mode hop free tuning range starts from 784 nm to 786 nm, well enough for a linewidth measurement of a ring resonator. We connect the laser with a polarization maintaining fiber designed at 780 nm from Thorlabs. The fiber was connected to another PM fiber array polished at 8 degrees and spaced by 250 μm from OZ Optics to couple light in and out from the chip. At the end we measure the power by a Thorlabs PM100D power meter. To measure the propagation losses at the telecom band we used a tunable TSL-510 type A Santec laser and changed the fiber optics for the appropriate wavelength. The setup is shown in Fig. 4.2

Before an actual measurement we prepare a script which automatize the control of the laser and saves the data measured by the power meter. We use a LabView programme for this task.

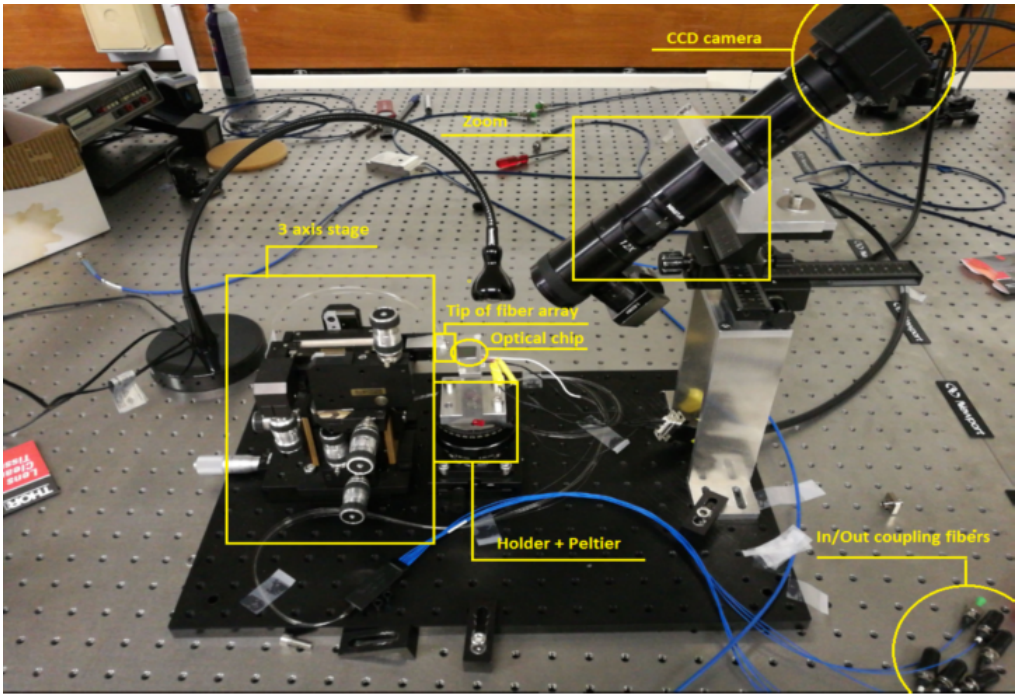

Figure 4.2: Experimental apparatus to characterise the performance of waveguides and ring resonators.

4.5 Cut-back method

There are several methods to estimate propagation losses in optical waveguides. One of the most used one is cut-back method. The name originates from literally cutting the optical fibers to measure losses with different lengths. The measured transmission can be broken into two distinct parts concerning losses of the fiber and coupling losses. In the estimation one considers the coupling efficiency to be equal from both sides. In case of the waveguides we design different lengths of waveguides and measure their transmission. This method is not the most reliable since there is a high possibility that any imperfection can occur on very long waveguides that can affect the results. We fabricate waveguides that were 0.5μm thick and 1μm - 2μm wide to obtain propagation losses of 5.3 dB/cm and 1.3 dB/cm at 785 nm and 1550 nm, respectively. As a top cladding we use 2μm thick layer of PMMA. First we measure losses in the near visible range. Afterwards we remove the polymer by putting the sample in an NMP solvent and leave it for 10 minutes at 80 degrees in an ultrasonic bath. Next we anneal the nitride at 1200 degrees for 3 hours in N_2 atmosphere and respin PMMA to estimate losses at 1550 nm. The results are shown in Fig. 4.3. The curves resemble typical exponential behaviour following the relation

$$P_{out} = P_{in}e^{-\alpha L}, \tag{4.3}$$

where α are the estimated propagation losses and L is the length of the waveguide. The difference in output power is due to higher coupling efficiency of the grating couplers.

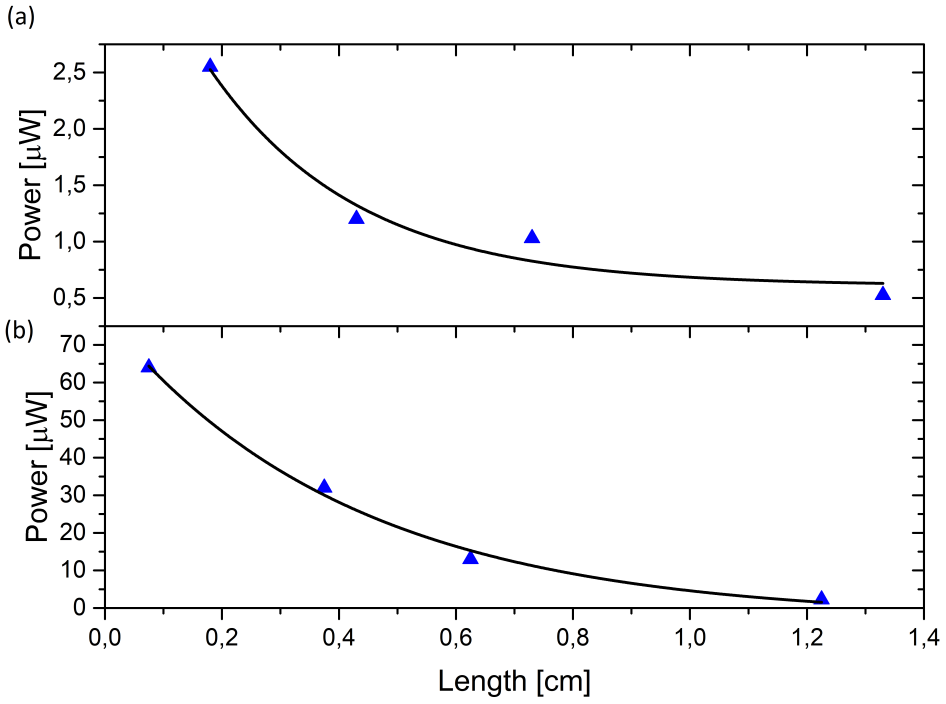

Figure 4.3: Measured propagation losses using Cut-back method at (a) 785 nm and (b) 1550 nm.

4.6 Ring resonator losses

Another method to evaluate the losses of an optical structure is based on measuring the linewidth of an integrated optical resonator. In comparison to cut-back method, resonance measurement is much more robust as the ring is a much smaller structure and therefore imperfections of the ring waveguide are less probable. Also coupling efficiencies of the grating couplers are not important as long as there is some transmitted power and the light couples to the fundamental mode to the ring. Using the same experimental setup as in previous section we show in Fig. 4.4 and Fig. 4.5 an examples of measured resonance spectrum of a ring resonator with 19 μm radius for visible wavelengths and a 80 μm radius cavity for telecom, respectively. Furthermore, by fitting resonance spectra with Lorentzian function we retrieve the respective full widths half maxima (FWHM), and using Eq. 3.34, Eq. 3.36, Eq. 3.38 and Eq. 3.35 we estimate the propagation losses of 2.1 dB/cm and 2.6 dB/cm for visible and telecom spectrum, respectively.

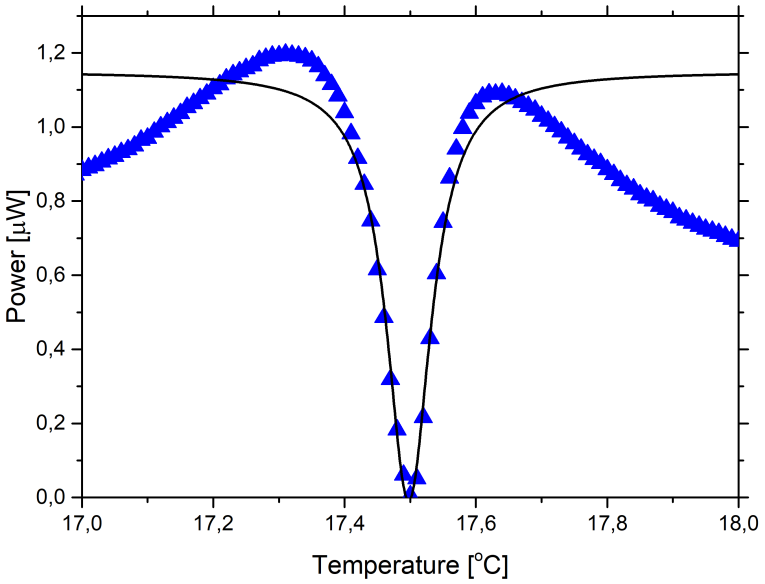

Figure 4.4: Example of measured resonance spectrum of a critically coupled ring resonator with 19 μm radius and spectral linewidth $\Delta\lambda$ of 4.7 pm. The estimated optical losses are 2.1 dB/cm.

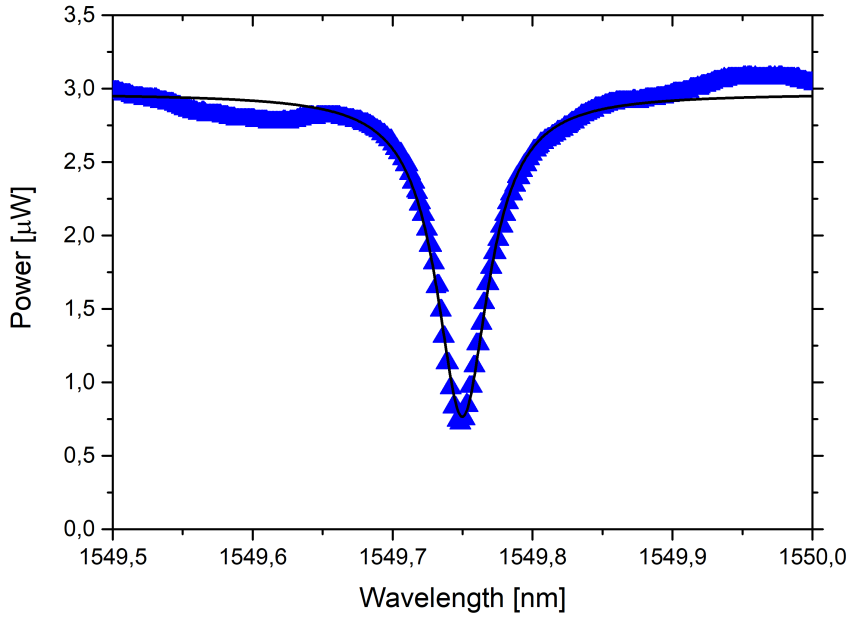

Figure 4.5: Example of measured resonance spectrum of an overcoupled ring resonator with 80 μm radius and spectral linewidth $\Delta\lambda$ of 45 pm. The estimated optical losses are 2.6 dB/cm.

In order to obtain low loss SiN, reducing the sidewall roughness must be a priority. The imperfections depend on both, the lithography step and the etching recipe. We use an optimized dose and shot step during the e-beam lithography and together with an adequate setting of deposition parameters we obtain resonators with high quality factors at visible range. To understand whether the sidewall roughness is limiting the performance of the resonators, we fabricate rings with different radii. As we start with the smallest radius, the overlap of the field with the sidewall of the waveguide is the biggest. When we increase the radius we decrease the overlap and therefore we are able to estimate whether roughness is the major limitation of our fabrication technology. We can conclude from Tab. 4.1 that the losses for different ring sizes are more or less equal, which means our fabrication is not limited by the sidewall roughness but rather by the material itself.

	19 μm ring	**40 μm ring**	**60 μm ring**	**80 μm ring**	**100 μm ring**	**120 μm ring**	**140 μm ring**	**160 μm ring**
Losses [dB/cm]	2.24	2.3	2.35	3.07	2.08	2.25	2.21	2.29

Table 4.1: Characterisation of the sidewall roughness at 785 nm. As we increase the radius of the ring resonator we decrease the overlap with the sidewall.

In order to improve the optical response even more, an effort needs to be put on characterising the recipe for the top cladding. We start with a reference process using PMMA as top cladding. If after each time we conclude that the fabrication results is comparable, we remove PMMA and deposit SiO_2 TEOS with different parameters and compare the obtained results. We change the flow of argon present in the deposition process. The amount of argon changes the deposition rate and the size of particles hitting the surface during the deposition. This is a physical process and therefore shapes the the top roughness of our waveguide. Another variable in our process is an additional annealing step using different gasses in the furnace. This step ensures a decrease of silicon nanoclusters that might have been formed during the deposition process and thus could increase the material absorption. We show the result of these steps in Tab. 4.2. We see that the lowest losses are achievable in case where we deposit TEOS without any present Ar. This is due to decreased level of bombardment from heavy Ar particles. Also we should note that annealing SiN does not improve the loss significantly. Furthermore, we have the option to characterise the LPCVD SiN deposition process developed in our cleanroom (Tab. 4.3). We make a linear characterisation for different thicknesses of the waveguide and different annealing steps but we conclude that the process has not improved so much in comparison to the PECVD SiN.

PMMA	TEOS 0 Ar flow	TEOS 50 Ar flow	TEOS 120 Ar flow	SiN annealed in N_2	SiN annealed in Ar	TEOS 0 Ar flow annealed in Ar	TEOS 0 Ar flow annealed in O_2	Losses [dB/cm]
YES	NO	NO	NO	NO	NO	NO	NO	2.90
NO	YES	NO	NO	NO	NO	NO	NO	2.80
NO	NO	YES	NO	NO	NO	NO	NO	2.96
NO	NO	NO	YES	NO	NO	NO	NO	4.06
YES	NO	NO	NO	YES	NO	NO	NO	2.29
YES	NO	NO	NO	NO	YES	NO	NO	2.72
NO	YES	NO	NO	NO	NO	YES	NO	2.24
NO	YES	NO	NO	NO	NO	NO	YES	3.07
NO	YES	NO	NO	YES	NO	YES	NO	1.95

Table 4.2: Linear characterisation of PECVD deposition process at 785 nm for different top claddings and annealing processes which was performed at 1200 °C. YES - means that either annealing step or cladding with specific chemistry is present on the final chip.

PMMA	210 nm thickness	410 nm thickness	1st deposited layer annealed in N_2	2nd deposited layer annealed in N_2	Losses [dB/cm]
YES	YES	NO	NO	NO	3.9
YES	YES	NO	YES	NO	2.3
YES	NO	YES	NO	NO	3.1
YES	NO	YES	YES	NO	2.74
YES	NO	YES	YES	YES	1.72

Table 4.3: Linear characterisation of LPCVD deposition process at 785 nm for different top claddings and annealing processes which was performed at 1200 °C. YES - means that either annealing step or cladding with specific chemistry is present on the final chip.

4.7 Conclusion

In conclusion we studied several effects on optical losses in the ring resonator in order to optimize our fabrication process. We conclude that the sidewall roughness has an negligible effect on the overall propagation losses. Increasing the thickness of our ring resonators might increase the quality factor. Moreover, we found that the best cladding for our chips is TEOS deposited without additional argon. Further optimization steps such as reflow, CMP and using TEOS as a hardmask in order to minimize material redeposition in the ICP RIE chamber might improve the fabrication process but consequently more effort should be put on the development of PECVD deposition to obtain lower material absorption.

Chapter 5

Integrated Single Photon Sources And Detectors

In this chapter we discuss the generation of non-classical states of light through spontaneous four wave mixing (SFWM) process that has been an essential source regarding many integrated quantum photonic experiments [113],[114],[115]. Furthermore, we also describe the enhancement process of light-matter interactions that can be achieved by microring resonators due to constructing interference yielding to an efficient production of time-bin entangled photons. The enhanced generation rate of single photons relies on high quality factor Q and small modal volume V of the resonator, therefore the low loss and small radius we described in previous chapter is a highly desirable achievement. Moreover, most intensive investigation of on chip integrated sources has been focused mainly at telecom range [70],[116],[73] which has been highly motivated for the straightforward application in quantum cryptography systems due to a long history of classical communications via low loss optical fibres [117]. On the other hand, the downfall of working at telecom wavelengths resides in the use of high performance superconducting detectors working at cryogenic temperatures that limits the scalability and potential commercialization of these devices. Placing the sample in a cryostat also precludes the use of modulators based on the thermo-optical effects, commonly used in present silicon devices for quantum optics [70]. In order to avoid working in cryogenic temperatures, we investigate in this chapter the photon pair generation in the near visible region, on a photonic chip fabricated with steps compatible with back end of line CMOS processes. Furthermore, we collaborate with Dr. Alberto Tosi (Politecnico of Milan) to fabricate SiN photonic components on a chip containing silicon avalanche photodetectors, that are accessible from a standard CMOS foundry and could potentially lead to a fully integrated quantum photonic simulator working at room temperature, which we discuss at the end of this chapter. Parts of this chapter are based on work published in [8]. My

contribution in the published manuscript covers the device fabrication, building the experimental apparatus, measurement and data analysis while Francesco Martini provides the design of apodized grating couplers.

5.1 Resonantly enhanced optical nonlinearities

In this section we discuss the nonlinear optical effects in a Kerr medium that has been the basis for many interesting phenomena such as second and third harmonic generation, spontaneous parametric down and upconversion, stimulated and spontaneous four wave mixing process. Here we focus on a SFWM process and its enhancement in integrated ring resonators.

5.1.1 Four wave mixing in Kerr nonlinear media

When four waves propagate through a nonlinear Kerr medium they can couple one to another via the intrinsic third order polarization vector of the material

$$\vec{P}_i^{NL} = \epsilon_0 \chi^3_{ijk} \vec{E}_i \vec{E}_j \vec{E}_k \tag{5.1}$$

where χ^3_{ijk} is a third order tensor of the material susceptibility that determines the coupling strength in between the waves. In the case of degenerate FWM ,where the two waves of the pump have the same frequency ω_p, FWM can be seen as a four photon scattering process where a field at the signal frequency ω_s can be converted to a field at an idler frequency $\omega_i = 2\omega_p - \omega_s$ (Fig. 5.1). The frequency conversion does not involve any loss mechanism during the scattering effect and therefore the energy and momentum relations needs to be conserved:

$$2\omega_p = \omega_i + \omega_s \tag{5.2}$$

$$2k_p = k_i + k_s. \tag{5.3}$$

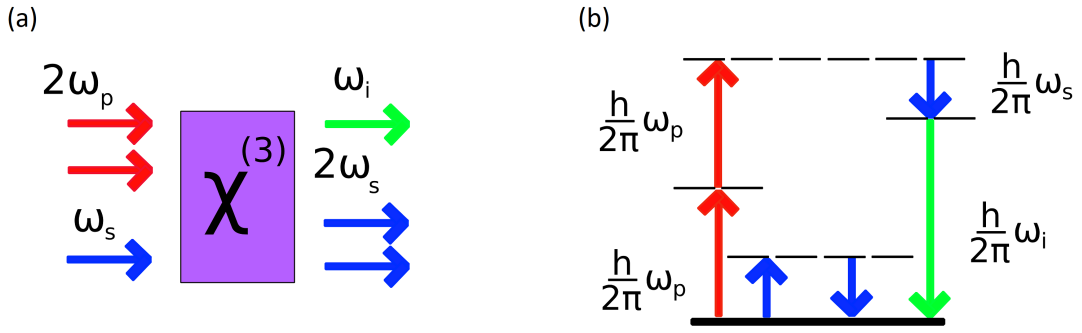

Figure 5.1: (a) Input output conversion of photons interacting in a χ_3 nonlinear Kerr medium. (b) Schematic representation of an energy diagram DFWM process stimulated by a signal field. The solid line is the ground state level while the dashed represent the virtual level.

In order to understand the main properties of FWM process, we consider that the pump field is much stronger than the signal and idler powers. Following the threatment in [118], [119] we can obtain the dynamical equations describing the coupling in between the waves that propagate in the z direction of the nonlinear medium:

$$\frac{\partial E_p}{\partial z} = -\frac{\alpha_p}{2}E_p + i\gamma|E_p|^2E_p \tag{5.4}$$

$$\frac{\partial E_s}{\partial z} = -\frac{\alpha_s}{2}E_s + 2i\gamma|E_p|^2E_s + \gamma E_p^2E_i^*e^{-i\Delta kz} \tag{5.5}$$

$$\frac{\partial E_i}{\partial z} = -\frac{\alpha_i}{2}E_i + 2i\gamma|E_p|^2E_i + \gamma E_p^2E_s^*e^{-i\Delta kz} \tag{5.6}$$

where the first term on the right hand side of Eq. 5.4-5.6 is responsible for the attenuation $\alpha_p = \alpha_s = \alpha_i$ of the pump, signal and idler photons, the second term in Eq.5.4 describes the selfphase modulation of the pump beam while Eq.5.5 and 5.6 take into account cross-phase modulation effect of the pump on the single photons. Finally, the last term in Eq.5.6 is responsible for the FWM process that depends on quadratically on the pump amplitude and linearly on the nonlinear optical coefficient γ that describes the strength of the process. Another important parameter defining the efficiency of the FWM process is the phase mismatch

$$\Delta k = 2k_p - k_s - k_i. \tag{5.7}$$

Since in most practical cases we consider the pump being much more intense the the two opposing beams, the crossphase modulation effect produced by signal and idler can be neglected.

5.1.2 Spontaneous FWM in ring resonators

As mentioned in Chapter 3, an integrated ring resonator is an optical device that can enhance the intracavity power of the pump due to constructive interference effect between the circulating and coupling wave. Such a device has enormous possibilities to enhance many nonlinear effects only with just few mW of continuous power.
Spontaneous FWM (SFWM) process is a nonlinear phenomena where the signal beam is not present in the conversion process. This can be justified by the fact that the signal photon does not contribute to the energy transfer between the waves. For that reason, an efficient SFWM process can be "stimulated" by vacuum fluctuations that satisfy the energy and phase matching condition. This can be seen as a four particle elastic process where two pump photons annihilate in order to produce correlated pair of single photons (Fig. 5.9). The photons are entangled in energy and time and such a process where vacuum fluctuations drive the conversion is called parametric process. There is no classical explanation for such process and it can be only described in quantum optics theory.

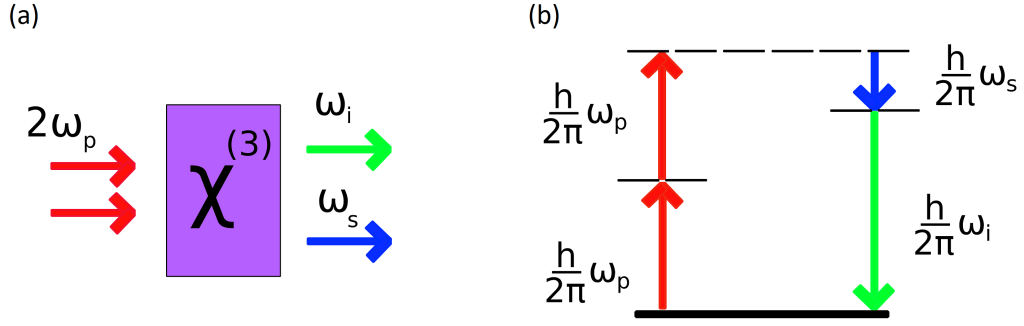

Figure 5.2: (a) Input output conversion of photons interacting in a χ_3 nonlinear Kerr medium. (b) Schematic representation of an energy diagram of SFWM process "stimulated" by vacuum fluctuations at ω_s and ω_i. The solid line is the ground state level while the dashed represent the virtual level.

The formalism is briefly described here but we refer the readers to [120] for more detailed explanation. We imagine a coherent pump that propagates in the waveguide in the z direction. In this model we consider a situation where the pump is coupled to the ring with radius R at a point $z = 0$. The Hamiltonian of the system can be written as

$$H = H^{ch} + H^{cp} + H^{R} \tag{5.8}$$

where the Hamiltonian of the waveguide is

$$H^{ch} = \sum_{\mu} \left[\hbar\omega_{\mu} \int dz \psi_{\mu}^{\dagger}(z)\psi_{\mu}(z) + \frac{i}{2}\hbar v_{\mu} \int dz \left(\frac{\partial \psi_{\mu}^{\dagger}(z)}{\partial z}\psi_{\mu}(z) - h.c. \right) \right], \tag{5.9}$$

the coupling Hamiltonian between the channel and the ring is

$$H^{cp} = \sqrt{2\pi}\hbar \sum \left[c_\mu b^\dagger \psi_\mu(0) + h.c. \right], \tag{5.10}$$

and the Hamiltonian of the ring resonator is

$$H^R = \sum_\mu \hbar\omega_\mu b_\mu^\dagger b_\mu - \sum_{\mu_1\mu_2\mu_3\mu_4} S_{\mu_1\mu_2\mu_3\mu_4} b_{\mu_1}^\dagger b_{\mu_2}^\dagger b_{\mu_3} b_{\mu_4}. \tag{5.11}$$

In the equations above we define the mode μ with an eigenfrequency ω_μ and a group velocity v_μ. The ψ_μ and b_μ are the field operator of the bus waveguide and ring resonator that are coupled to each other via the coupling constant c_μ. The term $S_{\mu_1\mu_2\mu_3\mu_4}$ corresponds to nonlinear effects in the ring. Applying the Hamiltonian from Eq. 5.8 on the coherent state that is coupled to the resonance at the pump frequency generates state at the resonances of the signal and idler frequencies in the form of two mode squeezed vacuum

$$|\Psi_{gen}\rangle = e^{\beta C_{II}^\dagger - h.c.} |00\rangle, \tag{5.12}$$

where

$$C_{II}^\dagger = \frac{1}{\sqrt{(2)}} \int d\omega_s d\omega_i \phi(\omega_s\omega_i) a_{\omega_s}^\dagger a_{\omega_i}^\dagger \tag{5.13}$$

and $\phi(\omega_s\omega_i)$ is the bi-photon function that must satisfy $|\phi(\omega_s\omega_i)|^2 = \delta(\omega_s + \omega_i - 2\omega_p)$ in a CW regime. The $|\beta|^2$ is recognized as the probability of the photon pair generation and if we consider $|\beta| << 1$ the output state is defined as

$$|\Psi_{gen}\rangle \approx |00\rangle + \beta|II\rangle. \tag{5.14}$$

Overall, we are interested in the main result of [120]

$$P_i^{SP} = (\gamma 2\pi R)^2) \left(\frac{2Q}{k_\mu 2\pi R} \right)^3 \frac{\hbar\omega_s v_g}{4\pi R} P_p^2 \tag{5.15}$$

that makes an important connection between the quality of the ring and the generation rate. Eq. 5.15 refers to a special case of critically coupled ring resonator from which we can conclude that the generation of the correlated pairs of photons depends on three important parameters: size of the ring, losses and nonlinear enhancement of the waveguide that is inversely proportional to the waveguides effective area A_{eff}. Therefore, all this criteria need to be careful optimized to obtain the best results.

5.2 Generation of entangled pairs of in the visible spectrum

Here we describe the experiment regarding generation of single photons at 785 nm. We start with the design and precise fabrication process. Then we measure the spectrum of the ring resonator which we conduct the experiment on. Afterwards we build the setup and characterise the generation rate and the performance of the single photon source in terms of coincidence to accidentals ratio (CAR).

5.2.1 Design, fabrication and characterisation of the photonic chip

Design

The chip design was aimed to optimize the light confinement and propagation loss. Thus, we design devices with dimensions of 400 x 700 nm, showing a multi-mode behaviour. The fundamental TE mode used for this experiment is reported in (Fig. 5.3.

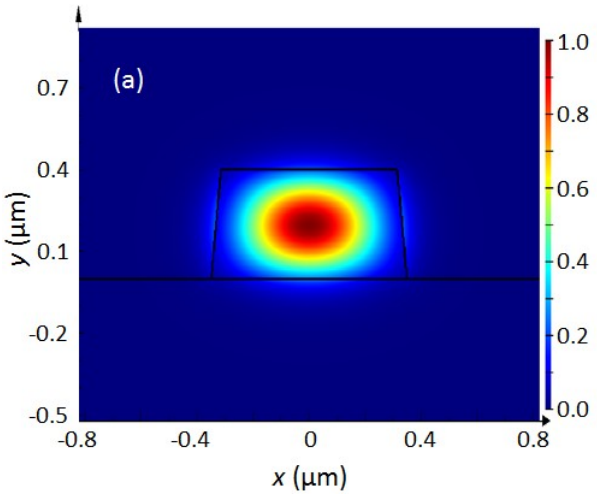

Figure 5.3: Fundamental TE mode of the waveguide with dimensions of 400x700 nm.

To couple light from SiN waveguides to optical fibers, we optimize the apodized gratings following the algorithm described in reference [121]. The optimization algorithm and design was made by my colleague Francesco Martini. In order to reduce lithography steps we design the gratings to be fully etched, while apodization maintains a simulation coupling efficiency of 38% and a 3 dB bandwidth of more than 20 nm, as shown in Fig. 5.4. We use mode converters to reshape the optical mode adiabatically to minimize coupling losses to higher order modes while the transverse size of the waveguide is changing from 13 μm to 700 nm in a length of 350 μm.

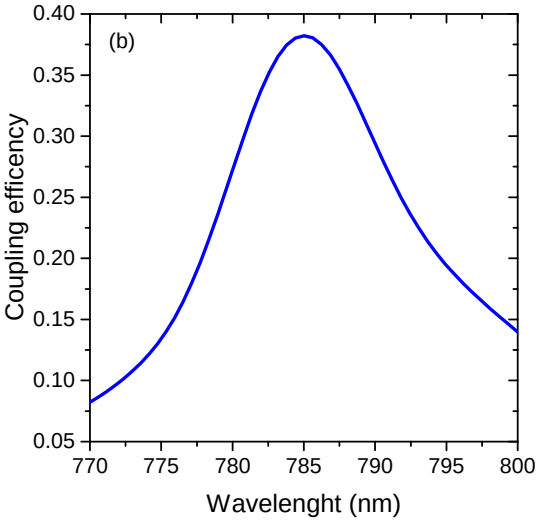

Figure 5.4: Coupling efficiency of an apodized grating coupler.

Fabrication and linear characterisation

The nanofabrication starts from a 2 μm of low loss thermal SiO_2 grown by wet oxidation on top of a standard silicon wafer. Then we deposit 410 nm PECVD SiN with a 5:2 ratio of NH_3:SiH_4 to minimize the amount of silicon nanoclusters [103], showing a refractive index of 1.97 at 785 nm. We dice the samples and spin with 450 nm of CSAR, before exposing them with an electron beam lithography system JEOL JBX-9300FS. After the lithography step we develop the resist and etch the sample with ICP RIE. We remove the resist leftover and deposit 1.2 μm of PECVD TEOS SiO_2 as top cladding. All the fabrication steps after the wet oxidation process are performed in temperatures not exceeding 350 degrees, making PECVD SiN compatible with Back End of Line CMOS processes. The details of the fabrication steps are shown in Fig. 5.5 while an optical image with SEM details of the photonic chip are reported in Fig. 5.6(a)-(c).

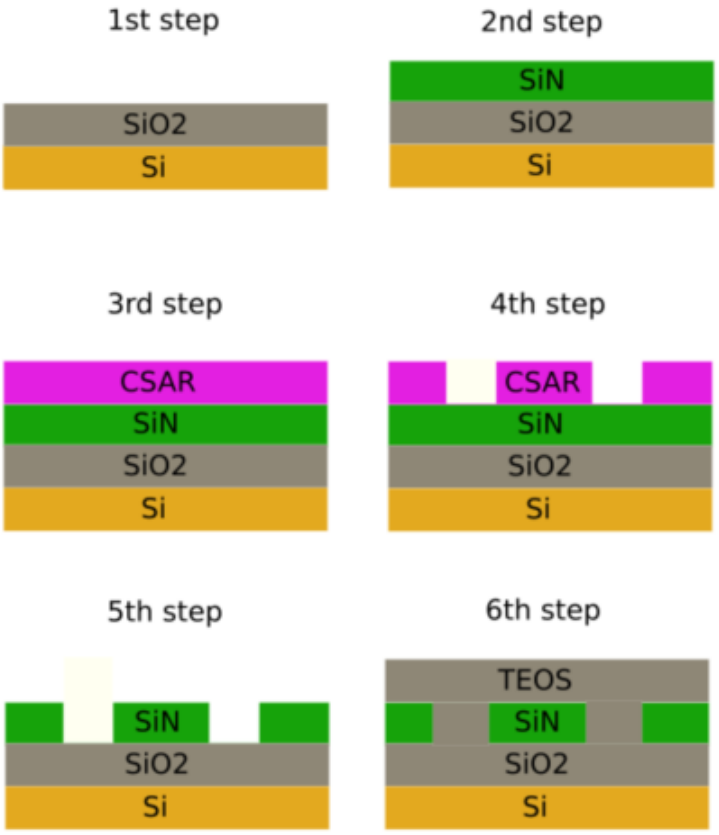

Figure 5.5: Process steps regarding the fabrication of the photonic device.

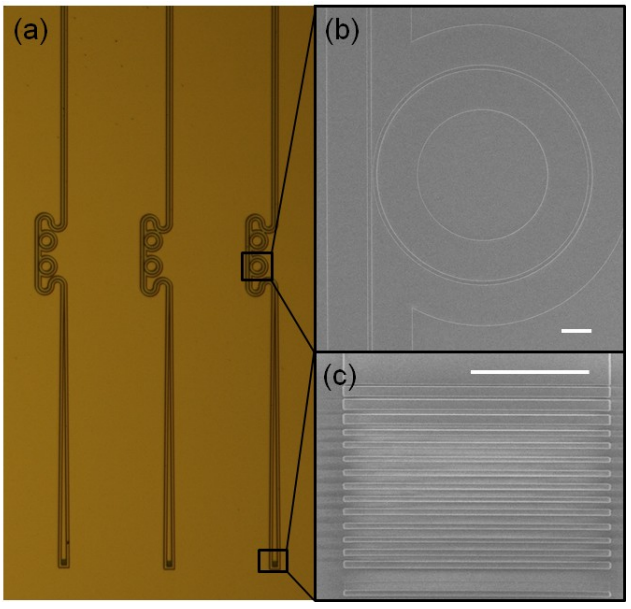

Figure 5.6: (a) Fabricated photonic device with a detailed SEM picture of the (b) ring and (c) grating coupler. Two rings are present due to lack of tunability of the DBF laser and sharp bends tend to be used as single mode filters.

We do an optical characterization of the devices by performing transmission measurements shown in Fig. 5.7 that displays the resonance spectrum of a critically coupled ring with 19 μm radius with an intrinsic Q-factor of 320,000. From this value we can extract the propagation losses of the structure to be 2.2 dB/cm.

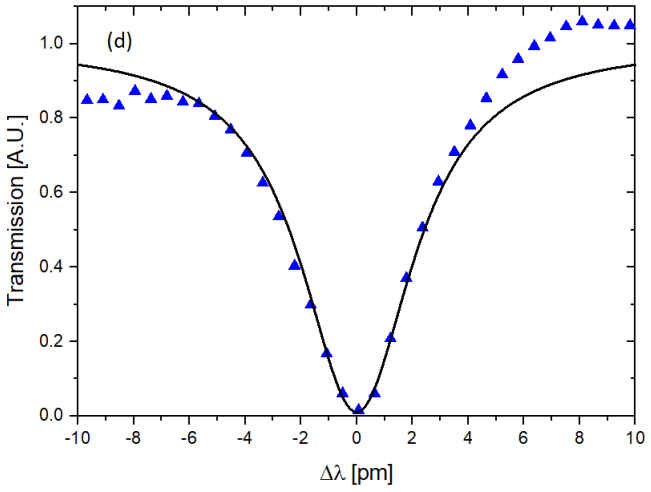

Figure 5.7: Transmission spectrum of a ring resonator with an intrinsic Q-factor of 320k at 785 nm. Data are well fitted with Lorentzian function.

5.2.2 Experimental setup and performance characterisation of the single photons

We design an experimental setup to measure SFWM that consists of three parts (Fig. 5.8). The first part in Fig. 5.8(a) is composed by spectral filtering to reduce the laser sideband noise to the level of the single photons. This we achieve with one dispersive grating whose stray light reduction is 60 dB at frequencies of signal (777.5 nm) and idler (792.5 nm). The filtered beam is then coupled via a high NA objective to the 2 mm long input waveguide, shown in Fig. 5.8(b). We use free space coupling for the input to avoid any spurious light generated in optical fibers. The pump laser propagates in the waveguide and couples to the ring resonator under test where it was further attenuated by 23 dB due to the destructive interference of the resonator, and simultaneously the twin photons are generated. Signal, pump and idler photons are then coupled to a fiber array thanks to the grating coupler. The last part of the setup, Fig. 5.8(c), is used to separate the signal and idler photons and reject the pump light. In order to separate the correlated photons we use another dispersive grating in Littrow configuration where the pump wavelength is back reflected while the signal and idler are diffracted to opposite angles with 80% efficiency . Additional rejection was provided by 3 nm bandwidth filters centred at respective signal/idler wavelength. The single photons are finally coupled to single mode fibers and are detected by silicon avalanche photodiode detectors with quantum efficiency of 65%. The electric signals are recorded by counting electronics and

a time interval analyser to measure single and coincidence counts.

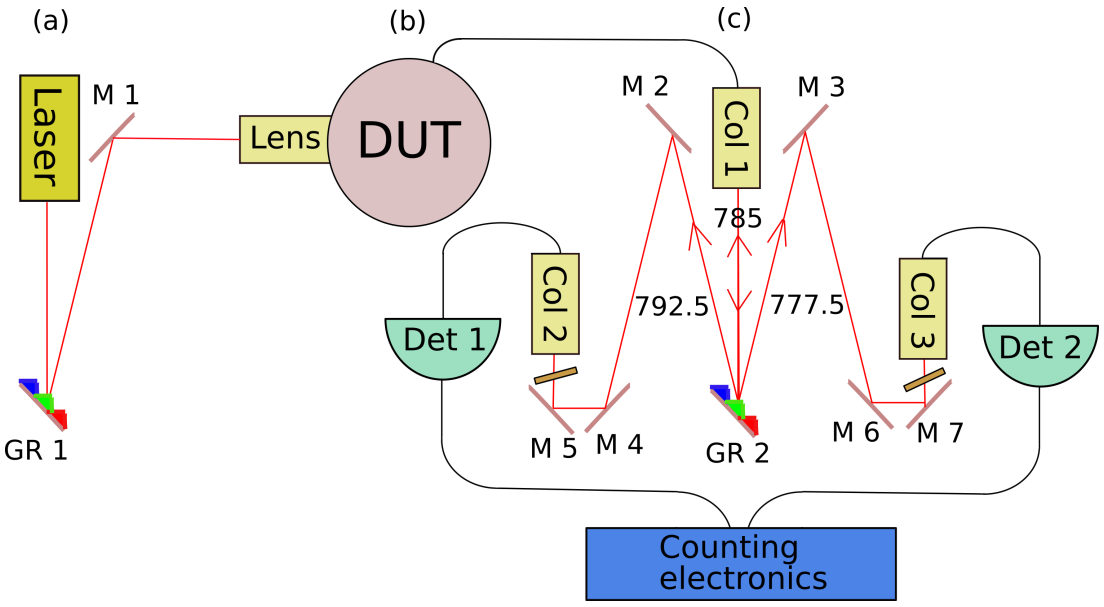

Figure 5.8: Schematic setup for on-chip generation and measurement of single photons. (a) Spectral filter of the noise generated from the pump laser. (b) Coupling to the SiN chip and generation of signal and idler photons. (c) Free-space optics to separate the generated photons and remove the pump stray light. GR, diffraction grating; M, mirror; Col, collimation optics; DUT, device under test.

From the coincidence measurement we are able to extract the information about single photons generation in the ring coupled to the waveguide. The experimental data of generated pairs are extracted from the equation

$$G_{SFWM} = \frac{P^{SFWM}}{2\hbar\omega_p} = \frac{CC}{10^{-(\eta_s+\eta_i)/10}}, \tag{5.16}$$

where CC are measured coincidences, $\eta_{s/i}$ are the overall collection losses for the signal and idler, which in our case are 16.4 dB and 24.1 dB, respectively. P^{SFWM} is the power of measured photons based on the Eq. 5.15

$$P^{SFWM} = (\gamma L)^2 \left(\frac{Q_l v_p}{\omega_p L/2}\right)^3 \frac{\hbar\omega_p v_p}{2L} P_p^2, \tag{5.17}$$

where γ is the nonlinear parameter, L is the circumference of the ring, P_p is power of the pump in the ring, Q_l is the measured loaded Q factor. The nonlinear parameter is defined as $\gamma = \frac{2\pi n_{nl}}{\lambda_p A_{eff}}$, where we used the nonlinear index n_{nl} from literature [122] and the mode effective area A_{eff} and group velocity v_p of the fundamental mode were numerically calculated. We can conclude that the experimental data in Fig. 5.9 are in a good agreement with the theoretical model of Eq. 5.17. This confirms the nonlinear

relationship between the generated single photons and pump photons with a generation rate of 950,000 $\frac{pairs}{mW}$.

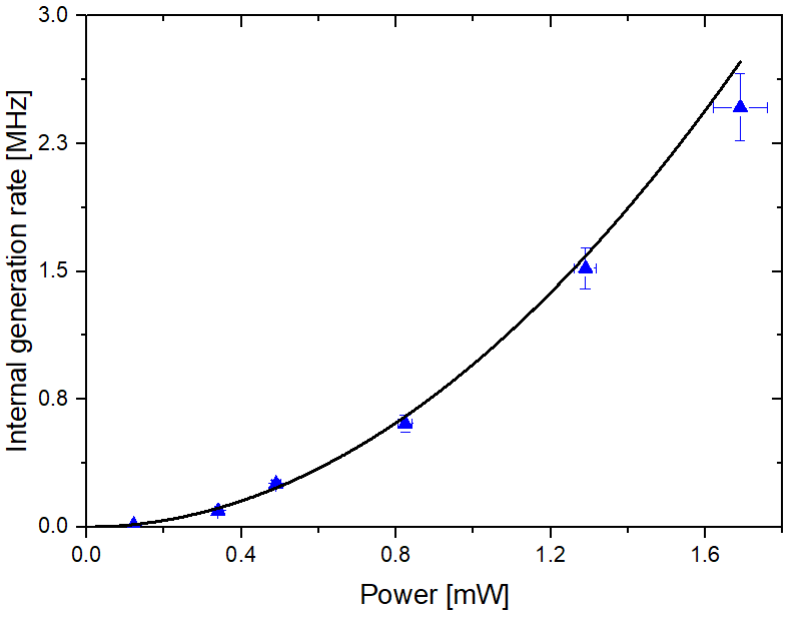

Figure 5.9: Measured (triangles) and theoretical (solid line) generation of inferred photon pairs at the ring location as a function of the power coupled into the chip, measured with 1152ps time integration.

Beside the photon pair generation rate, an important figure of merit to characterize the quality of a correlated photon pair source is the coincidence CC to accidental AC ratio CAR. It takes into account the relationship between the number of SFWM photon pairs and the number of accidental coincidences, coming from photons emitted randomly in time

$$CAR = \frac{CC}{AC}, \tag{5.18}$$

$$CC = G_{SFWM}\eta_s\eta_i, \tag{5.19}$$

$$AC = R_sR_i\delta t, \tag{5.20}$$

$$R_s = (n_s + G_{SFWM})\,\eta_s + dc_s, \tag{5.21}$$

$$R_i = (n_i + G_{SFWM})\,\eta_i + dc_i, \tag{5.22}$$

where CAR depends on the integration time δt and dark counts of the detectors $dc_{s/i}$, and any linear noise $n_{s/i}$ resulting from the light interaction in the material. $R_{s/i}$ are the measured singles at signal and idler frequency, respectively. In Fig. 5.10(a) we report the power dependence of the detected signal photons R_s, showing a linear dependence. This relation suggests that the ring resonator emits uncorrelated photons generated from spontaneous Raman scattering, as suggested by the broad scattering spectrum of SiN

[123]. In Fig. 5.10(b) we characterize CAR as a function of the power in the waveguide. The number of coincidences and accidental counts is measured with a time window of 1152 ps, longer than the FWHM value of the coincidence peak of $\sim 500ps$. This is to ensure that all the coincidence counts are included, at the expense of a lower CAR [74]. Moreover, the FWHM value is mainly dictated by the jitter of our Si detectors, rather than the lifetime of the photons ($< 200ps$, considering the Q factor of our cavity). Faster detectors, or pulsed excitation, would result in a higher measured CAR. Fig. 5.10(a) also includes a curve from equations 5.18-5.22 where the parameters are extracted from Fig. 5.9, considering correction of signal and idler photons by respective phonon distribution [124], without fitting any additional variable. The model shows good agreement with data, indicating that the CAR value is limited from Raman photons at all the powers used in the experiment. Effects from detector dark counts are only visible at very low pump powers, while multi-photon events cause a small decrease in CAR for increasing power in the tested range. These results are comparable to CAR measurements in strip SiN waveguides [125] and Hydex rings resonators [126] at telecom wavelengths, once the detection timing is considered.

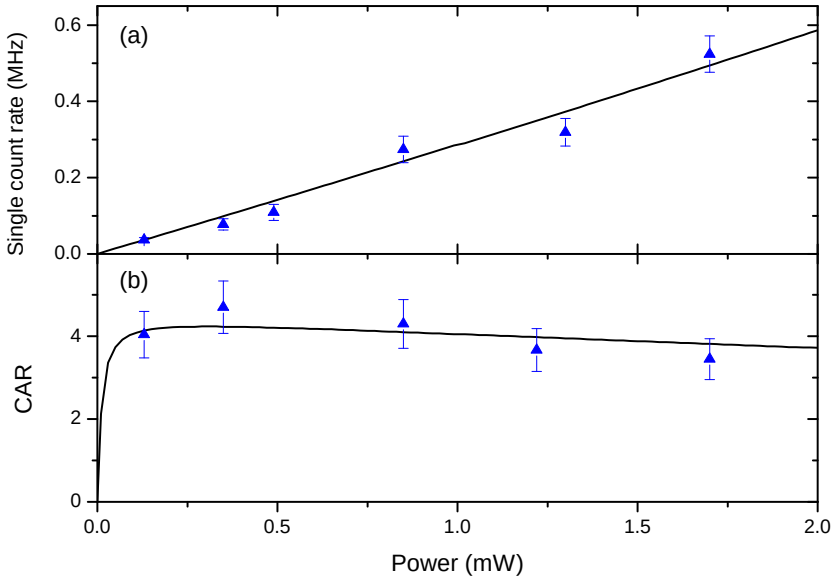

Figure 5.10: (a) Measured (dots) and theoretical (solid line) power dependence of the single photon generation at the signal wavelength (777.5nm) fitted by linear function. (b) Measured Coincidence to Accidental Ratio (CAR).

5.2.3 Raman noise reduction in lossy ring resonator

As we show in the previous section, CAR is mainly limited by the generation of spontaneous raman scattering. Here, we further investigate whether we can reduce spurious noisy effects in the ring by optimizing some of its parameters, such as losses and coupling

condition. For that reason we fabricate a new sample. We make a linear characterisation of the photonic chip to obtain results for three different rings with distinct features as shown in Fig. 5.12. Two of the resonators posses the same propagation loss of 1.4 dB/cm where one of them is in critical coupling conditions (Fig. 5.12 (a)) while the other is in slightly undercoupled regime (Fig. 5.12 (b)). The last ring is a bit overcoupled but the total loss of the ring is 2.1 dB/cm (Fig. 5.12(c)). As it can be seen from Eq. 5.18-5.22, since the detection rate of either Raman or single photons is highly above the dark counts of the detectors, the performance of the source can be evaluated independently of the its outcoupling efficiency. For that reason we can measure the CAR of individual rings and compare their signal to noise ratio. The results are shown in Fig. 5.11.

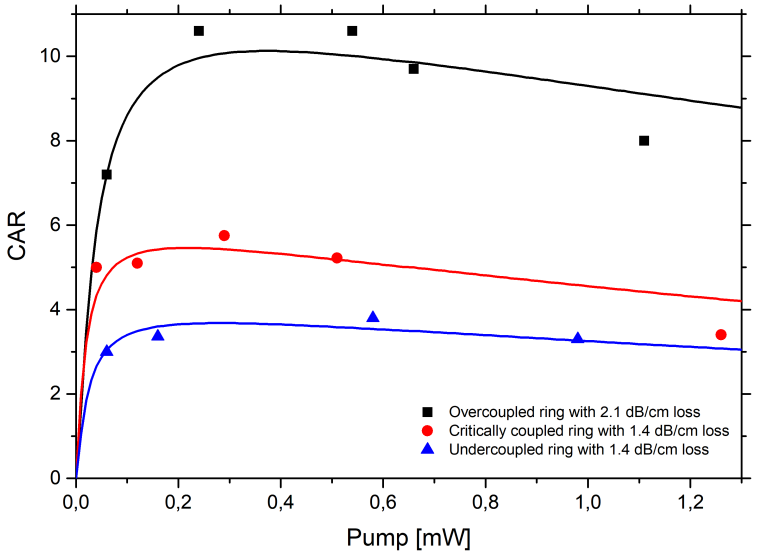

Figure 5.11: Performance characterisation of single photon generation in three different ring resonators with different coupling conditions.

Unexpectedly, more than two times improvement in performance is obtained in case of a ring with the worst Q-factor. At the same time the two rings with the same propagation losses exhibit a slightly different CAR, where the undercoupled condition exhibits smaller signal to noise ratio. We strongly suspect that the reason for such behaviour is the fact that decreasing the coherence time, by either decreasing the losses or increasing the coupling condition, makes the spontaneous raman photons more uncorrelated while single photons do not change their correlation properties. For that reason it might be interesting investigate additional steps to optimize the CAR and generation rate as function of propagation or coupling losses. Another possible way to decrease the generation of raman photons is performing the experiment in 77 K.

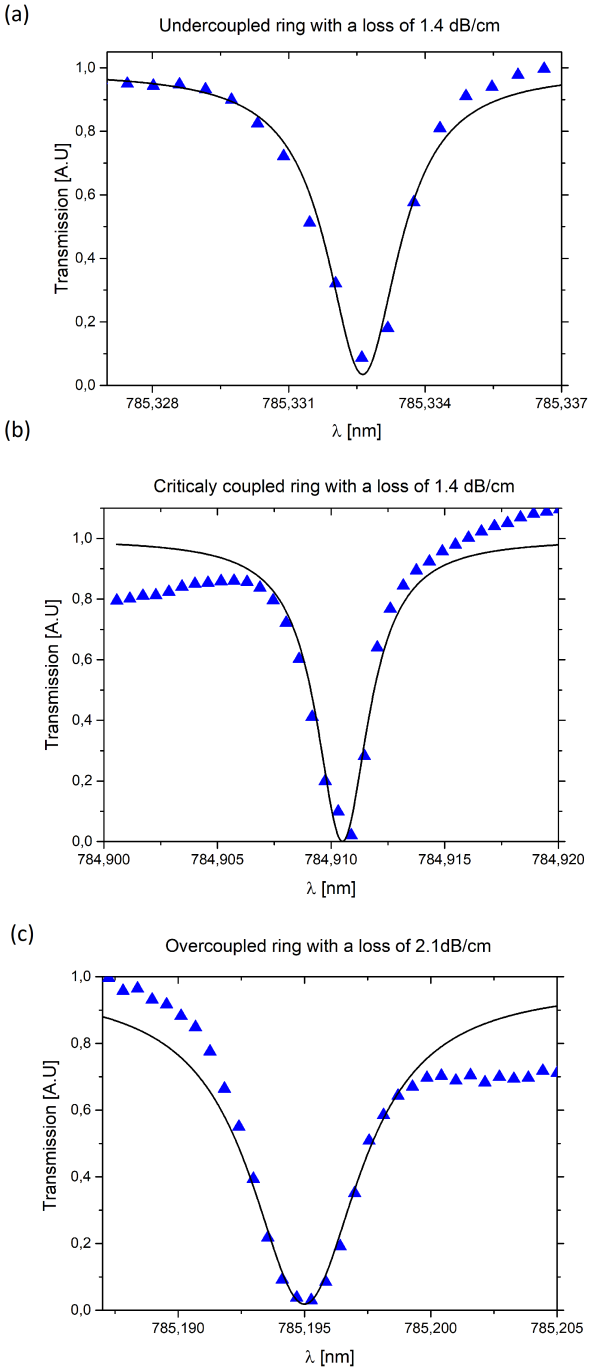

Figure 5.12: Linear characterisation of (a) Undercoupled ring resonator with 1.4 dB/cm losses, (b) Critically coupled ring resonator with 1.4 dB/cm losses and (c) Overcoupled ring resonator with 2.1 dB/cm losses.

5.2.4 SPAD characterisation on a photonic chip

In this section we briefly introduce integrated silicon single photon avalanche detectors (SPAD) working at room temperature and show recent fabrication results that will lead to the future characterisation of SPADs with attenuated light.
The high measurement efficiency, low time jitter, high uniformity across a wafer scale distribution and room temperature accessibility makes SPADs an excellent candidate for efficient, fast time correlated detection of single photons integrated on a chip [66]. Samples with already integrated complex electronics can be obtain from a commercial CMOS facility. For that reason we collaborate with Prof. Alberto Tosi and his group from Politecnico of Milan to design and fabricated SPAD chips with cross section shown in Fig. 5.13.

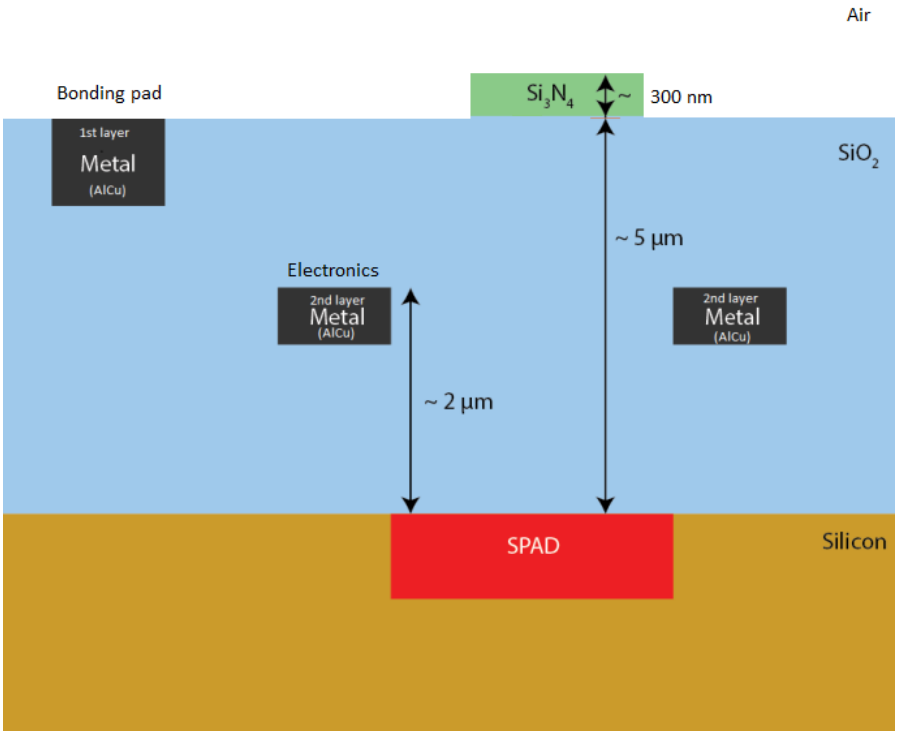

Figure 5.13: Cross section of the SPAD chip containing electronics to convert optical to electronic signals. On top is already shown the fabrication of a waveguide in our nanofabrication facility.

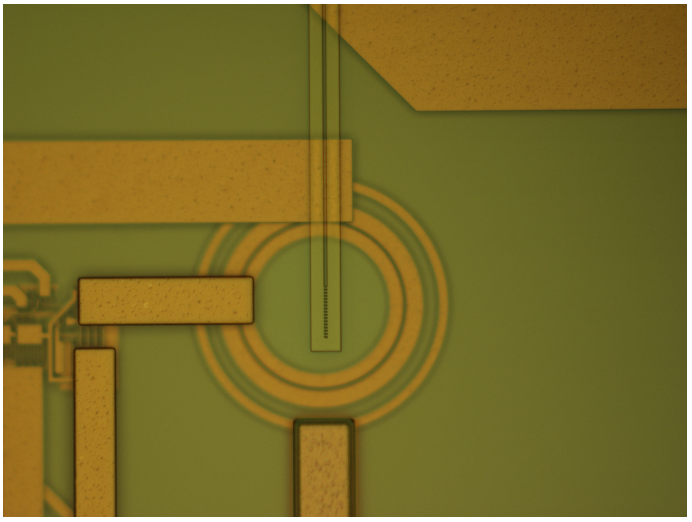

Figure 5.14: Optical image of a waveguide with grating coupler that diffracts light at visible wavelength with 50% efficiency.

The first layer contains the doped part of silicon to form the SPAD detectors. On top of them is the first metal layer containing the complex electronics to convert the measured optical signal to a electronic TTL pulse. Unfortunately, additional signal amplification is needed for successful read out. For that reason the second layer of metal is present to bond the chip to external PCB board with integrated amplifier so that we can directly count the signals for either single or two photon coincidence measurements with a PicoQuant counting card. The last layer contains Silicon Nitride deposited by the CMOS foundry. Since the sample needs further planarization in order for us to be able to deposit SiN developed in our facility we first decided to characterise the SPAD with SiN already present on the chip. We thin down the sample to 300 nm thickness in order to obtain high incoupling efficiency to the chip and high diffraction efficiency from the grating to the SPAD detector shown in Fig 5.15 (b). We also fabricate several ring resonators to evaluate the propagation loss of the commercial SiN at 785 nm from a waveguide structure shown in Fig. 5.16. As it can be seen the losses are very high for any further application of the SiN that was deposited by the CMOS facility. Therefore, for future devices its crucial to further planarize the surface with a spin on glass and then deposit low loss SiN that was developed in the Southampton nanofabrication center. At the moment the sample is at the group of Prof. Tosi who designs the PCB board. We hope to obtain and characterise the chip it soon.

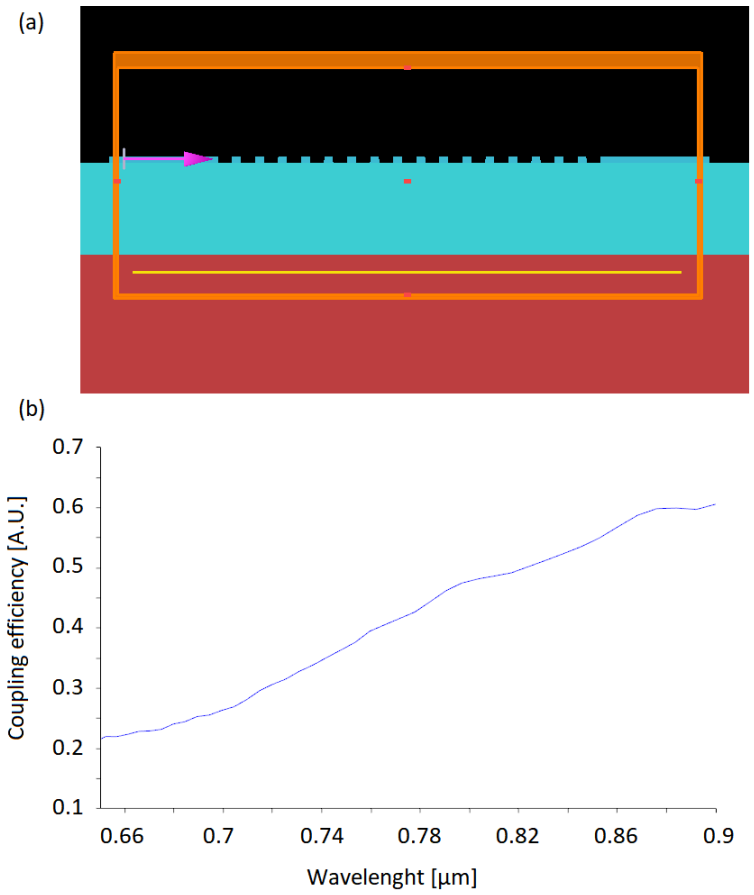

Figure 5.15: (a) Simulation window of diffraction grating to couple light from waveguide to the SPAD with calculated coupling efficiency shown in (b).

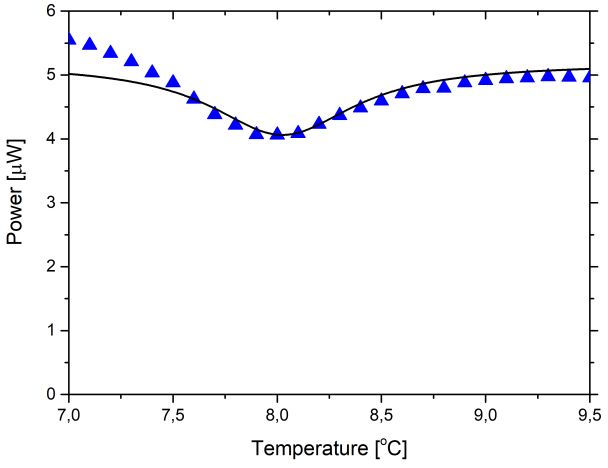

Figure 5.16: Resonance spectrum of a highly undercoupled ring resonator integrated on a SPAD chip with evaluated losses of 41 dB/cm.

5.3 Future work: Fully integrated on chip analogue quantum simulator working at room temperature

As it was introduced in Chapter 1, continuous time analogue quantum simulator based on quantum walk algorithm can be easily implemented in optical circuits via coupled waveguide arrays. In the part of this chapter we combine all the results from previous sections and propose a design for fully integrated photonic quantum simulator working at room temperature shown in Fig. 5.17. Due to low detections efficiencies of the integrated SPAD detectors and lack of low loss fast switches to implement efficient spatial multiplexing, the simulator contains only three pair-photon sources in order to herald a three photon state with a reasonable generation rate. In order to uncorrelate the generated spontaneous Raman scattering, we can fabricate ring resonators in overcoupled regime and work under pulsed excitation. Since SiN is not limited by two photon absorption, we can pump the sources with high enough power to saturate the correlated pair generation before we start producing multiphoton events. Combining all this elements, we should easily achieve a CAR of more than 10 in order to obtain high enough single photon indistinguishability for an efficient implementation of the quantum walk algorithm.

We imagine the design work in a following way: We start pumping the three thermally tuned rings that produce pair of photons, where one of them is later used to herald the presence of the other. The pump, signal and idler photons continue to propagate in their respective waveguides until they have to pass a distributed bragg grating that is used to filter out the pump of more than a 100 dB [58]. The signal and idler further propagate until they are multiplexed to another waveguide with a ring resonator thermally tuned to the respective frequency of either signal or idler. The presence of a three photons in the waveguides that serve as input state for the quantum walk are then heralded by a three photon coincidence measurement performed by the integrated SPAD detectors. Afterwards, the three photon state propagates through a carefully designed set of waveguide arrays. At the end the photons are separated by adiabatic fanout structure and measured by set of SPAD detectors whos number corresponds to the number of coupled waveguides of the simulator. The coincidence electronics to convert optical to electronic signal is already integrated on the chip so the readout of the correlated statistics can be performed by additional PCB board and a computer.

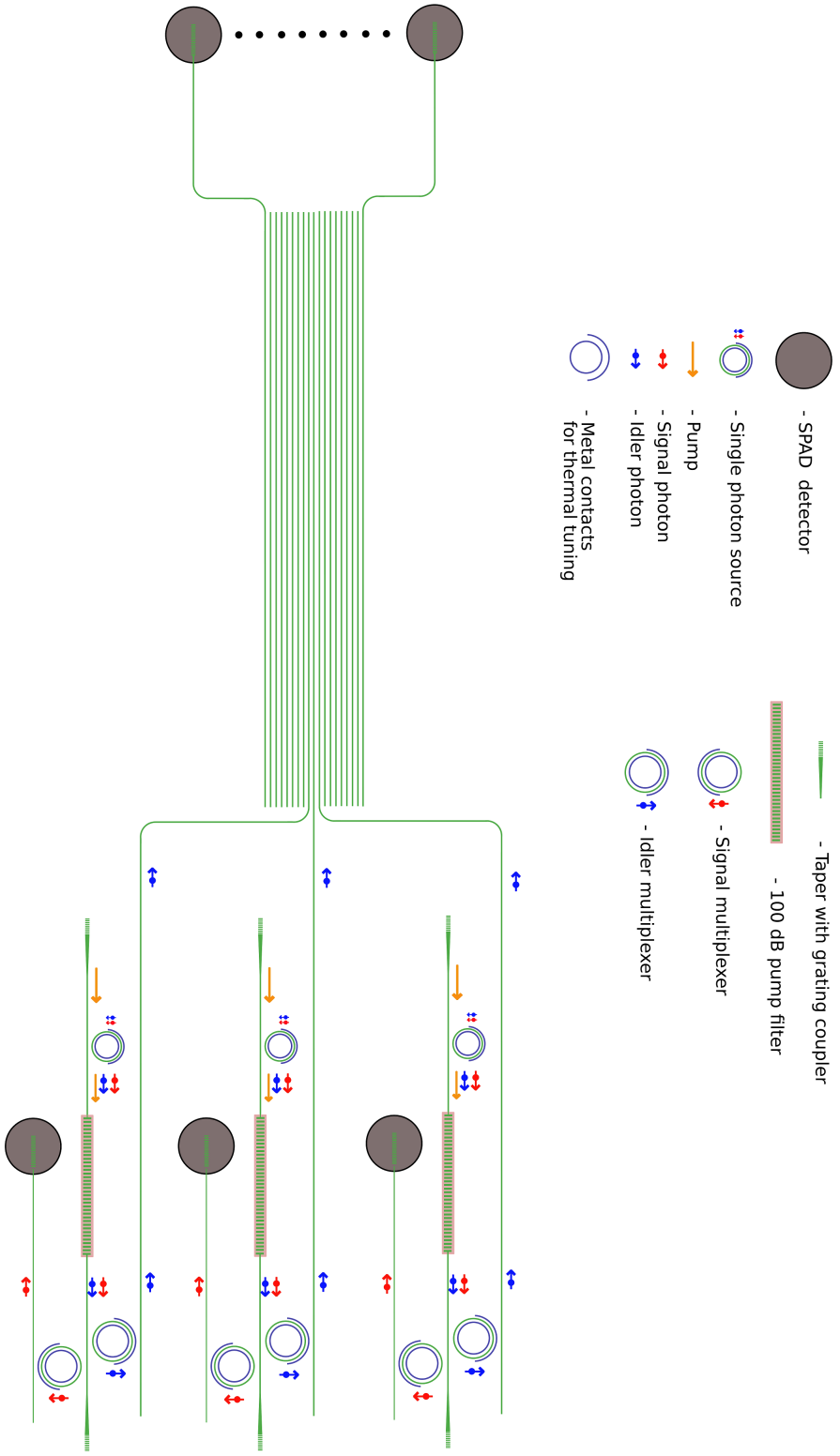

Figure 5.17: Schematic design of a fully integrated analogue quantum simulator working at room temperature.

5.4 Conclusion

In conclusion, we studied spontaneous four wave mixing process in the near visible region generated in a microring resonator. Contrary to alternative sources based on periodically pooled crystals the CMOS compatible fabrication process developed here makes possible the integration of non-classical sources together with silicon based detectors working at room temperature. We believe that the measured CAR is mainly limited by the linear noise coming from uncorrelated Raman photons which affects amorphous materials, including Silicon Nitride. Optimization of the optical properties of SiN through tailored material deposition, combined with the design parameters for the ring resonator, can lead to an increase of generation rate and CAR value. At the expense of lower CAR, an increase of Q factor will also reduce the bandwidth of the generated photons from the current $\sim 2.4GHz$ to sub-GHz values, making this source fully compatible with atomic memories. Finally, the confirmed absence of saturation in the pair generation rate, thanks to the high band gap of SiN, suggests that integrated single photon sources can be developed well in the visible spectrum. These properties make SiN resonators excellent candidates to expand the applications of integrated single photon sources for a broad range of quantum technology applications such as analogue quantum simulators discussed in this chapter.

Chapter 6

Integrated Source Of Broadband Squeezed States Of Light

Even thought the results presented in previous chapter show some promise regarding fabrication of small scale quantum simulator, scaling up the photonics technology based on purely discrete variable (DV) encoding of single photons is quite challenging technological task. The obstacles are present in both, the nanofabrication requirements and the models for UQC itself. The fact that logical operations, losses and error correction place a polynomial overhead on the amount of nonclassical sources to achieve near unit computational determinism, makes DV encoding hard to scale. For that reason, we decide to move towards continuous variable (CV) encoding of squeezed state of light [127]. Unfortunately, CV model lacks the high fidelity operations of DV and there is yet not efficient error correction scheme for fault tolerant UQC (FTUQC). Therefore, in the beginning of this chapter we introduce a hybrid DV-CV approach to build a deterministic fault tolerant UQC (FTUQC) that harness the advantage of high fidelity, error correction friendly operations of DVs and unconditional control and detection of CVs [128], [129]. Next, we briefly explain what is squeezing, how to measure and generate it via self phase modulation in a ring resonator cavity. At the end we show our recent results and future prospects of hybrid encoding on a photonic chip.

6.1 CV model for measurement based fault tolerant UQC

In 1999, Lloyd and Braunstein provided sufficient conditions for building a UQC over continuous variables that could be constructed using linear optics, squeezers and Kerr effect based nonlinear devices [47]. This work has been extended by Menicucci to CV measurement based universal quantum computation model (CV-MBUQC) [130], which has been first proposed for DV [131]. As opposed to DV, CV-MBUQC is purely unconditional due to the analog nature of the CV gaussian states. The beauty of this

model is that deterministic entangling gates and can be produced by beam-splitter and homodyne detector which are easily applicable by modern experimental means [132]. Unfortunately, the low fidelity of CV operations limits the ability to apply standart error correcting protocols to achieve fault tolerancy. Therefore a popular approach is to hybridize the CV and DV systems. First model was proposed by Gottesman, Kitaev and Preskill (GKP) [133]. In the heart of the proposal is the possibility to encode finite-dimensional quantum system (qudit) into an infinite-dimensional system (CV envelope). In its realistic requirements, the authors describe the GKP qubit as a superposition of squeezed Gaussian states in a phase space that are weighted by a Gaussian envelope. Such a hybridized qubit is well protected against small errors and that a universal set of Clifford and Non-Clifford operations can be efficiently applied on a GKP qubit to realize a FTUQC [133]. Furthermore, it has been calculated that 20.5 dB of squeezing is required to perform FTUQC with CV-MBUQC where the nodes of the 2D square lattice cluster state are composed out of squeezed vacuum, GKP qubits and cubic phase states (or Hadamar eigenstates to implement non-Clifford operations). [134]. Recently, such a 2D Gaussian cluster state composed out of 25 000 temporal modes has been prepared using only four sources of quadrature squeezed states of light and two delay lines providing a true scalable platform for quantum computation [135]. Later, using postselection and analog surface error correction code, a threshold value of 9.8 dB on a 3D cluste state has been evaluated [50].

Recently, a realization of a GKP qubit with 7.3 dB of squeezing has been produced in trapped ion system [136] showing a truly exciting promise of the hybrid architecture. Even though there are several other experimental proposals how such a logical qubit can be prepared, we mainly focus on all optical implementation [137], [138] based on photon substraction or addition that can conditionally prepare GKP qubits with sufficient amount of squeezing. Since theses states are fragile to losses and detector inefficiencies, the only approach that can prepare near-deterministic, good coherent superpositions are in integrated low loss waveguides, such as SiN, where near unit efficiency photon number resolving SSPDs and germanium homodyne detectors [139], have already been fabricated. Once a good GKP qubit is prepared, similar experimental methodology concerning preparation of cubic phase state, to implement non-Clifford operation, can be applied [140]. Alternatively, if we use GKP error correction, it is possible to generate distillable magic states for non-Gaussian operations only using GKP qubits, Gaussian operations and heterodyne measurements [141]. This method is extremely powerful because it removes the impractical requirement to implement nonlinear electronic feed-forward for non-Gaussian gates. The only condition is to prepare GKP qubits with sufficient purity [142] and high enough squeezing.

The real beauty of the GKP proposal is that once you prepare a good GKP qubit it is not just a physical but a logical qubit in the computational system. This is a big advantage of opposed traditional DV systems with ions, superconducting circuits or single photons where a single logical qubit is composed of hundreds or even thousands physical

qubits for efficient error correction protocol. The CV-MBUQC architectures proposed so far are based on time-domain multiplexing scheme [143], [144] which is highly relaxed on the number of physical resources needed [135]. In an ideal world we would only need one high quality source of GKP states, diminishing the chances of fabrication imperfections that plagues technologies based on encoding information into physical qubits. Such a platform that can be scaled up on a single wafer which shows an exponential improvement in comparison to other architectures where football size stadiums quantum computers, cooled to low temperatures are in consideration. Furthermore, the photonic platform can be expanded to work at room temperature which makes this platform even more attractive.

6.2 Quantum theory of quantized electromagnetic field

Position and momentum operators of a classical harmonic oscillator are formally the same as the quadrature operators of a quantized electromagnetic field. Since the operators do not commute, they have to obey the Heisenberg uncertainty relation which gives rise to non-zero energies of quantum mechanical vacuum oscillation - vacuum noise.

6.2.1 Quadrature operators

The Hamiltonian of a quantized harmonic oscillator in terms of annihilation and creation operators can be written as

$$\hat{H}_k = \hbar\omega_k \left(\hat{a_k}^\dagger \hat{a_k} + \frac{1}{2} \right), \tag{6.1}$$

where $\hbar$ is the reduced planck constant, $\hat{a_k}^\dagger$ is the creation operator, $\hat{a_k}$ is the annihilation operator, ω is the eigenfrequency of the oscillator and k is the number of mode of the electromagnetic field. The Hamiltonian can be rewritten in the operators of position and momentum as

$$\hat{H}_k = \hbar\omega_k \left(\hat{x_k}^2 + \hat{p_k}^2 \right), \tag{6.2}$$

where the position operator is defined as

$$\hat{x_k} = \frac{\left(\hat{a_k} + \hat{a_k}^\dagger \right)}{2} \tag{6.3}$$

and momentum operator as

$$\hat{p_k} = \frac{\left(\hat{a_k} - \hat{a_k}^\dagger \right)}{2i}. \tag{6.4}$$

Since these operators obey the commutation relation

$$\left[\hat{x_k}, \hat{p_{k'}} \right] = \frac{i\delta_{kk'}}{2}, \tag{6.5}$$

their variances have to follow the Heisenberg uncertainty relation

$$\left\langle (\Delta \hat{x_k})^2 \right\rangle \left\langle (\Delta \hat{p_k})^2 \right\rangle \geq \frac{|\langle [\hat{x_k}, \hat{p_k}] \rangle|^2}{4} = \frac{1}{16}. \tag{6.6}$$

The product of the position and momentum variances are bounded by the Heisenberg principle to be 1/16 meaning that each variance has value of 1/4, which we will refer to as the standard quantum limit (SQL), vacuum noise or shot noise. In reality a single variance, for example the position, can have smaller value than 1/4 and beat the SQL while at the same time the variance of the momentum increases, satisfying the Heisenberg uncertainty relation.

6.2.2 Squeezed states

We define squeezed state in case $\left\langle (\Delta \hat{x_k})^2 \right\rangle \neq \left\langle (\Delta \hat{p_k})^2 \right\rangle$ and at the same time the variance of one observable drops ("squeeze") below the SQL while the variance of the conjugate observable increases ("anti-squeeze") above the SQL. Single-mode squeezed states are generated when the vacuum noise of either of the two conjugated operators are squeezed by the unitary squeezing operator

$$\hat{S}(\zeta) = e^{\frac{1}{2}\left(\zeta^* \hat{a}^2 - \zeta \hat{a}^{\dagger 2}\right)}, \tag{6.7}$$

where $\zeta = re^{i\theta}$. The amplitude r is the squeezing parameter and θ is the phase of the squeezed state.
When we apply the squeezing operator on creation and annihilation operators we get

$$\hat{S}^\dagger(\zeta)\, \hat{a} \hat{S}(\zeta) = \hat{a} \cosh r + \hat{a}^\dagger e^{i\theta} \sinh r, \tag{6.8}$$

$$\hat{S}^\dagger(\zeta)\, \hat{a}^\dagger \hat{S}(\zeta) = \hat{a}^\dagger \cosh r + \hat{a} e^{-i\theta} \sinh r. \tag{6.9}$$

We can define the rotated quadrature operators of position and momentum as

$$\hat{x}^{(\theta)} = \frac{\left(\hat{a} e^{-i\theta} + \hat{a}^\dagger e^{i\theta}\right)}{2}, \tag{6.10}$$

$$\hat{p}^{(\theta)} = \frac{\left(\hat{a} e^{-i\theta} - \hat{a}^\dagger e^{i\theta}\right)}{2i}. \tag{6.11}$$

Because the momentum operator in rotated frame is defined as $\hat{p}^{(\theta)} = \hat{x}^{(\theta)+\pi/2}$ we can define the full continuum of quadratures only with position operator $\hat{x}^{(\theta)}$.
By applying the squeezing operator to the rotated mode and setting the $\theta = 0$ the position and momentum operator can be defined with the squeezing parameter r as

$$\hat{x}(r) = e^r \hat{x}^{(0)}, \tag{6.12}$$

and

$$\hat{p}(r) = e^{-r} \hat{p}^{(0)}, \tag{6.13}$$

which results in squeezed momentum operator and antisqueezed position operator determined by r. In Fig. 6.1 we show several cases of squeezed states visualized in the phase space representation.

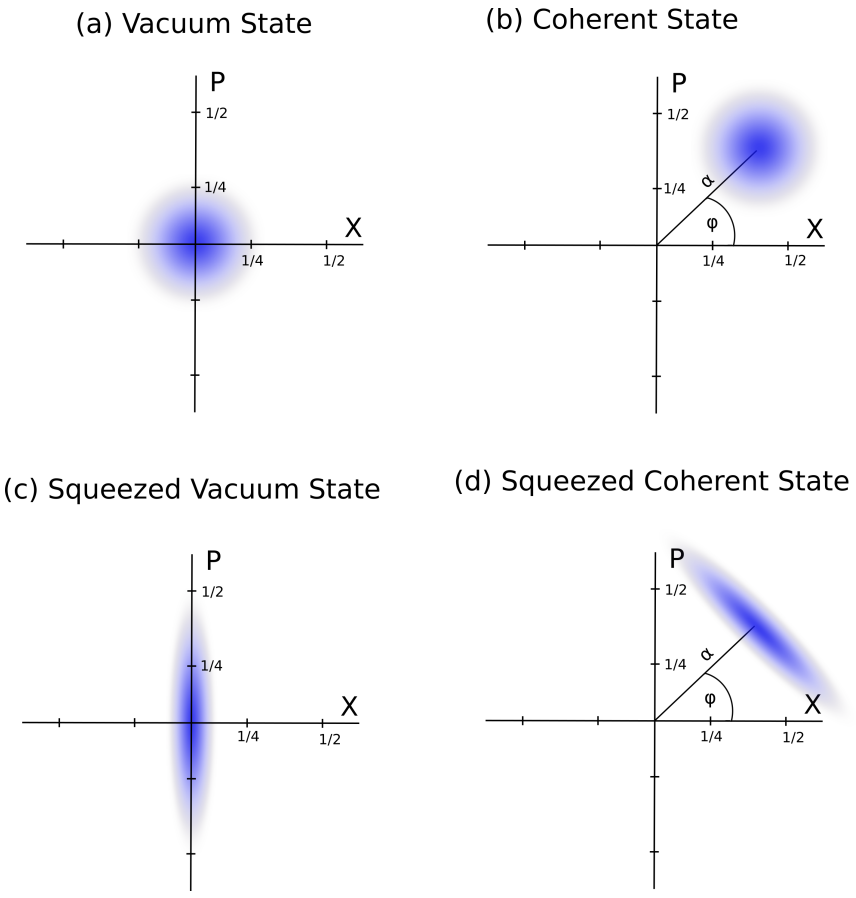

Figure 6.1: Visualization of (a) vacuum state, (b) coherent state, (c) squeezed vacuum and (d) squeezed coherent state in the phase space representation. Cases (a) and (c) are discussed in the main text regarding the variance of vacuum state being limited by the Heisenberg uncertainty principle for the vacuum state while the squeezed vacuum has one squeezed and one antisqueezed variances. Coherent state (b) is a displaced vacuum while squeezed coherent state is a displaced squeezed vacuum in the phase space.

6.2.3 Squeezing via self phase modulation

Historicaly, the first observed squeezed state was experimentaly realized by Slusher [145] in his groundbreaking experiment regarding FWM in an atomic vapor of sodium atoms. Afterwards, many other technological proposals such as laser diodes [146] and second order nonlinear effects [147] became to produce significant shot noise reduction. A very common way to generate squeezed states of light in a Kerr medium is through the χ_3

nonlinear optical effect [148]. As mentioned in previous chapter, FWM involves the conversion of two pump photon, at an angular frequency of ω_p, to a generation of pair of entangled photons at signal ω_s and idler ω_i frequency, satisfying the energy and phase conservation criterion. Self phase modulation is always present and has the strongest effect on the pump photons due to constantly fulfilled phase matching condition. Under large optical field the refractive index starts to be substantially dependent on its intensity I resulting to

$$n(I) = n_0 + n_{nl}I, \tag{6.14}$$

where n_0 is the linear and n_{nl} is the nonlinear refractive index. In this case the overall phase ϕ_{tot} of the the pump field starts to be disturbed by additional nonlinear phase shift ϕ_{nl} resulting in

$$\phi_{tot} = \phi_l + \phi_{nl}, \tag{6.15}$$

$$\phi_{nl} = \frac{2\pi n_{nl} I L}{\lambda} \tag{6.16}$$

where ϕ_l is the initial phase of the coherent state and ϕ_{nl} is the self-induced nonlinear phase shift. SPM squeezing has a intuitive interpretation for an input pump beam

$$\alpha = \alpha_0 + \delta X_1^{in} + \delta X_2^{in} \tag{6.17}$$

that consists of an coherent amplitude α_0 and quadratures for the amplitude δX_1^{in}, and phase δX_2^{in} operators. The SPM is driven by both the amplitude and the vacuum noise that defines the acquired variance of the nonlinear phase shift at the sideband frequencies

$$\delta\phi_{nl} = \frac{4\pi n_{nl} L \alpha_0 \delta X_1^{in}}{\lambda}. \tag{6.18}$$

Therefore, any small deviation of phase fluctuations $\Delta(\delta X_2) \approx \alpha_0 \delta\phi_{nl} \approx 2r\delta X_1^{in}$corresponds to following input-output relations

$$\delta X_1^{out} = \delta X_1^{in}, \tag{6.19}$$

$$\delta X_2^{out} = \delta X_2^{in} + 2r\delta X_1^{in}, \tag{6.20}$$

from those we can see that the amplitude quadrature is unaffected, while the phase variance has a dependence on the squeezing parameter r. Usually the χ_3 effect is quite limited due to the small n_{nl} which results in modest levels of squeezing. Therefore, in order to enhance the light matter interaction we describe the continuous wave (CW) light matter interaction in ring resonator Kerr media which was developed in [149].

6.2.4 Quantum dynamics of light-matter interactions in a ring resonator based χ_3 medium

The self phase modulation part of the interaction Hamiltonian is derived as

$$\hat{H}_{SPM} = \frac{1}{2}\hbar\zeta \hat{a_p}^{\dagger 2}\hat{a_p}^2, \tag{6.21}$$

and it is govern with an interaction strength

$$\zeta = \frac{\hbar\omega_p c^2 \gamma}{2n_{eff}^2 L}, \tag{6.22}$$

where n_{eff} is the effective index of the fundamental mode in the ring resonator and γ is the nonlinear parameter defined in Sec. 5. In order to understand the dynamics of the light matter interaction enhanced in a ring resonator the Hamiltonian from Eq. 6.21 is solved via Langevin equation of motion

$$\frac{d\hat{a_p}}{dt} = -\frac{i}{\hbar}\left[\hat{a_p}, \hat{H}\right] - \kappa\hat{a_p} + \sqrt{2\kappa_c}\hat{a}_{p,in}e^{-i\omega_L t} + \sqrt{2\kappa_0}\hat{b_p}, \tag{6.23}$$

$$\hat{H} = \hbar\omega_p\hat{a}^\dagger\hat{a_p} + \hat{H_{SPM}}, \tag{6.24}$$

where ω_L is the frequency of the driving field, κ is the total, κ_0 is the intrinsic, κ_c is the coupling loss rate of ring resonator, $\hat{a}_{p,in}$ and $\hat{b_p}$ are the input driving and vacuum fields, respectively.

In [149], Hoff provides details to the solution of Langevin equation of motion 6.23 and further describes how to obtain the phase θ dependent spectrum, measured at sideband angular frequency Ω

$$S_\theta^{meas}(\Omega) = (1-\eta) + \eta S_\theta^{SPM}(\Omega), \tag{6.25}$$

where $\eta = \eta_c.\eta_{mo}.\eta_{qe}$ is the overall measurement loss defined as a product of outcoupling efficiency η_c, mode overlap η_{mo} and detection efficiency η_{qe}, respectively. The squeezing spectrum of the pump mode S_θ^{SPM} can be solved from Eq. 6.23 in a form of

$$\begin{aligned} S_\theta^{SPM} = 1 + G[2\kappa|\epsilon| - 2\kappa\left[2|\epsilon| - \Delta_p\right]\cos 2(\theta+\phi) - \\ \left[\kappa^2 + \Omega^2 - \Delta_p^2 + 4\Delta_p|\epsilon| - 3|\epsilon|^2\right]\sin 2(\theta+\phi)], \end{aligned} \tag{6.26}$$

$$G = \frac{4\kappa_c|\epsilon|}{\left[\Delta_p^2 + \kappa^2 - \Omega^2 - 4\Delta_p|\epsilon| + 3|\epsilon|^2\right]^2 + 4\kappa^2\Omega^2}, \tag{6.27}$$

where $\Delta_p = \omega_L - \omega_p = \zeta|\alpha_p|^2 = |\epsilon|$ is a particular condition of pump detuning that makes the resonant system stable. In that case, the nonlinear shift of the cavity resonance is compensated by the laser detuning, restoring the well known dependence between the intra cavity power and input pump power $|\alpha_p|^2 = 2\kappa_c/\kappa^2.|\alpha_{p,in}|^2$.

In Fig. 6.2 we show several cases of possible on chip generation of squeezed state of light to estimate initial experimental and fabrication parameters of the ring resonator. We use parameters that are standard for our fabricated process, such as low loss of 0.5 dB/cm at telecom wavelength and small radius of 30 μm. We evaluate that for an input power that we are able to obtain via lens coupling to the photonic chip, we should fabricate a ring with an escape efficiency between 70 - 80 % to generate squeezing between -5 to -6 dB at a sideband frequency ($\frac{\Omega}{2\pi}$) of 30 MHz.

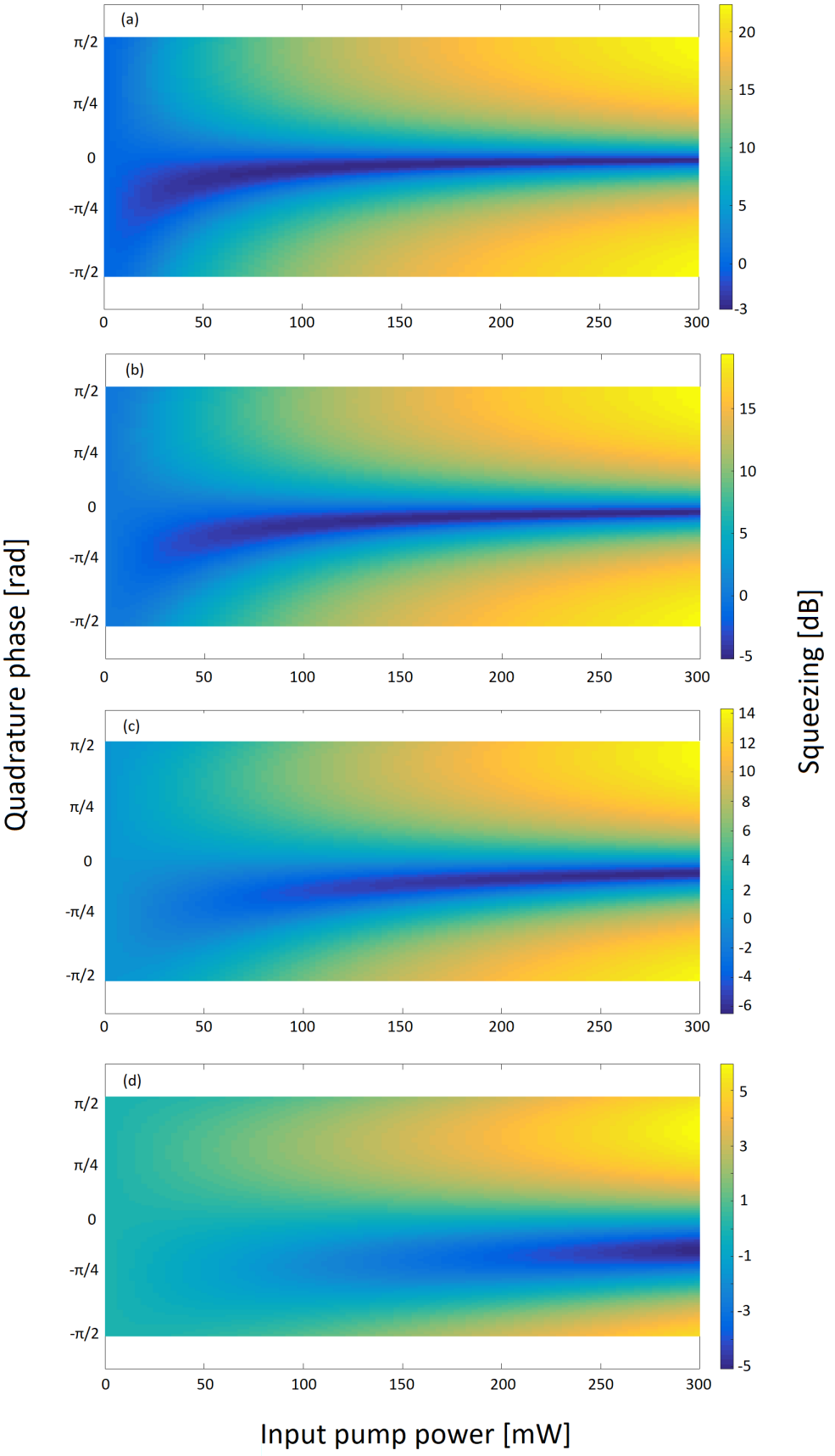

Figure 6.2: Numerical evaluation of possible squeezing and anti squeezing levels generated on chip for a ring resonator with 30 μm radius, 0.5 dB/cm loss and ζ of 9.4 for escape efficiencies of (a) 60%, (b) 70%, (c) 80% and (d) 90%.

6.2.5 Homodyne detection

Spatial homodyne detection

The most common method to measure quadrature squeezing is the balanced homodyne detection technique. Its implementation is based on superimposing a squeezed signal beam with a strong coherent beam, called local oscillator (LO), on a 50/50 beamsplitter. Afterwards, the two beams are measured using a balanced homodyne detector containing photodiodes with very similar quantum efficiencies. The difference of the output photocurrent can be read out via an electronic signal analyser resulting in a direct measurement of the quadrature variance. Additional readout of the amplitude or phase variance is performed by changing the phase of the local oscillator. The schematic representation is depicted on Fig. 6.3

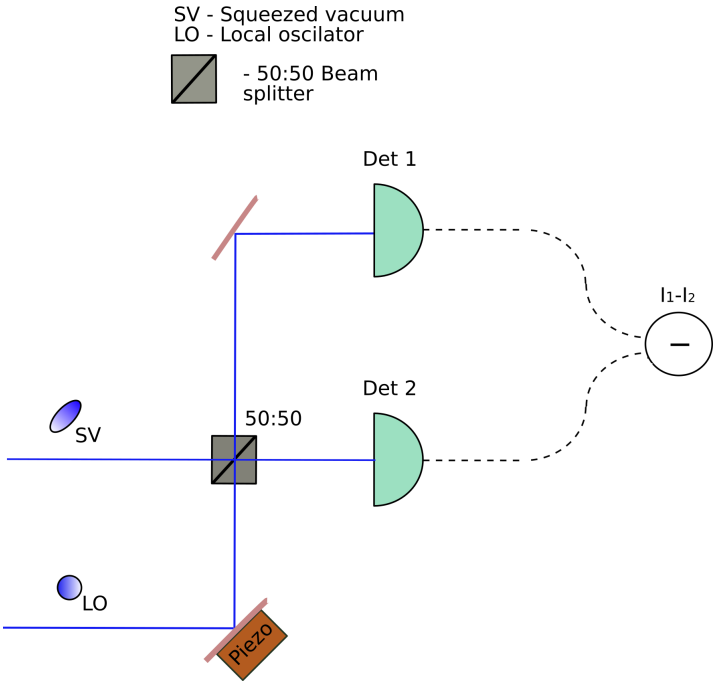

Figure 6.3: Spatial Homodyne Detection.

The mathematical description of balanced homodyne detection is following:
Imagine two optical beams interfering on a 50/50 beam splitter, where the signal beam can be described by the field operators

$$\hat{a}(t) = \alpha(t) + \delta\hat{a}(t), \tag{6.28}$$

while the LO beam is presented with a relative phase θ as

$$\hat{b}(t) = \left(\beta(t) + \delta\hat{b}(t)\right) e^{i\theta}. \tag{6.29}$$

After the interference effect, the two output fields are given as

$$\hat{c}(t) = \frac{1}{\sqrt{2}} \left((\alpha(t) + \delta\hat{a}(t)) - \left(\beta(t) + \delta\hat{b}(t)\right) e^{i\theta} \right) \tag{6.30}$$

and

$$\hat{d}(t) = \frac{1}{\sqrt{2}}\left((\alpha(t) + \delta\hat{a}(t)) + \left(\beta(t) + \delta\hat{b}(t)\right)e^{i\theta}\right). \tag{6.31}$$

The measured photocurrents from the two detectors are acquired by multiplying the respective modes with their complex conjugate

$$i_1(t) = g\hat{c}^\dagger(t)\hat{c}(t) \approx \frac{g}{2}\left[\alpha(t)^2 + \beta(t)^2 - 2\alpha(t)\beta(t)\cos\theta + \alpha(t)\left(\delta\hat{X}_1^a(t) - \delta\hat{X}_{-\theta}^b(t)\right) + \beta(t)\left(\delta\hat{X}_1^b(t) - \delta\hat{X}_\theta^a(t)\right)\right], \tag{6.32}$$

and

$$i_2(t) = g\hat{d}^\dagger(t)\hat{d}(t) \approx \frac{g}{2}\left[\alpha(t)^2 + \beta(t)^2 + 2\alpha(t)\beta(t)\cos\theta + \alpha(t)\left(\delta\hat{X}_1^a(t) + \delta\hat{X}_{-\theta}^b(t)\right) + \beta(t)\left(\delta\hat{X}_1^b(t) + \delta\hat{X}_\theta^a(t)\right)\right]. \tag{6.33}$$

When taking the difference in the photocurrents we get

$$i_2(t) - i_1(t) \approx g\left(2\alpha(t)\beta(t)\cos\theta + \alpha(t)\delta\hat{X}_{-\theta}^b(t) + \beta(t)\delta\hat{X}_\theta^a(t)\right), \tag{6.34}$$

where g is the electronic gain of the two detectors which we consider to be equal. An important condition for homodyne measurement is that the power of the local oscillator must be much stronger than the power of the signal, $\beta \gg \alpha$. In such case we can obtain the spectral variance of the differential signal as

$$\delta i_-(\Omega) \approx g^2\beta(t)^2\delta\hat{X}_\theta^a(\Omega) \tag{6.35}$$

and therefore directly measure the variance of the signal field.

Polarization homodyne detection

As we encode information of the measured squeezed vacuum (SV) in the horizontal (H) polarization and the LO into vertical (V) polarization, we perform the homodyne detection technique in the polarization degree of freedom. The intrinsic advantage of this scheme is that we do not need to lock the phase of the two polarizations because they propagate in the same spatial mode. Therefore, no additional electronics is needed that could potentially reduce the amount of squeezing due to imperfect feedback control. In Fig. 6.4 we show the configuration for performing polarization homodyne detection.

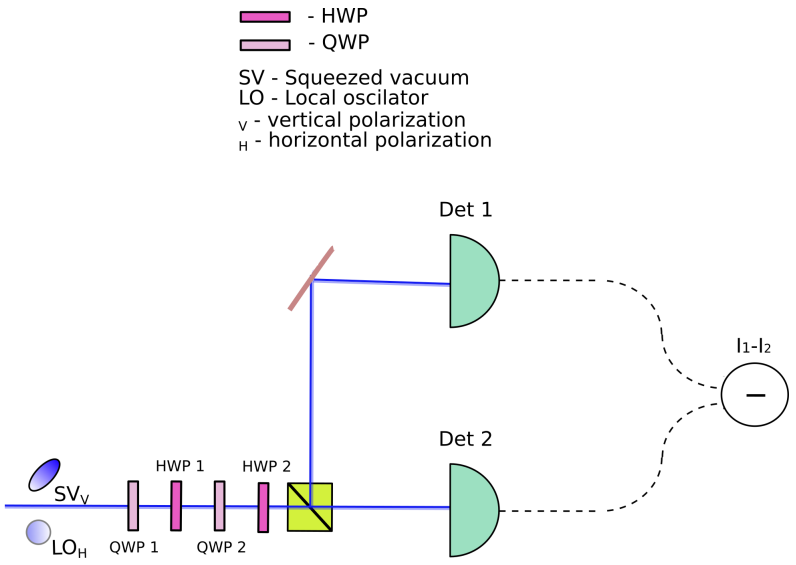

Figure 6.4: Polarization Homodyne Detection.

We use two quarter waveplates (QWP1, QWP2) and two half waveplates (HWP1, HWP2) in a following way: first two waveplates QWP1 and HWP1 are used to correct any acquired phase delay between the two orthogonal polarization throughout the setup and therefore rotate any arbitrary input state to a horizontal state $|H\rangle$ on the Poincare sphere. Afterwards, we use another QWP2 at 22.5° to set the output state at right circular state $|R\rangle$. In order to obtain arbitrary phase difference between the measured SV encoded in $|H\rangle$ state and LO in its orthogonal counterpart we use another HPW2 and polarization beam splitter (PBS). In this case we satisfy both conditions to realize efficient polarization homodyne: Equal powers in both detectors and perform full phase tomography of the measured state.

6.3 Squeezing Experiment I: Free space Sagnac interferometer

Historicaly, self phase modulation is one of the first nonlinear processes that was used to generate squeezed states of light. First experiment regarding Kerr squeezing was done in optical fibers where 0.6 dB of noise below the vacuum noise was measured [49]. The biggest obstacle during the measurement was to avoid spurious intrinsic noise generation of Guided Acoustic Wave Brillouin Scattering (GAWBS) that could span over several GHz. In order to avoid it, the fiber was cooled down to 4.2K.

Spatial Sagnac interferometer

After the realization of limiting effects in optical fibers, another effective way to remove

the intinsic noise of GAWBS was established on symmetric sagnac interferometer [150] shown in Fig.6.5

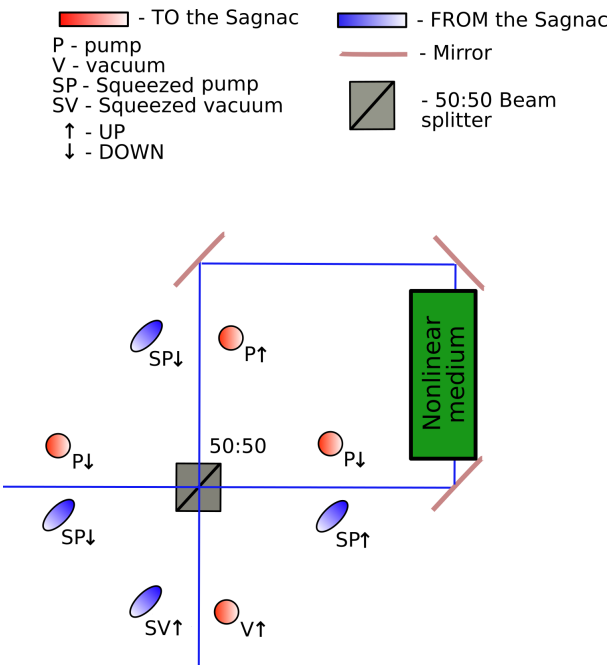

Figure 6.5: Spatial Sangac interferometer.

A pump beam enters the interferometer from one side of the 50/50 beam splitter while a vacuum state enters from the other port. The pump is then split and occupies the two orthogonal paths (UP, DOWN) where it starts to interact with the Kerr medium. The two coherent states then start to get squeezed via the light matter interaction. Both counter-propagating squeezed states of light then reinterfere on the 50/50 beam splitter resulting to an squeezed coherent state propagating back throught the input port while a squeezed vacuum state is generated on the output port. In the first experiment [151], [152] the squeezed coherent state was reused as a LO to measure the amount of squeezing in the other port. The beauty of the sagnac loop is that it is phase stabilized and at the same time, it works as a natural purifier of quantum correlations where any classical noise such as Brillouin, Raman scattering or even technical noise of the laser can be cancelled out [153].

Polarization Sagnac interferometer

Instead of encoding into spatial mode of the interferometer, information can be encoded in polarization by using waveplates realizing a polarization sagnac loop as shown in Fig. 6.6.

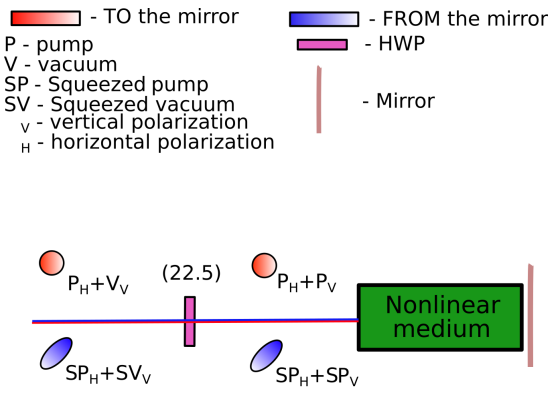

Figure 6.6: Polarization Sangac interferometer.

A H polarized input pump beam is diagonally polarized by HWP set at 22.5 °. The two polarizations of the light then interact with a nonlinear medium and get squeezed. If we imagine a mirror at the end of the medium, the beam gets backreflected and continues to propagate in the Kerr medium to form an output superposition of squeezed coherent state in both orthogonal polarizations. When such a state passes through the HWP again, it reinterferes with itself to produce a squeezed coherent state in H polarization meanwhile the orthogonal V polarization generates squeezed vacuum similarly as in the case of spatial encoding.

Hyper-encoded Sagnac interferometer

One of the biggest concern that we take into consideration when designing the experimental setup is the implementation of homodyne detection. In order to avoid either scanning or locking the phase of the LO in a conventional way, we decide to encode information into polarization rather than space. In that case we have to assure that the LO and SV would be in the same spatial mode but orthogonal polarization. That is not possible to achieve in either experimental designs of Fig. 6.5 nor Fig. 6.6. In the first case, its intrinsic that both of the beams are spatially separated prior the detection. In the second case, when a diagonally polarized beam propagates in the chip with the microring resonator, one polarization can be resonantly coupled but the other not due to different propagation constant. Therefore, we have to combine both types of encoding into Hyper-encoded Sagnac interferometer as depicted in Fig. 6.7.

An initial H polarized pump beam interacts with a PBS that is slightly rotated around its axis. This is a crucial element of the setup since it ensures that both the SV (encoded in V) and LO (encoded in H) are at the same spatial mode enabling the polarization homodyne measurement. In such configuration rotating the PBS provides most of the H polarized pump beam in the transmitted port but some is reflected and dumped into an empty port. On the other hand, when the pump is V polarized 100% of the power is reflected, minimizing additional loss for SV. Such a partially polarizing beam splitter

is also very useful for flexible tuning the amount of power in LO for efficient homodyne detection. When most of the H power passes through the PBS, next in line is a HWP that is set at 22.5 ° encoding H into H+V polarization. The optical beam is afterwards spatially split via another PBS, hyper-encoding the information into a superposition of two orthogonal spatial and polarization states. In the path of V polarized beam is yet another HWP set at 45 ° switching the V to H polarization, ensuring that both counter propagating beams are on resonance with the ring resonator. Afterwards, both beams are coupled, squeezed in the ring and outcoupled at the same time via high NA lens. On the way back, one of the squeezed coherent state SP_H passes through the PBS, while the other one passes through the HWP rotating the H into V polarization SP_V that gets reflected by the PBS into common spatial mode preparing a superposition of $SP_H + SP_V$. Such a superposition reinterferes with itself at the HWP, producing SP_H in H but at the same time squeezed vacuum SV_V in V. On the way back, the squeezed states pass through the rotated PBS, where SV_V is fully reflected and SP_H is also partially reflected into the same spatial mode, serving as a LO.
The performance of the Sagnac interferometer can be evaluated by the visibility V_{int} of the interference effect as

$$V_{int} = \frac{P_{in} - P_{out}}{P_{in} + P_{out}}, \tag{6.36}$$

where P_{in} and P_{out} is the measured input power before the loop and output power from the interferometer. We check the visibility without the sample and achieve reasonable result of 98%. We also test the visibility of the Sagnac with a polished sample containing a waveguide with a coupled ring resonator to obtain an unfortunate visibility result fluctuating from 66% to 96%. We believe that the time variations of the interference effect come from independent mechanical fluctuations of the two coupling lenses producing a time dependent spatial overlap of the two optical spots.

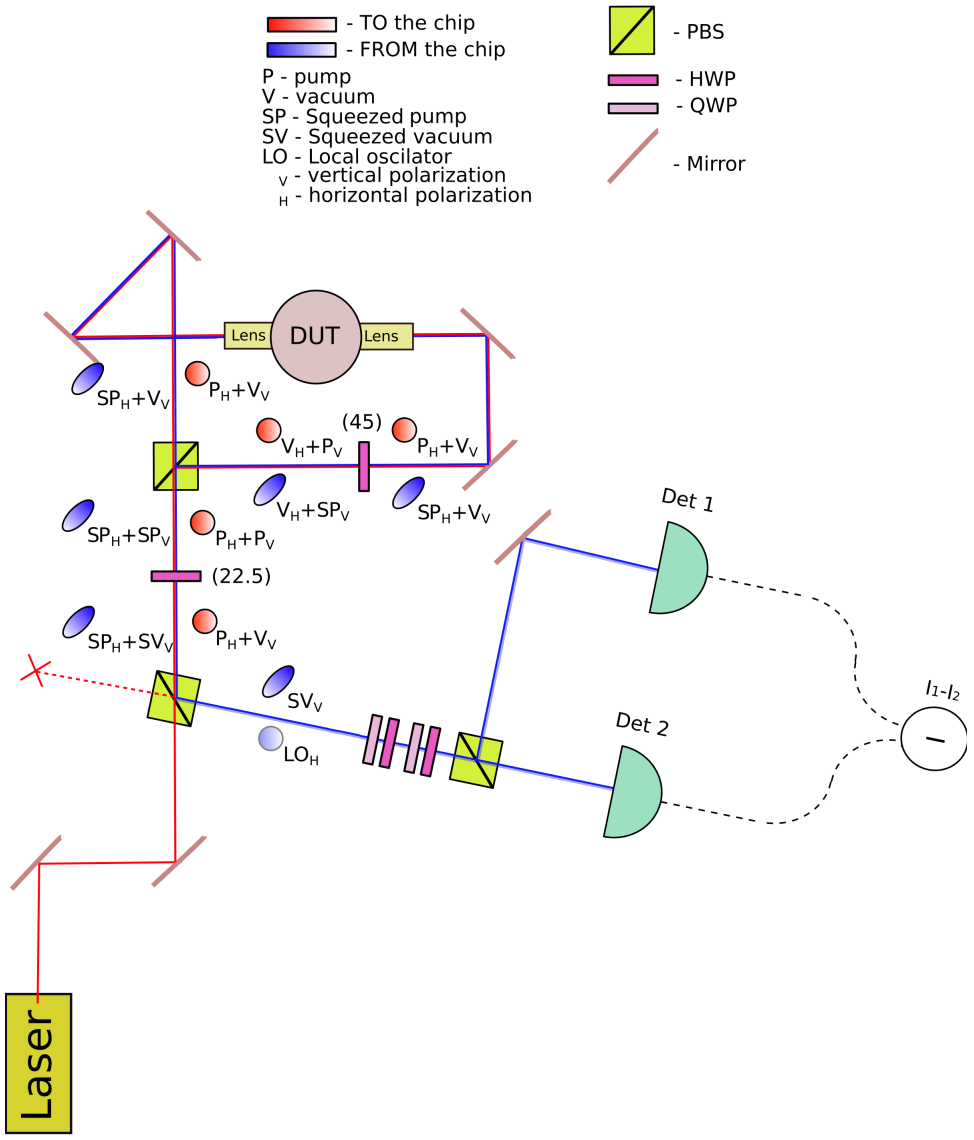

Figure 6.7: Hyper-encoded Sagnac interferometer.

6.4 Squeezing Experiment II: Integrated Sagnac interferometer

In order to solve the issue with interferometric stability of the setup we decide to integrate the Sagnac on a photonic chip. The loop is composed of a long waveguide and a 2x2 multimode interference device (MMI) that plays the role of a 50:50 beam splitter. Consequently, we can still apply polarization encoding as the MMI can be designed to work as a balance splitter for one polarization and unbalanced for the other.

6.4.1 Design of the photonic chip

Waveguide design

The amount of squeezing is strongly limited by the propagation loss of the ring resonator. In order for the device to perform at its best we design the waveguide width of the cavity to be 1880 nm. The thickness of the sample is limited to 500 nm due to etching selectivity between the resist and SiN. In Fig. 6.8 we show the field distribution of the fundamental waveguide TE mode.

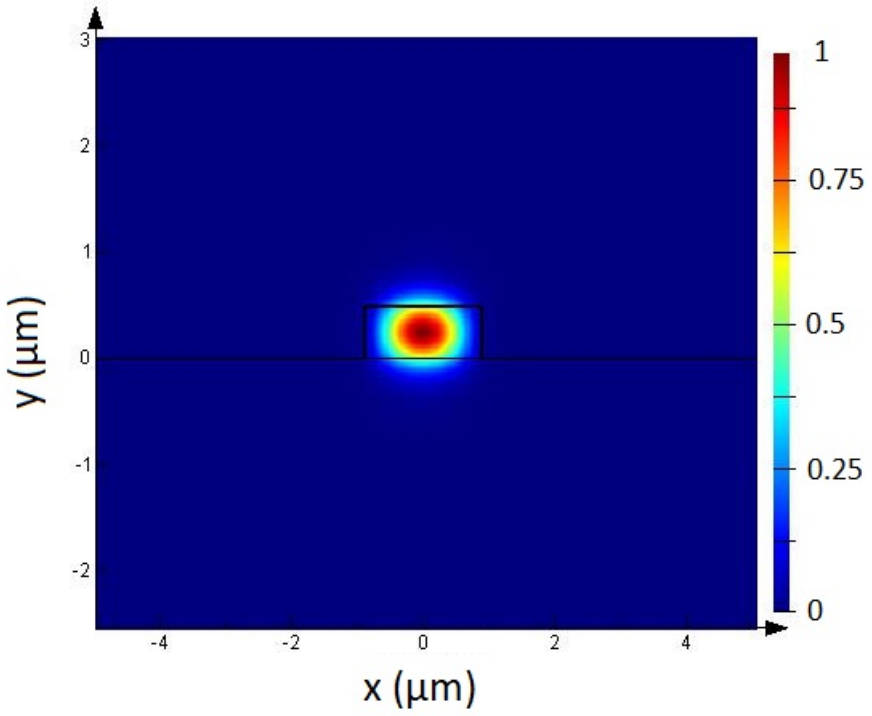

Figure 6.8: Mode distribution of waveguide for squeezing experiment.

MMI design

The most important part of the photonic device is the design of the 50:50 beam splitter. It has been shown, that a multi mode interference (MMI) device works as a perfect splitting mechanism to achieve full quantum interference equal to the one of a directional coupler [154]. Since we want to use the polarization homodyne detection scheme we design the MMI in our sample to work as a perfect 50:50 beam splitter for the fundamental TE mode that we use as a source for generating SV, while at the same time it splits unequally the TM mode in order to obtain some light in the dark port to use it as a LO. We report a simulation of a MMI shown in Fig. 6.9 with a 100 μm long input ports and different lengths of the apparatus.

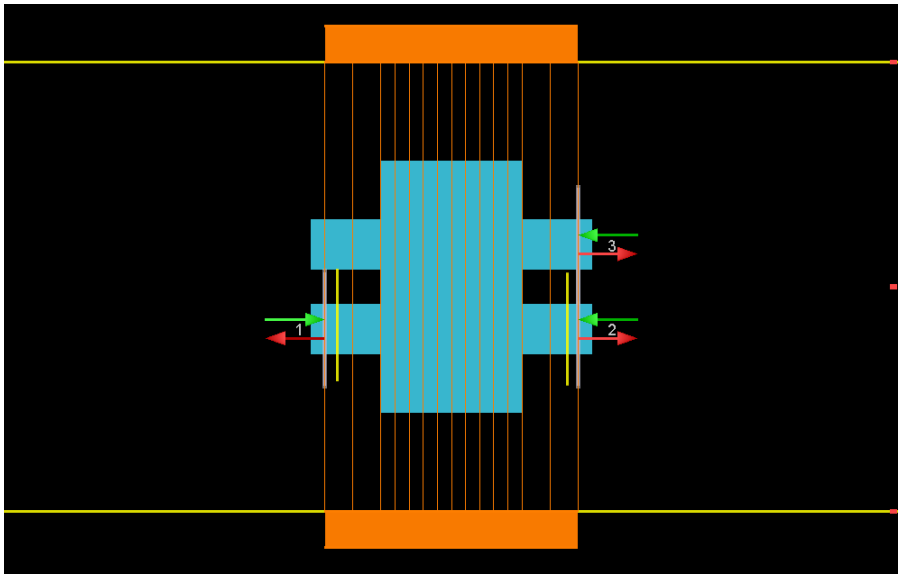

Figure 6.9: Design of the multi mode interference device presented in Lumerical Mode Solutions software.

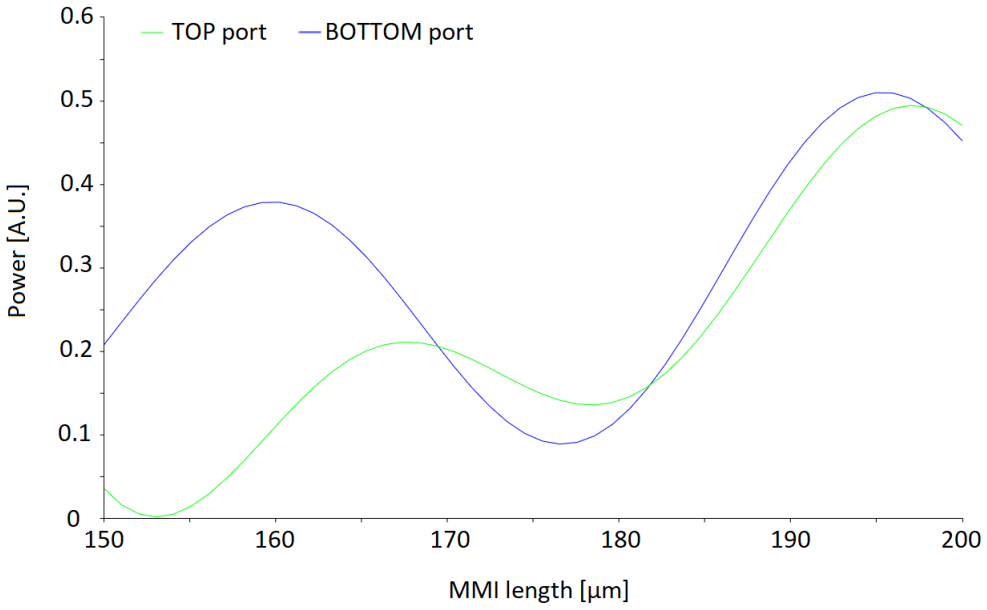

Figure 6.10: Power distribution of each port in a MMI device for a fundamental TE mode.

In Fig. 6.10 we show results of power distribution of individual output ports of the MMI for the fundamental TE mode. The device achieves self imaging condition at around 135 μm of body size while at the 197 μm length we obtain a perfect, low loss 50 : 50 splitter. We show the mode propagation in a 197 μm long MMI device in Fig. 6.11 to

illustrate the complicated field distribution.

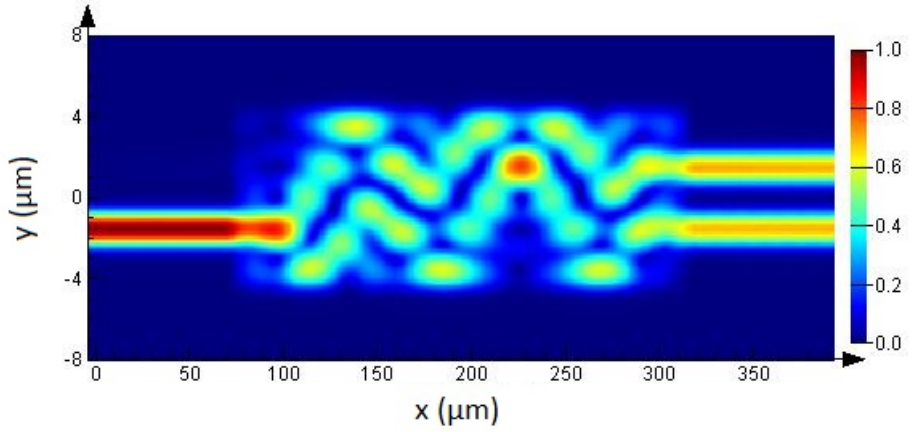

Figure 6.11: Power propagation of the fundamental TE mode in the MMI device of length 198 μm.

At the same time we perform the same simulation shown in Fig. 6.12 for the fundamental TM mode of the identical MMI device to confirm that we obtain a highly unbalanced splitter for the orthogonal polarization that serves for our purpose. The field propagation is shown in Fig. 6.13.

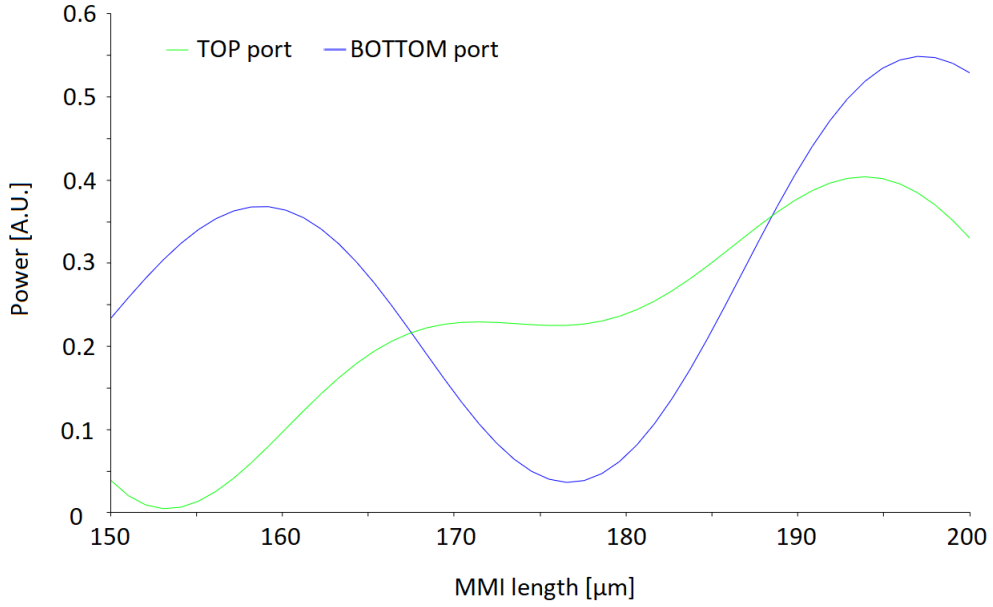

Figure 6.12: Power distribution of each port in a MMI device for a fundamental TM mode.

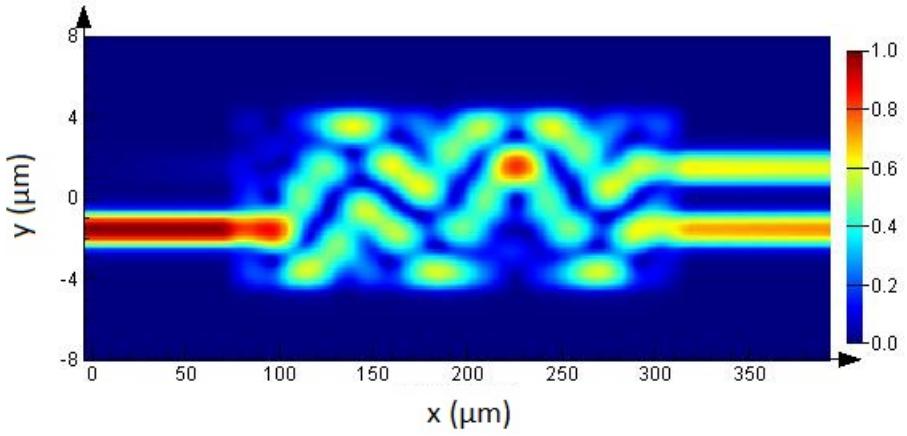

Figure 6.13: Power propagation of the fundamental TM mode in the MMI device of length 198 μm.

Overcoupling Ring resonator

Another strict condition for an efficient generation of squeezed vacuum is to obtain a highly overcoupled ring resonator. For that purpose we design a short section of 50 μm long waveguide with a width of 900 nm that is tapered in and out of the fundamental waveguide shown in Fig. 6.8. Since the possible gap between the bus waveguide and the ring is limited to 100 nm due to verticality of the fabrication process, the narrow waveguide pushes the optical field out more to achieve higher coupling ideality of the resonator [155].

Fabricated device

In Fig. 6.14 we show an optical image of the fabricated photonic chip consisting of a 2x2 MMI structure and four ring resonators embedded in the middle of the Sagnac interferometer.

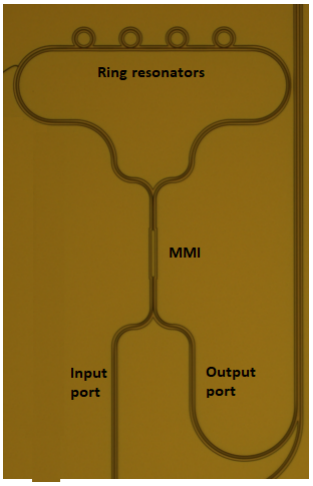

Figure 6.14: Optical image of the fabricated photonic chip.

First we characterise the part of the device without a MMI, realizing a transmission measurement with a tunable fiber-coupled TSL-510 laser, to determine whether we fulfil the strict fabrication conditions for a successful squeezing experiment. The on chip coupling is performed by grating couplers and the measured spectrum of four rings with a 30 μm radius is shown in Fig. 6.15. All resonators were highly overcoupled (<70%) with an average intrinsic Q-factor around 950k, corresponding to 0.35 dB/cm of propagation loss.

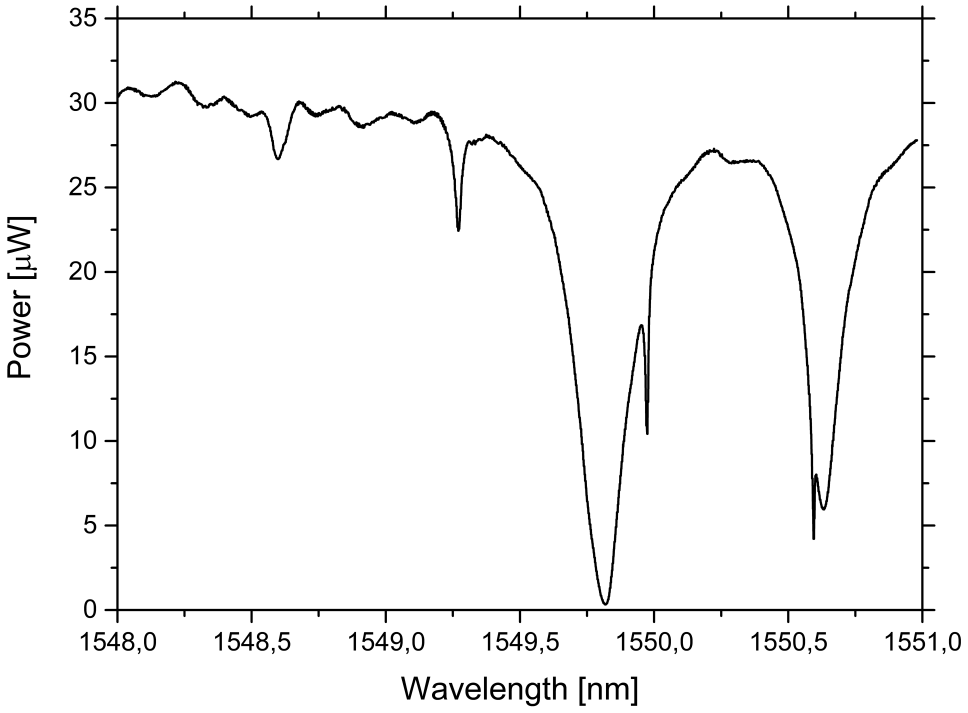

Figure 6.15: Resonances of the four ring resonators showing a promising average intrinsic Q-factor of 950k in a highly overcoupled regime (<70%). The four sharp resonances correspond to the fundamental mode of different rings (Fig. 6.14) while the two broader resonances are their higher order modes.

6.4.2 Experimental setup

The experimental setup is depicted in Fig. 6.17. The TSL-510A is fiber coupled to an erbium doped fiber amplifier (EDFA) to obtain 460 mW of output power. Afterwards we use a HWP1 with a polarizing beam splitter (PBS) to control the input power that has been coupled to the optical chip via a high NA (0.7) lens achieving an incoupling efficiency of 25 % for H and 30 % for V polarization, respectively. We use another HWP2 that is set at 45/55 of the H/V ratio to couple light that is used both as a source for generating SV (H polarization) and as LO (V polarization). In the chip the H polarization is split via the MMI to two equal beams which are frequency tuned and resonantly

coupled to a microring structure where the beams are squeezed via self phase modulation. The optical spectrum of the ring used during the experiment is measured via back propagation of the light from the Sagnac loop, see Fig. 6.16. Its estimated loaded Q-factor is around 238k with an escape efficiency of 77 %. The two squeezed coherent beams then counter-propagate and reinterfere on the MMI where the SV continues its propagation in the output port while the pump is rejected and propagates further back through the input port. At the same time V polarization, being off resonant from the ring, is unequally split and recombined back on the MMI rejecting great portion of the pump in the input port but at the same time small amount of the light further propagates in the output port. Afterwards both beams, the SV and the LO, are outcoupled from the output port with another high NA lens. We use a set of Thorlabs lenses (f1=100mm, f2=75mm) to minimize the coupling losses to the optical fiber. The overall outcoupling efficiency including mode overlap between the SV and LO is estimated to be around 3.25 dB. Using four waveplates and a PBS we measure the noise reduction with a polarization homodyne detection scheme described in Sec. 6.2.5.

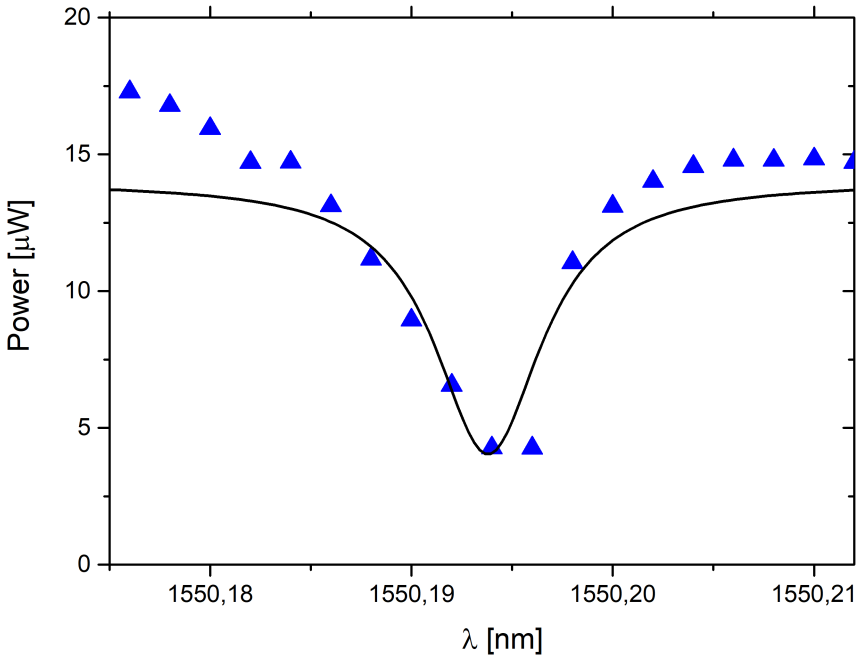

Figure 6.16: Optical spectrum of a ring resonator used during the experiment with an estimated Q-factor of 238k and an escape efficiency of 77 %.

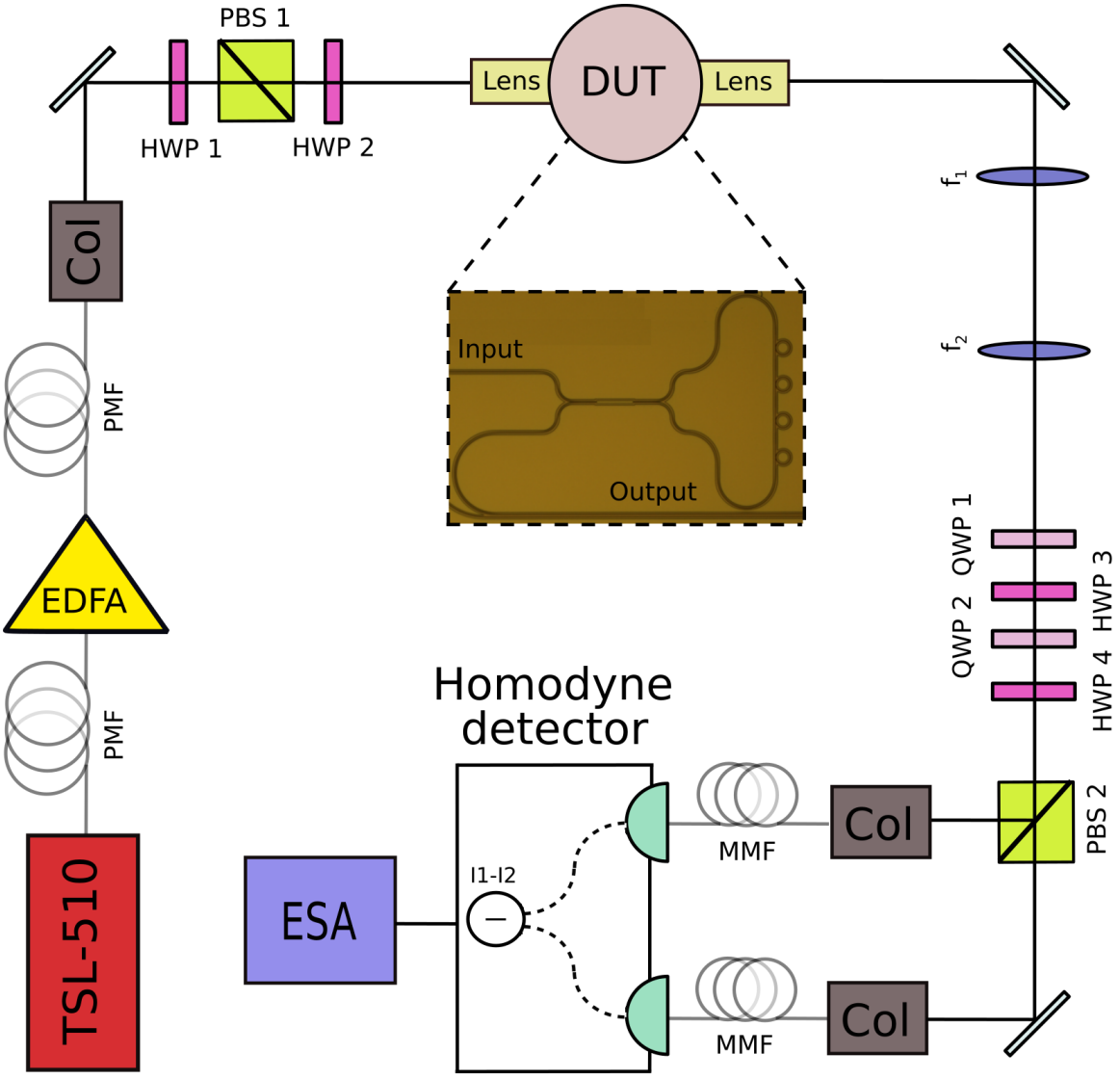

Figure 6.17: Schematic setup for on chip generation of broadband quadrature squeezed states. An amplified optical beam in a diagonal polarization is coupled to the photonic chip via lens coupling. In the chip the H polarization is split by a 2x2 MMI and used to produce SV in the output port via reinterference from the back propagation of two squeezed coherent states in the Sagnac loop. On the other hand, V polarization is unequally split and used as a LO. The SV and LO are outcoupled by another lens and measured via polarization homodyne measurement (Detector: WL-BPD1GA (Wiserlabs electronics)). PMF: polarization maintaining fiber, EDFA: erbium doped fiber amplifier, COL: collimator, HWP: half waveplate, QWP: quater waveplate, PBS: polarizing beam splitter. DUT: device under test, MMF: Multi mode fiber (FC/APC to avoid interference effects in the fiber), ESA: electronic spectrum analyser (AEROFLEX 3252).

6.4.3 Experimental results and noise analysis

In Fig. 6.18(b) we characterise the amount of squeezing for three different input powers, (52 mW, 39 mW and 26 mW) before the Sagnac interferometer. We measure maximum squeezing of 0.45 dB spanning over 300 MHz. The inferred level of squeezing corrected for the measurement efficiency is estimated to be 1 dB. Also, in Fig. 6.19(a) we compare the measured squeezing (SQ) and antisqueezing (ASQ) spectrum and confirm that in each case the Heisenberg uncertainty relation is fully satisfied. One of the measurements regarding the highest power of 52 mW shows a cross over with another dataset for lower power. We suspect that this unexpected behaviour can be explained by imperfect alignment of the ASQ variance set by HWP4. In Fig. 6.19 (b) we numerically calculate two ASQ spectra for different powers being perfectly aligned during the homodyne measurement and an additional simulation of the ASQ for higher power being misaligned resembling similar behaviour shown in Fig. 6.19 (a).
Looking at Fig. 6.18(b) in more detail one can notice that we do not observe any squeezing at low frequencies as it would be expected. Quite the contrary, we measure vast amount of noise that prevents us to see squeezing until we reach certain high frequency. We strongly suspect that the spurious noise at short frequencies arises from the temperature dependend refractive index variations of the material [156] that are coupled to the phase noise of the laser. In the next sections we experimentally and theoretically evaluate its generation and filtering in the photonic chip.

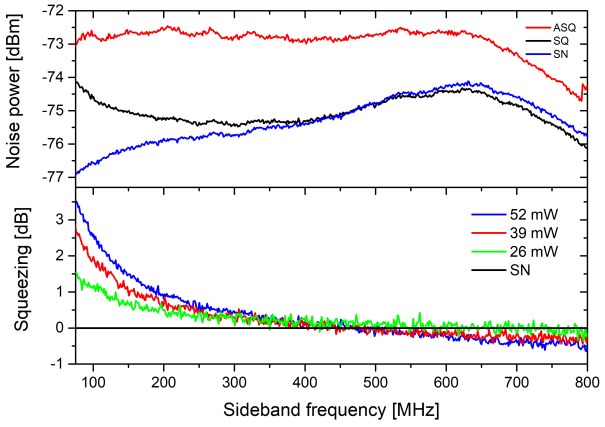

Figure 6.18: a) Noise spectrum for measured squeezing (SQ), antisqueezing (ASQ) and shot noise (SN). The video (VBW) and radio (RBW) bandwidths are set up at 100 kHz and 20 Hz, respectively. Each line is an average of five measurements where each measurement have a sweep time of 10s. b) Squeezing spectrum, for three different input powers before the 50/50 beam splitter, that has been corrected for the noise of the detector and normalized to the SN level. SN is measured off resonance with an input light being purely V polarized.

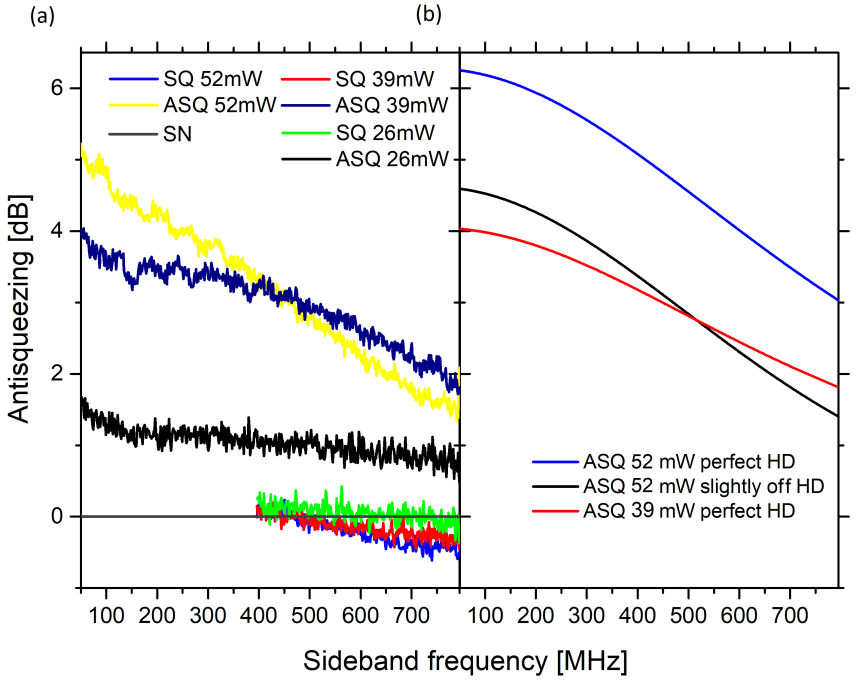

Figure 6.19: a) Comparison between the measured squeezing, antisqueezing and shot noise spectrum for three different pump powers each one satisfying the Heisenberg uncertainty relations. (b) Simulation providing a possible explanation regarding unexpected behaviour of ASQ in 6.19(a). Calculated two ASQ spectra for two different powers of 52 mW and 39 mW being perfectly aligned during the homodyne measurement. The black line demonstrates an imperfect homodyne measurement (HD) set by HWP4 of the ASQ spectrum for 52 mW power. Please note these are just examples that do not try to fit any theory.

6.4.3.1 Experimental characterization of the thermorefractive phase noise in ring resonator

As it is shown in [157] the thermal noise has its unique dependence on the sideband frequency. At low frequency approximation the spectrum of the thermal fluctuations can be described as $S(\Omega) \sim 1/\Omega^2$. To understand if this is also our case we make two assumptions. First, we assume that after the measurement the squeezing spectrum at short frequencies is dominated only by thermal noise. Second, we assume that the quadratic behaviour of the thermorefractive noise is not affected by the power enhancement in the ring resonator nor the rejection of the Sagnac interferometer. Therefore, we describe the squeezing spectrum as $S(\Omega) = A/\Omega^2$, where A is a frequency independent parameter that contains the effects of the microring, Sagnac and overall outcoupling losses. After our assumptions, we show in Fig.6.20(a) that the measured shot noise normalized squeezing spectrum at low frequencies can be quite well described by such an inverse quadratic function, supporting our initial proposition for the origin of the

unwanted noise. Another characteristic for this type of the noise is its linear power dependence. To prove this, we subtract the measured squeezing spectrum at 52 mW and 39 mW and compare it with subtracted squeezing spectrum at 39 mW and 26 mW. By knowing that the difference of the input powers in both cases is the same (13 mW) we can conclude that the overlap that is shown in Fig.6.20(b) provides sufficient evidence that the noise depends linearly on the power.

Finally, to gain full confidence about the origin of the noise, we investigate whether it shows a quadratic temperature dependence. As we can observe the thermorefractive phase noise in the amplitude spectrum via direct measurement (explanation in subsection 6.4.3.3), we tune the wavelength of the laser to pass the resonance of the ring resonator and at the same time we perform a 60 second measurement of the transmitted signal using ESA set at 100 MHz sideband frequency, obtaining an electronic spectrum shown in Fif. 6.21 (a). Afterwards we compare the measured noise OFF resonance with the same power as the one that was measured on resonance. In Fig. 6.21 (b) we show the temperature dependence of the noisy spectrum at 10°C, 20°C and 30°C, confirming the quadratic behaviour of the spurious effect having a thermorefractive origin.

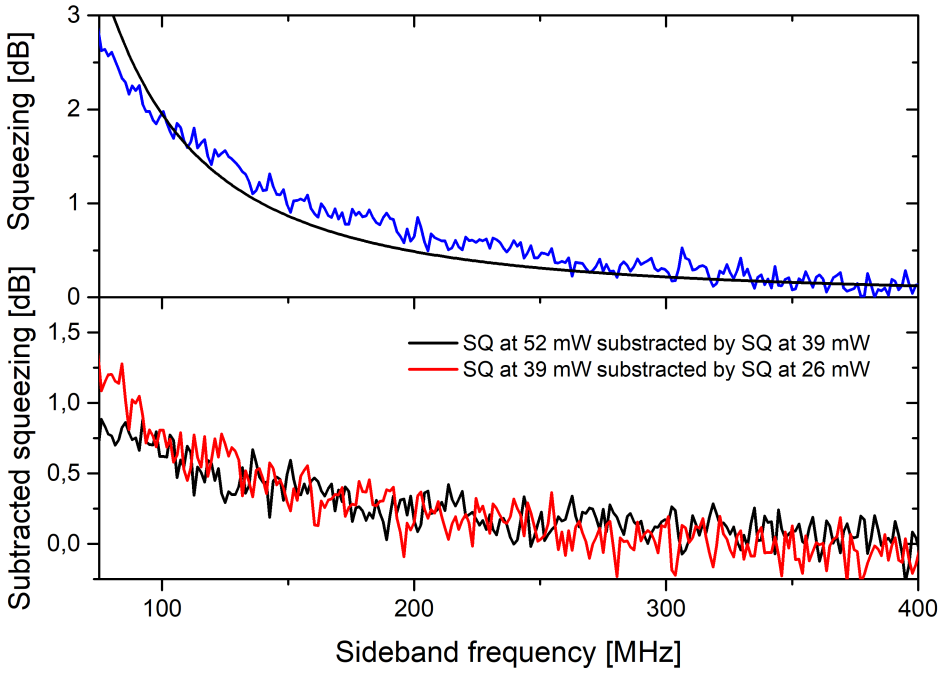

Figure 6.20: (a) Squeezing spectrum with an input power of 39 mW that is fitted with $S(\Omega) \sim A/\Omega^2$. (b) Subtracted squeezing spectra showing that the thermal noise depends linearly on the input pump power.

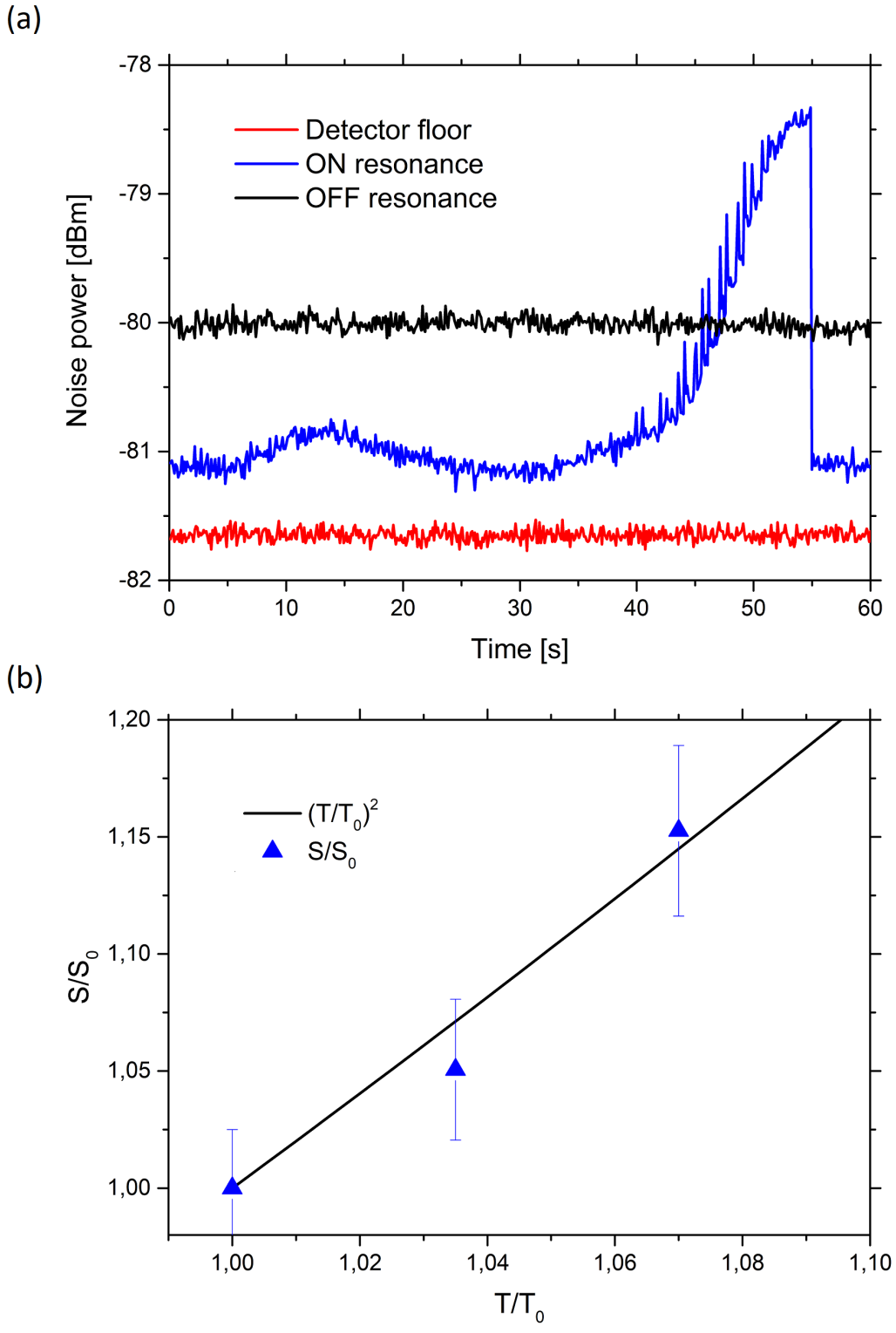

Figure 6.21: (a) Time dependent measurement at 100 MHz sideband frequency, where we tune the laser through the resonance in order to compare the noise spectra ON and OFF resonance at the same power. (b) Temperature dependence change of the spectral intensity S normalized to initial spectrum S_0 at measured temperature T_0. The black line shows the theoretical quadratic scaling of the spectrum.

6.4.3.2 Generation and elimination of thermorefractive phase noise in the Sagnac interferometer

We theoreticaly investigate the amount of thermorefractive phase variations that are produced and subsequently cancelled out by a filtering effect of the Sagnac interferometer with a length L. We follow the treatment initially described in [158], where the uncorrelated phase fluctuations are generated in an input point x of the loop up to the output point L. The phase perturbation of the two counter-propagating beams can be described by a transfer function

$$F(\Omega, x) = e^{i\frac{\Omega n_{eff}}{c}(L-x)} - e^{i\frac{\Omega n_{eff}}{c}x}, \tag{6.37}$$

where we further define $k = \frac{\Omega n_{eff}}{c}$. The generated noise in an elemental length dx that is transferred to the output port of the Sagnac can be written as

$$dS_{out} = \frac{S_{tpn}}{L}|F(\Omega, x)|^2 dx \tag{6.38}$$

where S_{tpn} is the thermorefractive phase noise defined as

$$S_{tpn} = 4\left(\frac{dn}{dT} + n_{eff}\alpha_L\right)^2 \frac{2\pi T^2 k_b L}{\kappa\lambda_p} \ln\left[\frac{\left(k_{max}^2 + \left(\frac{\omega}{v}\right)^2\right)^2}{\left(k_{min}^2 + \left(\frac{\omega}{v}\right)^2\right)^2}\right], \tag{6.39}$$

with values and definitions of each parameter is shown in Table I. Furthermore,

$$|F(\Omega, x)|^2 = \sqrt{Re(F(\Omega, x))^2 + Im(F(\Omega, x))^2}^2, \tag{6.40}$$

has a real part

$$Re(F(\Omega, x))^2 = (\cos[k(L-x)] - \cos(kx))^2 = 4\sin^2\left[\frac{k}{2}(L-x) - \frac{k}{2}x\right]\sin^2\left[\frac{k}{2}(L-x) + \frac{k}{2}x\right] \tag{6.41}$$

and an imaginary part

$$Im(F(\Omega, x))^2 = (i\sin[k(L-x)] - i\sin(kx))^2 \tag{6.42}$$

where k, L and x are real numbers, therefore we can write

$$Im(F(\Omega, x))^2 = 4\sin^2\left[\frac{k}{2}(L-x) - \frac{k}{2}x\right]\cos^2\left[\frac{k}{2}(L-x) + \frac{k}{2}x\right]. \tag{6.43}$$

If we insert Eq. 6.41 and Eq. 6.43 into Eq. 6.40 we obtain

$$|F(\Omega, x)|^2 = 2 - 2\cos[k(L-2x)]. \tag{6.44}$$

Integrating over the length L of the Sagnac interferometer we can obtain the spectrum of the thermorefractive phase noise at the output port

$$S_{out} = \frac{S_{tpn}}{L}\int_0^L |F(\Omega, x)|^2 dx = 2HS_{tpn}, \tag{6.45}$$

where we retrieve the H as in [158]

$$H = 1 - \frac{\sin(kL)}{kL}. \tag{6.46}$$

Consequently, H represents a high-pass filtering function that strongly depends on the size of the Sagnac itself, as shown in Fig. 6.23. The thermal fluctuations produced at short sideband frequencies are classically correlated and thus filtered out by the Sagnac interferometer. On the other hand, at sideband frequencies whose wavelengths are comparable with the size of loop, the noise is uncorrelated and therefore continues to propagate further to the output port. Using Eq. 6.45, we numerically examine the amount of thermorefractive noise produced in the Sagnac and the effect of the filter. During our calculation we approximate the waveguide geometry to the geometry of the optical fiber. Even though the approximation is lenient on the confinement factor and therefore generating less thermal fluctuations, the effect of the filtering is several magnitudes stronger. The results are shown in Fig.6.22 where we can compare the noise produced in the waveguide, before and after filtering in respect to shot noise that is defined as

$$S_{SN} = \frac{2hf_p}{0.5^2\eta_{det}P_{in}}. \tag{6.47}$$

We can see that the Sagnac filters out more than 100 dB of phase noise at low frequencies while at high frequencies we can achieve around 30 dB of rejection. On top of that, in comparison to the shot noise power the unwanted noise is very small, therefore we can assume its generation outside of the ring resonator as negligible.

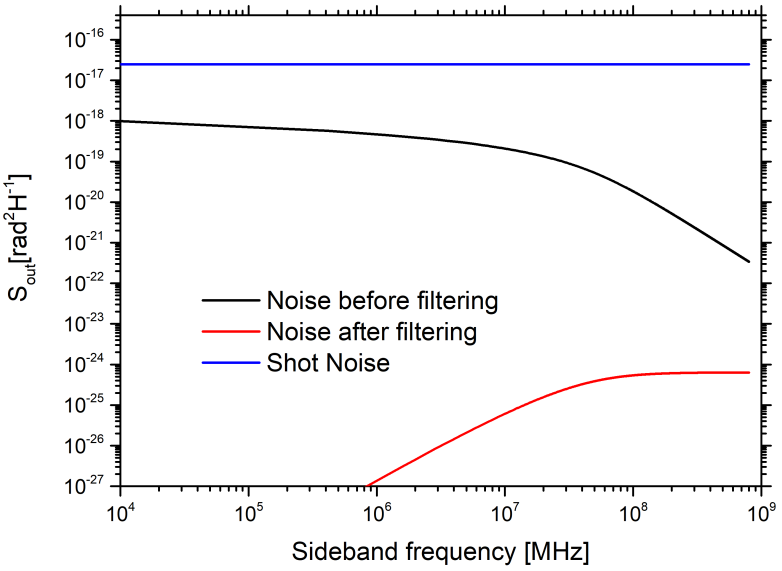

Figure 6.22: Numerical calculation of thermorefractive noise produced in the Sagnac interferometer before and after filtering compared with shot noise calculated for 52 mW of input power.

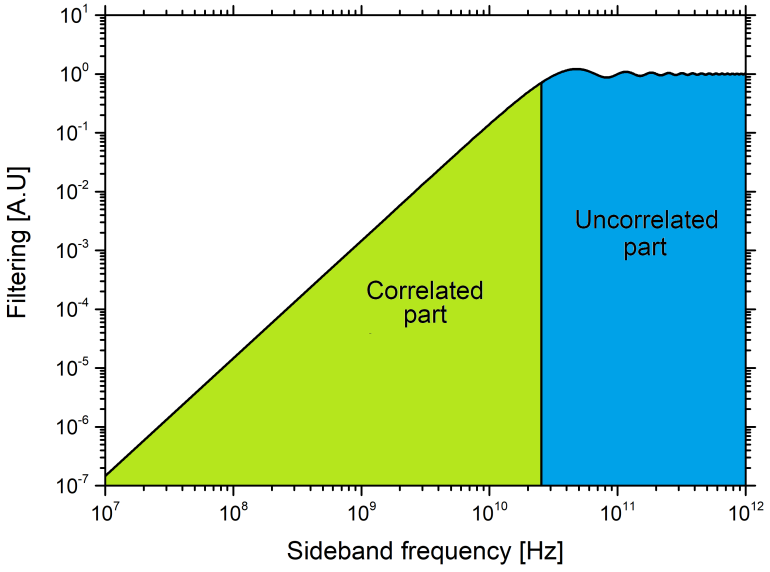

Figure 6.23: Filtering function of a Sagnac interferometer with L=2.6 mm separated into two parts. The green section is filtering the correlated part of the uncorrelated thermorefractive noise generated in the two arms of the loop while the blue section passes by its uncorrelated part. The vertical black line shows a 3 dB separation.

At this point we ask following question regarding our experiment: If we assume that the loop does not introduce noise in our measurement and we consider a situation where the phase fluctuations are produced at some location x inside the Sagnac, illustrated in Fig. 6.24. Would the output spectrum of the thermorefractive noise be independent of the position x? This is an important question and investigates whether the phase noise produced in the ring resonator depends on its position in the interferometer. For that purpose we define $L_1 = x$ as the position of the noisy source, $L_2 = L - x$ as the position of the output port at the 50/50 beam splitter and therefore $L = L_1 + L_2$. In such case we can calculate the output spectrum of the thermorefractive phase noise as

$$S_{out} = \frac{S_{tpn}}{L} \int_{L_1}^{L_2} |F(\Omega, x)|^2 dx = 2HS_{tpn}, \tag{6.48}$$

where

$$H = \frac{(L_2 - L_1)}{L} - \frac{\sin\left[k(L_2 - L_1)\right]}{kL}. \tag{6.49}$$

If we assume $L_1 \approx L_2$ we can expand the Eq.6.50 as

$$H = \frac{k^2 (L - 2x)^3}{6L}. \tag{6.50}$$

As expected from Eq. 6.50, the magnitude of reduction strongly depends on the position of the noisy source and therefore on the overall symmetry of the Sagnac. For that purpose we can conclude that to improve the noise filtering the microring resonator should

be placed in the middle of the interferometer.

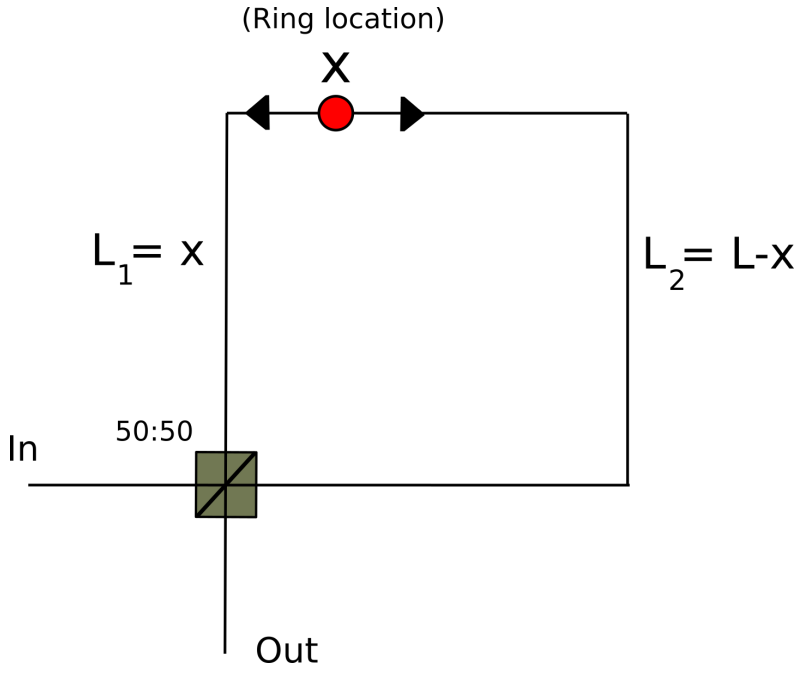

Figure 6.24: Schematic representation of generation of thermal fluctuations from a point source located at position x inside the Sagnac interferometer.

In order to estimate the amount of unwanted phase noise generated in the ring resonator we use the model that describes the noise enhancement in Fabry-Perot fiber interferometers [159]

$$S_{R,tpn} = \frac{4F^2}{\pi^2} S_{tpn} \tag{6.51}$$

where F is the finesse of the ring resonator. If we combine Eq. 6.48, 6.50 and Eq. 6.51 we can show in Fig. 6.25 numerical simulations regarding the amount of thermorefractive variations produced in the ring resonator and the effect of the Sagnac filter on the phase noise.

At the end, whether we use Eq.6.51 or we addapt recent results of [160], where an experimental investigation of thermorefractive noise has been conducted on a similarly structured ring resonator, we can conclude that Sagnac loop cleans out the spurious phase noise at measured frequencies with more than 50 dB, resulting with an unwanted noise contribution far below the shot noise.

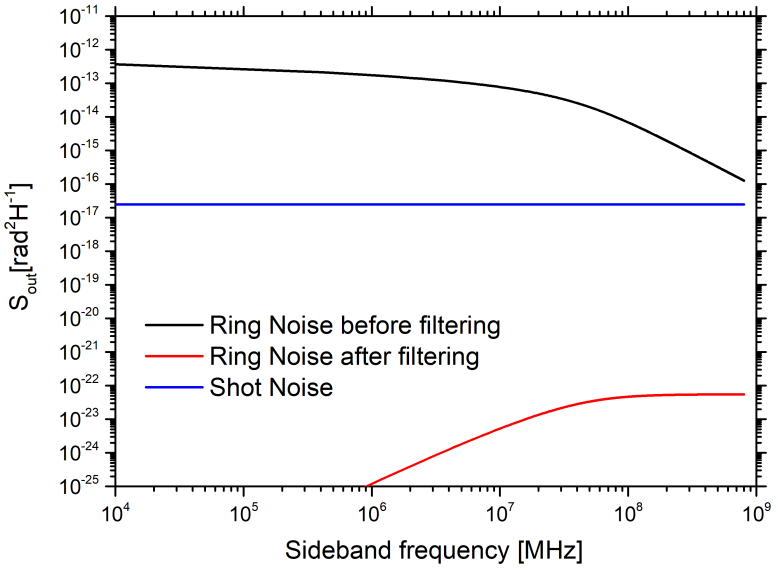

Figure 6.25: Thermorefractive noise of a source located at position x inside the Sagnac interferometer before and after filtering compared with phase shot noise calculated for 52 mW.

Physical property	Value	Units
Thermo-optic coefficient (dn/dT)	2.45 $\times 10^{-5}$	K^{-1}
Effective index (n_{eff})	1.74	
Linear expansion coefficient (α_L)	1 $\times 10^{-6}$	K^{-1}
Temperature (T)	298.15	K
Boltzmann constant (k_b)	1.38 $\times 10^{-23}$	J K^{-1}
Sagnac length (L)	2572 $\times 10^{-6}$	m
Position of the ring resonator (x)	1207 $\times 10^{-6}$	m
Wavelength (λ_p)	1550 $\times 10^{-9}$	m
k_{max}	5.847 $\times 10^{6}$	m^{-1}
k_{min}	3.848 $\times 10^{4}$	m^{-1}
refractive index (n)	1.996	
Radius of the ring resonator (R)	30 $\times 10^{-6}$	m
Thermal conductivity (κ)	30	W m^{-1} K^{-1}
Finesse (F)	960	

Table 6.1: Values and definitions of physical properties used to calculate the amount of thermorefractive phase noise in the waveguide and in the ring resonator

6.4.3.3 Discussion on noise contribution in the measurement results of SQ and ASQ variance

Finally, we discuss the evolution of possible sources of amplitude and phase noises which contribute to the final results shown in Fig. 6.18(b) - 6.19(a). We focus on two cases of noise generation when the pump beam is ON and OFF resonance from the micro ring resonator.

OFF resonant

During the propagation of the light in the waveguide the classical noise produced by thermorefractive effect is coupled to the phase of the pump beam. The beam is then split by a 50/50 beam splitter that correlates the laser noise of the two beams. When the counter-propagating beams propagate in the waveguide, the phase noise is further increased by thermal effects. As the technical noise of the laser and the thermorefractive fluctuations are correlated in both counter propagating beams, the Sagnac interferometer removes the phase variations leaving a noise free output port. On the other hand, the amplitude noise is reduced by the rejection of the Sagnac independent on the sideband frequency [153], [161]. Afterwards, the low power signal beam propagates in a short waveguide section. Consequently, we assume that at the same time there is a co-propagating LO with the signal beam. As the noise contributions on both beams are spatially correlated, they are removed by the common mode rejection of the balanced homodyne measurement. We confirm this statement by performing a homodyne measurement of weak coherent state being off resonant with the cavity. By changing the phase of the LO we do not observe any change in the measured spectrum and therefore we can conclude that the generated, off resonant noise contributions in the waveguide are not affecting our results.

ON resonant

In case when the two counter propagating beams are resonantly coupled to the cavity, the thermorefractive phase noise increases in each arm due to the enhancement of the ring resonator, as was shown with Eq. 6.51. On top of that, due to finite tuning capabilities of the laser frequency, a slight detuning from the resonance causes the squeezed ellipse to rotate around its axis resulting to phase to amplitude noise transfer [162], [163], [164]. We confirm this statement with additional measurements shown in Fig. 6.26 where we observe the quadratic signature of the thermorefractive variations appearing in both quadratures. Since we concluded (Fig. 6.25) that any spurious noises are eliminated in the Sagnac, it is intriguing to observe the thermorefractive effect in the phase variance. We believe that the two counter propagating beams, when coupled to the resonator

become phase modulated and pick up a global phase shift that interferes with the LO as a relative phase. In such case the correlated noise is not rejected by the frequency dependent Sagnac filter rather than the frequency independent amplitude rejection of the loop. In Fig. 6.27 we calculate the amount of temperature noise that we should observe in the measurement considering a 23dB of amplitude rejection of our Sagnac loop. Consequently, the shape and amount of noise does resemble the observed data from Fig 6.18 (b) and therefore provides a supporting argument towards improving the amplitude rejection of the Sagnac in order to minimize the amount of noise generation. To conclude, we are convinced that in order to improve the reduction of either technical or chip based noises and observe squeezing at shorter sideband frequencies we need to increase the extinction ratio of the interferometer. Moreover, we should also perform the experiment at low temperatures to drastically decrease any temperature depended sources of phase noise.

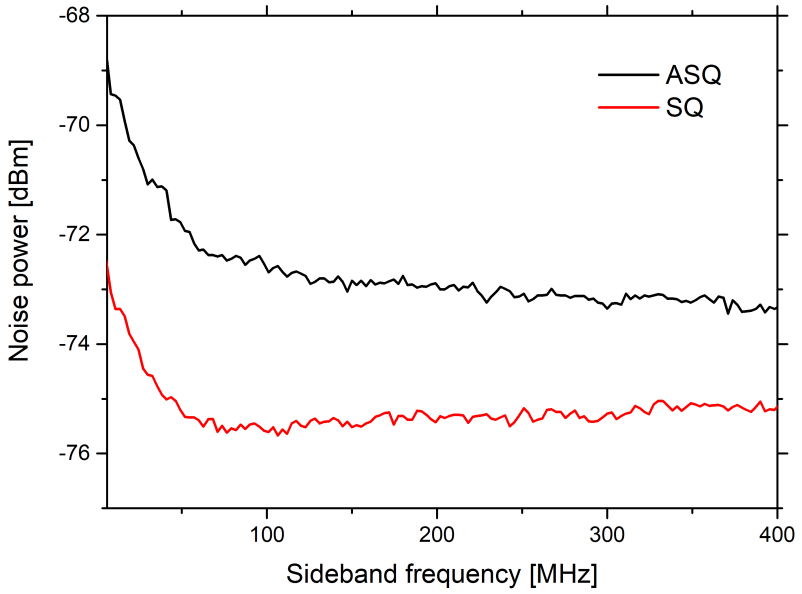

Figure 6.26: Additional raw measurement of the SQ and ASQ spectrum confirming the appearance of the thermorefractive noise in both quadratures. The pump beam is detuned from the resonance by 1 pm which is also the smallest tuning unit used during all measurements.

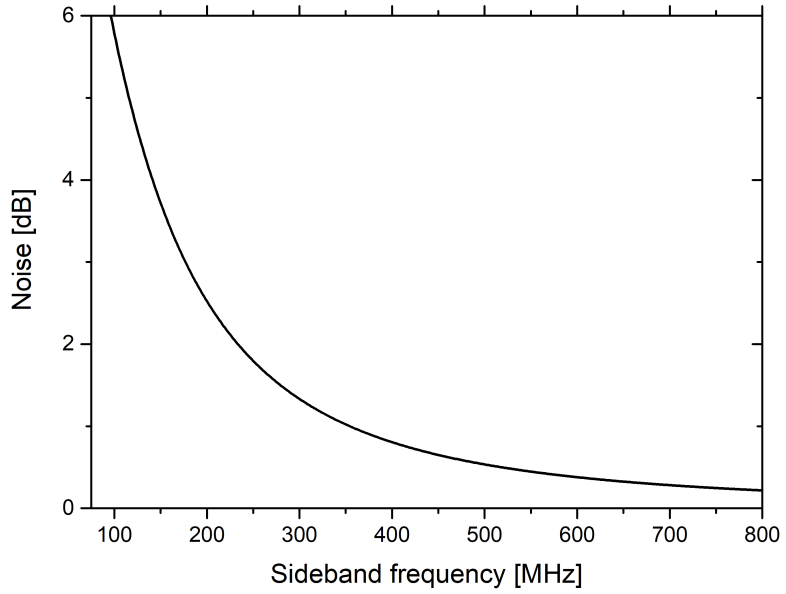

Figure 6.27: Shot noise normalized thermorefractive uctuations. The calculations consider the amplitude rejection of 23dB of the Sagnac interferemoter and shot noise value for 52 mW. For high frequencies the noise converges to shot noise level.

6.4.3.4 Calculation of broadband quadrature squeezing from a Sagnac interferometer

At this point, we estimate the amount of noise reduction we should observe in our measurement. Thus, we evaluate the level of squeezing generated via a single pass interaction of a coherent state in a nonresonant nonlinear medium and compare the results with calculations obtained in model described [150]. In that case, we retrieve the scaling factor between the squeezing parameters from both theories which we can apply to Hoffs model. The Hamiltonian describing the nonlinear interaction of a propagating field in the Kerr medium

$$\hat{H} = \frac{\zeta}{2} \int \hat{a}^{\dagger}(z,t)\hat{a}^{\dagger}(z,t)\hat{a}(z,t)\hat{a}(z,t)dt \tag{6.52}$$

has a solution already written in [150]

$$\hat{a}(L,t) = e^{i\zeta L\hat{a}^{\dagger}(0,t)\hat{a}(0,t)}\hat{a}(0,t). \tag{6.53}$$

We rewrite the amplitude operator as a linear sum of a large mean field β and small vacuum fluctuations $\hat{b}$

$$\hat{a} = \beta + \hat{b} \tag{6.54}$$

We then insert Eq. 6.54 to the solution of the propagation Eq. 6.53 to get

$$\hat{a} \approx e^{i\zeta\left(|\beta|^2+\beta\hat{b}^\dagger+\beta^*\hat{b}\right)}(\beta+\hat{b}), \tag{6.55}$$

where we redefined the Kerr interaction to include the length L and assumed that $\zeta^2|\beta|^2\langle\hat{b}\hat{b}^\dagger\rangle \ll 1$. Linearising and rearranging Eq. 6.55 yields to

$$\hat{a} \approx e^{i\zeta|\beta|^2}\left[(1+i\zeta|\beta|^2)\hat{b}+(i\zeta\beta^2)\hat{b}^\dagger+\beta\right]. \tag{6.56}$$

By defining coefficients

$$\mu = 1+i\zeta|\beta|^2 \tag{6.57}$$

and

$$\nu = i\zeta\beta^2 \tag{6.58}$$

we obtain a formula for amplitude squeezing as in [152]

$$\hat{a} \approx e^{i\zeta|\beta|^2}\left[\left(\mu\hat{b}+\nu\hat{b}^\dagger\right)+\beta\right]. \tag{6.59}$$

Now we can compare the Eq. 6.57-6.59 with Eq. 3.4 - 3.6 of [150] to conclude that the degree of squeezing between the squeezed coherent state obtained from a single pass through a nonlinear medium and a squeezed vacuum from Sagnac interferometer scales with a factor of 2. Using this information we rewrite Eq. 6.22 and calculate the amount of squeezing at the measured sideband frequency to obtain results shown in Fig.6.28. Under the assumption that the measurement at high frequencies is not limited with thermorefractive noise, the model describes the amount of observed squeezing reasonably well.

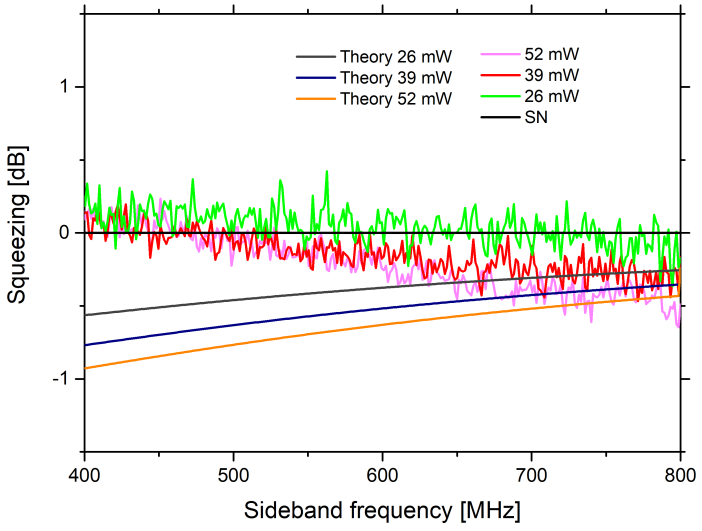

Figure 6.28: Theory vs Experiment regarding the measurement of broadband quadrature squeezing. The numerical calculations are performed considering 0.32 dB/cm propagation loss, escape efficiency of 77%, interaction strength of 4.7 and total outcoupling losses of 3.25 dB.

Finally, we investigate whether its possible to produce sufficient amount of squeezing using self phase modulation on a SiN photonic chip, to achieve fault tolerance. Combining Hoffs model and our premise for SV generation we calculate the squeezing levels in already fabricated waveguide and ring resonator structures that use commercially available ultra low loss LPCVD SiN [6] and the best known results in LPCVD SiN ring resonators [7] with an intrinsic Q-factor of 13 and 37 million, respectively. The most striking result of Fig. 6.29 is the small amount of power (40 mW) necessary to obtain -13 dB of squeezing. Such noise reduction is considered to be well below the treshold to achieve FTUQC and introduces a wide variety of future applications for CV encoding.

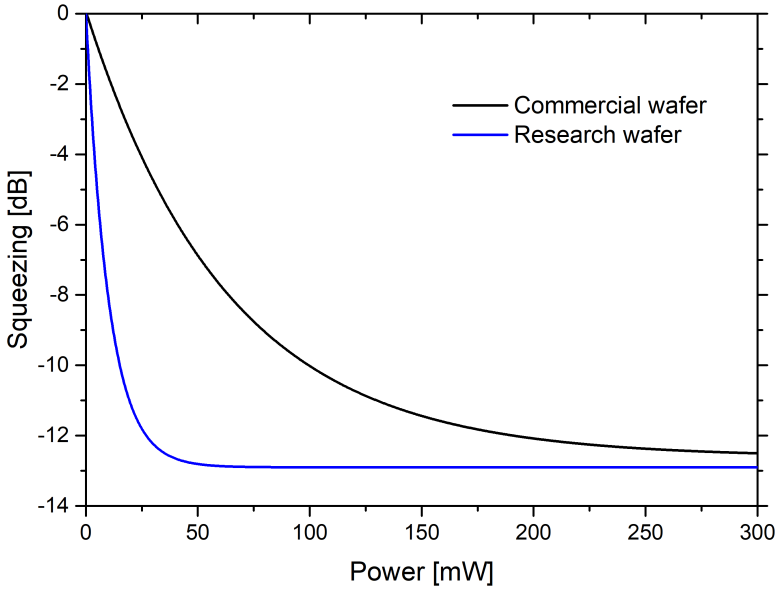

Figure 6.29: Theoreticaly predicted levels of SV for commercially available LPCVD SiN from [6] and LPCVD SiN from [7] which has been fabricated by a research group using same waveguide and ring dimensions as are reported in the respective references. Our fabrication process was able to produce a ring resonator with an escape efficiency of 95%, therefore we assume the same outcoupling condition for the calculations presented here.

6.5 Conclusion and future work

In conclusion, we studied on chip generation of broadband quadrature squeezing on a SiN photonic fabricated. Our inferred results of -1 dB are comparable to the on chip squeezing based on PPLN waveguides [48], [77], [165]. But contrary to the alternative PPLN sources which are several mm long and fabricated via proton beam lithography, our process takes full advantage of the standard commercial nanofabrication techniques

providing a truly scalable process. We are convinced that the amount of squeezing is limited by the thermorefractive noise that affects all materials. It is strongly believed that the temperature fluctuations can be heavily reduced by either operating at cryogenic temperatures or increasing the performance of the Sagnac interferometer. Such experimental changes would result in increasing the amount of observable squeezing using current sample pumped under same conditions. We also investigated a possible change in material to ultra low loss LPCVD SiN that would result in much higher amount of generated squeezing of -13 dB using only 40 mW of pumping power. Such source of high levels of shot noise reduction integrated on a photonic chip is highly attractive as it provides sufficient conditions for FTUQC.

Chapter 7

Conclusion and Outlook

It is truly astonishing to think that it has been 60 years ago when Richard Feynman gave his famous lecture **"There's Plenty of Room at the Bottom"** and discussed the potential of this exciting field of nanotechnology. Nowadays, it forms an irreplaceable part of many technological fields regarding quantum computation, sensing and communication.

In this thesis we mainly focused on its computational part, where we discussed pros and cons of several promising, scalable technologies ranging from superconducting circuits, semiconductor quantum dots up to photonic quantum technologies for faul tolerant universal quantum computer. Specifically photonics, holds a true potential to build a secure network of computers and establish the much desired idea of quantum internet. We presented several results concerning a source of generating more than milion pairs of correlated photons on a photonic chip in the visible region that can be merged with integrated SPAD technology to be potentially commercialized as one of the first devices as a small scale quantum simulator working at room temperature. As we further argue, scaling up photonic computers based on single photon sources can be highly challenging from both the engineering and computational perspective. On the other hand continuous variables can be hybridized with discrete systems to harness the advantage of both types of encoding with less practical challenges. We studied generation of broadband quadrature squeezing in a SiN photonic chip, fabricated with standard lithography techniques and measure 0.45 dB of shot noise reduction spanning over 300 MHz. Moving towards ultra low loss LPCVD SiN operating at low temperatures should produce squeezing up to -13 dB with only 40 mW of power. Such source forms the basis of error friendly DV-CV encoding and integrating it on a microchip opens up new routes for scalable quantum computation technology.

In the introduction of previous chapter we mentioned the necessity to prepare high quality Cat states in order to build a FTUQC on a photonic chip. The basic ingredients to generate a Cat state in an optical domain are sources of quadrature squeezed

of light, highly transparent beam splitters and efficient photon number resolving detectors. Thankfully, all this components can be integrated on a SiN photonic chip with high quality, making this material platform very attractive for CV QIP. In Fig. 7.1 we provide a schematic representation of a photonic circuit that is possible to produce and measure Cat states under cryogenic temperatures. Such future work will be realized with our collaborators in Rome with whom we developed an efficient single wire readout electronics for multiple SSPD's [67]. As the experiment will be performed under low temperatures, the spourious thermorefractive noise will be highly reduced but at the same time thermal heaters can not be used to provide a sufficient tuning capabilities to integrate Mach-Zenhder (MZ) type of a variable beam splitter [166]. For that reason we need to consider mechanical tuning via electrostatic MEMS structures that can be integrated with standart lithography techniques [167]. In order to avoid outcoupling losses from the chip, possible integration of highly efficient Germanium homodyne detectors [139] will be taken into consideration. Overall, we can imagine to cascade the design of Fig. 7.1 to produce on chip entanglement, teleportation or cluster state generation, making a broad variations of experimental proposals concerning the results obtained in this thesis.

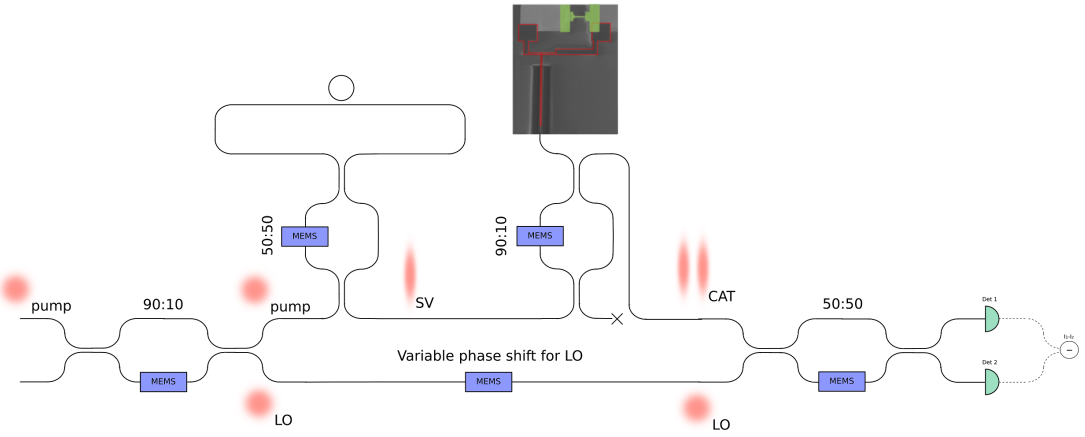

Figure 7.1: Schematic visualization of a photonic circuit to generate and measure Schrodinger Cat state on a chip.

References

[1] M. Nielsen and I. Chuang. *"Quantum computation and quantum information"*. Cambridge University Press, 2010.

[2] B. Lekitsch, S. Weidt, A.G Fowler, K. Molmer, S.J Devitt, Ch. Wunderlich, and W.K Hensinger. "Blueprint for a microwave trapped ion quantum computer ". *Science Advances*, 3(2):e1601540, February 2017.

[3] C. Neill, P. Roushan, K. Kechedzhi, S. Boixo, S.V Isakov, Smelyanskiy V., A. Megrant, B. Chiaro, A. Dunsworth, K. Arya, R. Barends, B. Burkett, Y. Chen, Z. Chen, A. Fowler, B. Foxen, M. Giustina, R. Graff, E. Jeffrey, T. Huang, J. Kelly, P. Klimov, E. Lucero, J. Mutus, Neeley M., C. Quintana, D. Sank, A. Vainsencher, J. Wenner, T.C. White, H. Neven, and J.M. Martinis. "A blueprint for demonstrating quantum supremacy with superconducting qubits". *Science*, 360(6385):195–199, April 2018.

[4] Semiconductor quantum dot technology. https://qutech.nl/vandersypen-lab/vandersypen-lab-research-overview/. Accessed: 2019.

[5] Fiber absortion CISCO. http://www.cisco.com/c/en/us/td/docs/optical/15000r7_0/dwdm/planning/guide/70epg/d7ovw.html. Accessed: 2017-07-29.

[6] Y. Xuan, Y. Liu, L.T Varghese, A.J. Metcalf, X. Xue, P.-H. Wang, K. Han, J.A. Jaramillo-Villegas, A.A. Noman, C. Wang, S. Kim, M. Teng, Y.J. Lee, B. Niu, L. Fan, J. Wang, D.E. Leaird, A.M Weiner, and M. Qi. "High-Q silicon nitride microresonators exhibiting low-power frequency comb initiation ". *Optica*, 3(11):1171–1180, October 2016.

[7] X. Ji, F.A.S Barbosa, S.P. Roberts, A. Dutt, J. Cardenas, Y. Okawachi, A. Bryant, A.L. Gaeta, and M. Lipson. "Ultra-low-loss on-chip resonators with sub-milliwatt parametric oscillation threshold ". *Optica*, 4(6):619–624, June 2017.

[8] R. Cernansky, F. Martini, and A. Politi. "Complementary metal-oxide semiconductor compatible source of single photons at near-visible wavelengths". *Optics Letters*, 43(4):855–858, February 2018.

[9] G. Moore. "Cramming more components onto integrated circuits". *Electronics*, 38(4):56–59, April 1965.

[10] D. DiVincenzo. "The Physical Implementation of Quantum Computation". *Fortschr. Phys.*, 48(9–11):771–783, 2000.

[11] J.I. Cirac and P. Zoller. "Quantum Computations with Cold Trapped Ions". *Physical Review Letters*, 74(20):4091–4094, May 1995.

[12] F. Schmidt-Kaler, H. Haffner, M. Riebe, S. Gulde, G. Lancaste, Ch. Deuschle, T. Becher, Ch. Roos, J. Eschner, and R. Blatt. "Realization of the CiracZoller controlled-NOT quantum gate". *Nature*, 422:408–411, March 2003.

[13] C. Monroe, D.M. Meekhof, B.E. King, W.M. Itano, and D.J. Wineland. "Demonstration of a Fundamental Quantum Logic Gate ". *Physical Review Letters*, 75(4714):4714–4717, December 1995.

[14] T.P. Harty, D.T.C. Allcock, C.J. Ballance, L. Guidoni, H.A Janacek, N.M. Linke, D.N. Stacey, and Lucas D.M. "High-Fidelity Preparation, Gates, Memory, and Readout of a Trapped-Ion Quantum Bit". *Physical Review Letters*, 113(220501):220501, November 2014.

[15] F. Mintert and Ch. Wunderlich. "Ion-Trap Quantum Logic Using Long-Wavelength Radiation ". *Physical Review Letters*, 87(257904):257904, November 2001.

[16] S. Aaronson and A. Arkhipov. "the computational complexity of linear optics ". *Proceedings of the forty-third annual ACM symposium on Theory of computing*, 8:333–342, June 2011.

[17] R. Barends, A. Kelly, J. Megrant, D. Sank, E. Jeffrey, Y. Chen, Y. Yin, B. Chiaro, J. Mutus, C. Neill, P. OMalley, P. Roushan, J. Wenner, T.C. White, A.N. Cleland, and J.M. Martinis. "Coherent Josephson Qubit Suitable for Scalable Quantum Integrated Circuits ". *Physical Review Letters*, 111(080502):080502, 2013.

[18] L. Casparis, T.W. Larsen, M.S. Olsen, F. Kuemmeth, P. Krogstrup, J Nygard, K.D. Petersson, and C.M. Marcus. "Gatemon Benchmarking and Two-Qubit Operation". *Physical Review Letters*, 116(150505):150505, 2016.

[19] A.G. Fowler, M. Mariantoni, J.M. Martinis, and A.N. Cleland. " surface codes: Towards practical large scale quantum computation ". *Physical Review A*, 86(3):032324, September 2012.

[20] P. Kurpiers, P. Magnard, T. Walter, B. Royer, M. Pechal, J. Heinsoo, Y. Salath, A. Akin, S. Storz, J.C. Besse, S. Gasparinetti, Blais A., and A. Wallraff. "Deterministic quantum state transfer and remote entanglement using microwave photons". *Nature*, 558:264–267, June 2018.

[21] J.M. Elzerman, R. Hanson, L.H Willems van Beveren, B. Witkamp, L.M.K Vandersypen, and L.P. Kouwenhoven. "Single-shot read-out of an individual electron spin in a quantum dot". *Nature*, 430:431–435, July 2004.

[22] A. Morello, J.J. Pla, F.A. Zwanenburg, K.W. Chan, K.Y. Tan, H. Huebl, M. Mottonen, Ch.D. Nugroho, Ch. Yang, J.A. van Donkelaar, A.D.C. Alves, D.N. Jamieson, Ch.C. Escott, L.C.L. Hollenberg, R.G. Clark, and A.S. Dzurak. "Single-shot readout of an electron spin in silicon". *Nature*, 467:687–691, October 2004.

[23] M Veldhorst, C.H. Yang, J.C.C. Hwang, W. Huang, J.P. Dehollain, J.T. Muhonen, S. Simmons, A. Laucht, F.E. Hudson, K.M. Itoh, A Morello, and A.S. Dzurak. "A two-qubit logic gate in silicon". *Nature*, 526:410–414, October 2015.

[24] T.F. Watson, S.G.J Philips, E. Kawakami, D.R. Ward, P. Scarlino, M. Veldhorst, D.E. Savage, M.G. Lagally, M. Friesen, S.N. Coppersmith, M.A. Eriksson, and L.M.K. Vandersypen. "A programmable two-qubit quantum processor in silicon". *Nature*, 555:633–637, March 2018.

[25] P.A. Hisket, D. Rosenberg, Peterson C.G., R.J. Hughes, S. Nam, A.E. Lita, A.J. Miller, and J.E. Nordholt. "long-distance quantum key distribution in optical fibre ". *New Journal of Physics*, 8(9):193–193, September 2006.

[26] A. Politi, M.J. Cryan, J.G. Rarity, S. Yu, and J.L. O'Brien. "Silica-on-Silicon Waveguide Quantum Circuits". *Science*, 320(5876):646–649, May 2008.

[27] E. Knill, R. Laflamme, and G.J. Milburn. "A scheme for efficient quantum computation with linear optics". *Nature*, 409:46–52, January 2001.

[28] J. O'Brien, A. Furusawa, and J. Vuckovic. "Photonic quantum technologies". *Nature Photonics*, 3:687–695, September 2009.

[29] M. Fiorentino, S.M. Spillane, R.G. Beausoleil, T.D. Roberts, P. Battle, and M.W. Munro. "Spontaneous parametric down-conversion in periodically poled KTP waveguides and bulk crystals". *Optics Express*, 15(12):7479–7488, June 2007.

[30] M. Fiorentino, P.L. Voss, J.E. Sharping, and P. Kumar. "All-Fiber Photon-Pair Source for Quantum Communications". *IEEE Photonics Technology Letters*, 14(7):983–985, July 2002.

[31] J.E. Sharping, J. Chen, X. Li, P. Kumar, and R.S. Windeler. "Quantum-correlated twin photons from microstructure fiber". *Optics Express*, 12(14):3086–3094, June 2004.

[32] J.G. Rarity, J. Fulconis, J. Duligall, W.J. Wadsworth, and P.S.T. Russell. "Photonic crystal fiber source of correlated photon pairs". *Optics Express*, 13(2):534–544, January 2005.

[33] J. Fulconis, O. Alibart, W.J. Wadsworth, P.S.T. Russell, and J.G. Rarity. "High brightness single mode source of correlated photon pairs using a photonic crystal fiber". *Optics Express*, 13(19):7572–7582, January 2005.

[34] M.J. Collins, C. Xiong, I.H. Rey, T.D. Vo, J. He, S. Shahnia, C. Reardon, T.F. T.F. Krauss, M.J. Steel, Clark A.S, and B.J. Eggleton. "Integrated spatial multiplexing of heralded single-photon sources". *Nature Communications*, 4:2582, October 2013.

[35] C. Xiong, X. Zhang, Z. Liu, M.J Collins, A. Mahendra, L.G. Helt, M.J Steel, D.-Y Choi, C.J. Chae, P.H.W Leong, and B.J. Eggleton. "Active temporal multiplexing of indistinguishable heralded single photons". *Nature Communications*, 7:10853, March 2016.

[36] O. Gazzano, S. Michaelis de Vasconcellos, C. Arnold, A. Nowak, E. Galopin, I. Sagnes, L. Lanco, A. Lematre, and P. Senellart. "Bright solid-state sources of indistinguishable single photons". *Nature Communications*, 4(1425), February 2013.

[37] M. Muller, S. Bounouar, K.D. Jons, M. Glassl, and P. Michler. "On-demand generation of indistinguishable polarization-entangled photon pairs". *Nature Photonics*, 8:224–228, February 2014.

[38] N. Somaschi, V. Giesz, L. De Santis, J.C. Loredo, M.P. Almeida, G. Hornecker, S.L. Portalupi, T. Grange, C. Anton, J. Demory, C. Gomez, I. Sagnes, N.D. Lanzillotti-Kimura, A. Lematre, A. Auffeves, A.G. White, L. Lanco, and P. Senellart. "Near-optimal single-photon sources in the solid state". *Nature Photonics*, 10:340–345, March 2016.

[39] X. Ding, Y. He, Z.-C. Duan, N. Gregersen, M.-C. Chen, S. Unsleber, S. Maier, Ch. Schneider, M. Kamp, S. Hfling, and J.-W. Lu, Ch.-Y. Pan. "On-Demand Single Photons with High Extraction Efficiency and Near-Unity Indistinguishability from a Resonantly Driven Quantum Dot in a Micropillar". *Physical Review Letters*, 116(2):020401, January 2016.

[40] M. Davanco, J. Liu, L. Sapienza, Ch.-Z. Zhang, J. Vinicius, D.M. Cardoso, V. Verma, R. Mirin, S.W. Nam, L. Liu, and K. Srinivasan. "Heterogeneous integration for on-chip quantum photonic circuits with single quantum dot devices ". *Nature Communications*, 8(889), October 2017.

[41] T. Schroder, S.L. Mouradian, J. Zheng, M.E. Trusheim, M. Walsh, E.H. Chen, L. Li, I. Bayn, and D. Englund. "Quantum nanophotonics in diamond [Invited]". *Journal of the Optical Society of America B*, 33(4):B65–B83, March 2016.

[42] I. Bayn, E.H. Chen, M.E. Trusheim, L. Li, T. Schroder, O. Gaathon, M. Lu, A. Stein, M. Liu, K. Kisslinger, H. Clevenson, and D. Englund. "Generation of

Ensembles of Individually Resolvable Nitrogen Vacancies Using Nanometer-Scale Apertures in Ultrahigh-Aspect Ratio Planar Implantation Masks". *Nano Letters*, 15(3):1751–1758, January 2015.

[43] M.W. Doherty, N.B. Manson, P. Delaney, F. Jelezko, J. Wrachtrup, and L.C.L. Hollenberg. "The nitrogen-vacancy colour centre in diamond ". *Physics Reports*, 528(1):1–45, January 2013.

[44] B. Rodiek, M. Lopez, H. Hofer, G. Porrovecchio, M. Smid, X.-L. Chu, S. Gotzinger, V. Sandoghdar, S. Lindner, Ch. Becher, and S. Kuck. "Experimental realization of an absolute single-photon source based on a single nitrogen vacancy center in a nanodiamond". *Nano Letters*, 4(1):71–76, January 2017.

[45] R.E. Sipahigil, Evans, D.D. Sukachev, M.J. Burek, J. Borregaard, M.K. Bhaskar, C.T. Nguyen, J.L. Pacheco, H.A. Atikian, C. Meuwly, R.M. Camacho, F. Jelezko, E. Bielec, H. Park, M. Loncar, and M.D. Lukin. "An integrated diamond nanophotonics platform for quantum-optical networks". *Science*, 354(6314):847–850, November 2016.

[46] J. Benedikter, H. Kaupp, T. Hummer, Y. Liang, A. Bommer, Ch. Becher, A. Krueger, J.M. Smith, T.W. Hnsch, and D. Hunger. "Cavity-Enhanced Single-Photon Source Based on the Silicon-Vacancy Center in Diamond". *Physical Review Applied*, 7(2):024031, February 2017.

[47] S. Lloyd and S.L. Braunstein. "Quantum Computation over Continuous Variables". *Physical Review Letters*, 82(8):1784–1787, February 1999.

[48] F. Kaiser, B. Fedrici, A. Zavatta, V. DAuria, and S. Tanzilli. "A fully guided-wave squeezing experiment for fiber quantum networks". *Optica*, 3(4):362–365, April 2016.

[49] R.M. Shelby, M.D. Levenson, S.H. Perlmutter, R.G. DeVoe, and D.F. Walls. "Broad-Band Parametric Deamplification of Quantum Noise in an Optical Fiber". *Physics Review Letters*, 57(6):691–694, August 1986.

[50] K. Fukui, A. Tomita, A. Okamoto, and K. Fujii. "High-Threshold Fault-Tolerant Quantum Computation with Analog Quantum Error Correction ". *Physical Review X*, 8(2):021054, May 2018.

[51] J.L. O'Brien, G.J. Pryde, A.G. White, T.C. Ralph, and D. Branning. "Demonstration of an all-optical quantum controlled-NOT gate". *Nature*, 426:264267, November 2003.

[52] S. Gasparoni, J.W. Pan, P. Walther, T. Rudolph, and A. Zeilinger. "Realization of a Photonic Controlled-NOT Gate Sufficient for Quantum Computation". *Physical Review Letters*, 93(2):020504, July 2004.

[53] A. Politi, J.C.F. Matthews, and J.L. O'Brien. "Shors Quantum Factoring Algorithm on a Photonic Chip". *Science*, 325(5945):1221, September 2009.

[54] M. Notomi, E. Kuramochi, and T. Tanabe. "Large-scale arrays of ultrahigh-Q coupled nanocavities". *Nature Photonics*, 2:741–747, November 2008.

[55] H. Sekoguchi, Y. Takahashi, T. Asano, and S. Noda. "Photonic crystal nanocavity with a Q-factor of 9 million". *Optics Express*, 22(1):916–924, January 2014.

[56] I. Fushman, D. Englund, A. Faraon, N. Stoltz, P. Petroff, and J. Vuckovic. "Controlled Phase Shifts with a Single Quantum Dot". *Science*, 320(5877):769–772, May 2008.

[57] T. Volz, A. Reinhard, M. Winger, A. Badolato, K.J. Hennessy, E.L. Hu, and A. Imamoglu. "Ultrafast all-optical switching by single photons". *Nature Photonics*, 6:605–609, August 2012.

[58] N.C. Harris, D. Grassani, A. Simbula, M. Pant, M. Galli, T. Baehr-Jones, M. Hochberg, D. Englund, D. Bajoni, and Ch. Galland. "Integrated Source of Spectrally Filtered Correlated Photons for Large-Scale Quantum Photonic Systems". *Physical Review X*, 4(4):041047, December 2014.

[59] J.E. Cunningham, I. Shubin, X. Zheng, T. Pinguet, A. Mekis, Y. Luo, H. Thacker, G. Li, J. Yao, K. Raj, and A.V. Krishnamoorthy. "Highly-efficient thermally-tuned resonant optical filters". *Optics Express*, 18(18):19055–19063, August 2010.

[60] C. Errando-Herranz, F. Niklaus, G. Stemme, and K.B. Gylfason. "Low-power microelectromechanically tunable silicon photonic ring resonator adddrop filter". *Optics Letters*, 40(15):3556–3559, August 2015.

[61] R. Spickermann, S.R. Sakamoto, M.G. Peters, and N. Dagli. "GaAs/AlGaAs travelling wave electro-optic modulator with an electrical bandwidth ¿40 GHz". *Electronics Letters*, 32(12):1095–1096, June 1996.

[62] G.-R. Lin, S.-P Su, Ch.-L. Wu, Y.-H Lin, B.-J. Huang, H.-Y. Wang, Ch.-T. Tsai, Ch.-I. Wu, and Y.-Ch. Chi. "Si-rich SiNx based Kerr switch enables optical data conversion up to 12 Gbit/s". *Scientific Reports*, 5(9611), April 2015.

[63] L. Chang, M.H.P. Pfeiffer, N. Volet, M. Zervas, J.D. Peters, C.L. Manganelli, E.J. Stanton, Y. Li, T.J. Kippenberg, and J.E. Bowers. "Heterogeneous integration of lithium niobate and silicon nitride waveguides for wafer-scale photonic integrated circuits on silicon". *Optics Letters*, 42(4):803–806, February 2017.

[64] A.N.R. Ahmed, S. Shi, M. Zablocki, P. Yao, and D.W. Prather. "Tunable hybrid silicon nitride and thin-film lithium niobate electro-optic microresonator". *Optics Letters*, 44(3):618–621, January 2019.

[65] F. Marsili, V.B. Verma, J.A. Stern, S. Harrington, A.E. Lita, T. Gerrits, I. Vayshenker, B. Baek, M.D. Shaw, R.P. Mirin, and S.W. Nam. "Detecting single infrared photons with 93 system efficiency". *Nature Photonics*, 7:210–214, February 2013.

[66] F. Villa, R. Lussana, D. Bronzi, S. Tisa, A. Tosi, F. Zappa, A.D. Mora, D. Contini, D. Durini, S. Weyers, and W. Brockherde. "CMOS Imager With 1024 SPADs and TDCs for Single-Photon Timing and 3-D Time-of-Flight". *IEEE Journal of Selected Topics in Quantum Electronics*, 20(6):3804810, July 2014.

[67] A. Gaggero, F. Martini, F. Mattioli, F. Chiarello, R. Cernansky, and R. Politi, A.and Leoni. "Amplitude-Multiplexed readout of single photon detectors based on superconducting nanowires". *arXiv:1811.12306*, November 2018.

[68] S. Bogdanov, M.Y. Shalaginov, A. Boltasseva, and V.M. Shalaev. "Material platforms for integrated quantum photonics". *Optical Materials Express*, 7(1):111–132, January 2017.

[69] C.M. Gentry, J.M. Shainline, M.T. Wade, M.J. Stevens, S.D. Dyer, X. Zeng, F. Pavanello, T. Gerrits, S.W. Nam, R.P Mirin, and M.A. Popovic. "Quantum-correlated photon pairs generated in a commercial 45nm complementary metal-oxide semiconductor microelectronic chip". *Optica*, 2(12):1065–1071, December 2015.

[70] J.W. Silverstone, D. Bonneau, K. Ohira, N. Suzuki, H. Yoshida, N. Iizuka, M. Ezaki, C.M. Natarajan, M.G. Tanner, R.H. Hadfield, V. Zwiller, G.D. Marshall, J.G. Rarity, J.L. O'Brien, and M.G. Thompson. "On-chip quantum interference between silicon photon-pair sources". *Nature Photonics*, 8:104–108, December 2013.

[71] J. Wang, S. Paesani, Y. Ding, R. Santagati, P. Skrzypczyk, A. Salavrakos, J. Tura, R. Augusiak, L. Mancinska, D. Bacco, D. Bonneau, J.W. Silverstone, Q. Gong, A. Acin, K. Rottwitt, L.K. Oxenlowe, J.L. O'Brien, A. Laing, and M.G. Thompson. "Multidimensional quantum entanglement with large-scale integrated optics". *Science*, 360(6386):285–291, April 2018.

[72] S. Azzini, D. Grassani, M.J. Strain, M. Sorel, L.G. Helt, J.E. Sipe, M. Liscidini, M. Galli, and D. Bajoni. "Ultra-low power generation of twin photons in a compact silicon ring resonator". *Optics Express*, 20(21):23100–23107, August 2012.

[73] S.F. Preble, M.L. Fanto, J.A. Steidle, Ch.C. Tison, G.A. Howland, Z. Wang, and P. M. Alsing. "On-Chip Quantum Interference from a Single Silicon Ring-Resonator Source". *Science*, 4(2):021001, August 2015.

[74] E. Engin, D. Bonneau, Ch. M. Natarajan, A.S. Clark, M.G. Tanner, R.H. Hadfield, S.N. Dorenbos, V. Zwiller, K. Ohira, N. Suzuki, H. Yoshida, N. Iizuka, M. Ezaki,

J.L. OBrien, and M.G. Thompson. "Photon pair generation in a silicon micro-ring resonator with reverse bias enhancement". *Optics Express*, 21(23):27826–27834, August 2013.

[75] M. Zhang, Ch. Wang, R. Cheng, A. Shams-Ansari, and M. Loncar. "Monolithic ultra-high-Q lithium niobate microring resonator". *Optica*, 4(12):1536–1537, December 2017.

[76] H. Jin, F.M. Liu, P. Xu, J.L. Xia, M.L. Zhong, Y. Yuan, J.W. Zhou, Y.X. Gong, W. Wang, and S.N. Zhu. "On-Chip Generation and Manipulation of Entangled Photons Based on Reconfigurable Lithium-Niobate Waveguide Circuits". *Physical Review Letters*, 113(10):103601, September 2014.

[77] F. Lenzini, J. Janousek, O. Thearle, M. Villa, B. Haylock, S. Kasture, L. Cui, H.-P. Phan, D.V. Dao, H. Yonezawa, P.K. Lam, E.H. Huntington, and M. Lobino. "Integrated photonic platform for quantum information with continuous variables". *Science Advances*, 4(12):eaat9331, December 2018.

[78] D.J. Moss, R. Morandotti, A.L. Gaeta, and M. Lipson. "New CMOS-compatible platforms based on silicon nitride and Hydex for nonlinear optics". *Nature Photonics*, 7:597–607, July 2013.

[79] Ch. Reimer, M. Kues, P. Roztocki, B. Wetzel, F. Grazio, B.E. Little, S.T. Chu, T. Johnston, Y. Bromberg, L. Caspani, D. J. Moss, and R. Morandotti. "Generation of multiphoton entangled quantum states by means of integrated frequency combs". *Science*, 351(6278):1176–1180, March 2016.

[80] A.M. Childs, D. Maslov, Y. Nam, N.J. Ross, and Y. Su. "toward the first quantum simulation with quantum speedup ". *PNAS*, 115(38):9456–9461, September 2018.

[81] R. Feyman. "Simulating physics with computers.". *Int. J. Theor. Phys.*, 21(467–488), 1982.

[82] S. Somaroo, C.H. Tseng, T.H. Havel, R. Laamme, and D.G. Cory. "Quantum simulations on a quantum computer". *Physical Review Letters*, 82(26):5381, June 1999.

[83] S. Lloyd. "Almost any quantum logic gate is universal". *Physical Review Letters*, 75(2):346–349, June 1995.

[84] J. Kempe. "Quantum random walks: An introductory overview". *Contemporary Physics*, 44(4):307–327, August 2003.

[85] E. Fahri and S. Gutmann. "Quantum computation and decision trees". *Physical Review A*, 58(2):915–928, August 1998.

[86] A. Childs, E. Fahri, and S. Gutmann. "An example of the difference between quantum and classical random walks". *Quantum Information Processing*, 1(1–2):35–43, April 2002.

[87] F. Zahringer, G. Kirchmair, R. Gerritsma, E. Solano, R. Blatt, and C.F. Roos. "Realization of a quantum walk with one and two trapped ions". *Physical Review Letters*, 104(10):100503, March 2010.

[88] E. Flurin, V. Ramasesh, S. Hacohen-Gourgy, L.S. Martin, N.Y. Yao, and I. Siddiqi. "Observing topological invariants using quantum walk in superconducting circuits". *Physical Review X*, 7(3):031023, August 2017.

[89] J. Du, H. Li, X. Xu, M. Shi, J. Wu, X. Zhou, and R. Han. "Experimental implementation of the quantum random-walk algorithm". *Physical Review A*, 67(4):042316, April 2003.

[90] A. Melnikov and L.E. Fedichkin. "Quantum walks of interacting fermions on a cycle graph". *Scientific Reports*, 6(34226), September 2016.

[91] P.M. Preiss, R. Ma, M. Eric Tai, A. Lukin, M. Rispoli, P. Zupancic, Y. Lahini, R. Islam, and M. Greiner. "Strongly correlated quantum walks in optical lattices". *Science*, 347(6227):1229–1233, March 2015.

[92] P. Knight, E. Roldan, and J.E. Sipe. "Quantum walk on the line as an interference phenomenon". *Physical Review A*, 68(2):020301, August 2003.

[93] Y. Omar, N. Paunkovic, L. Sheridan, and S. Bose. "Quantum walk on a line with two entangled particles". *Physical Review A*, 74(4):042304, October 2006.

[94] A. Perruzzo, M. Lobino, J.C.F. Matthews, N. Matsuda, A. Politi, K. Poulios, X.-Q. Zhou, Y. Lahini, N. Ismail, K. Worhoff, Y. Bromberg, Y. Silberberg, M.J. Thompson, and J.L. O'Brien. "Quantum walks of correlated photons". *Science*, 329(5998):1500–1503, September 2010.

[95] J.C.F. Matthews, K. Poulios, J.D.A. Meinecke, A. Politi, A. Peruzzo, N. Ismail, M.G. K. Worhoff, Thompson, and J.L. O'rien. "Observing fermionic statistics with photons in arbitrary processes". *Scientific Reports*, 3(1539), March 2013.

[96] L. Sansoni, F. Sciarrino, G. Vallone, P. Mataloni, A. Crespi, R. Ramponi, and R. Osellame. "Two-particle bosonic-fermionic quantum walk via integrated photonics". *Physical Review Letters*, 108(1):010502, January 2012.

[97] D.N. Biggerstaff, R. Heilmann, A.A. Zecevik, M. Grafe, M.A. Broome, A. Fedrizzi, S. Nolte, A. Szameit, A.G. White, and I. Kassal. "Enhancing coherent transport in a photonic network using controllable decoherence". *Nature communications*, 7(11282), April 2016.

[98] F. Caruso, A. Crespi, A.G. Ciriolo, F. Sciarrino, and R. Osellame. "Fast escape of a quantum walker from an integrated photonic maze". *Nature communications*, 7(11682), June 2016.

[99] A. Crespi, R. Osellame, R. Ramponi, V. Giovannetti, R. Fazio, L. Sansoni, F. De Nicola, F. Sciarrino, and P. Mataloni. "Anderson localization of entangled photons in an integrated quantum walk". *Nature Photonics*, 7:322–328, March 2013.

[100] K. Poulios, R. Keil, D. Fry, J.D.A. Meinecke, J.C.F. Matthews, A. Politi, M. Lobino, M. Grafe, M. Heinrich, S. Nolte, A. Szameit, and J.L. O'Brien. "Quantum walks of correlated photon pairs in two-dimensional waveguide arrays". *Physical Review Letters*, 112(14):143604, April 2014.

[101] N. Daldosso, M. Melchiorri, F. Riboli, F. Sbrana, L. Pavesi, G. Pucker, C. Kompocholis, M. Crivellari, P. Bellutti, and A. Lui. "Fabrication and optical characterization of thin two-dimensional Si3N4 waveguides". *Materials Science in Semiconductor Processing*, 7(4–6):453–458, October 2004.

[102] A.Z. Subramanian, P. Neutens, A. Dhakal, R. Jansen, T. Claes, X. Rottenberg, F. Peyskens, S. Selvaraja, P. Helin, B. Du Bois, K. Leyssens, S. Severi, P. Deshpande, R. Baets, and P. Van Dorpe. "Low-loss Singlemode PECVD silicon nitride photonic wire waveguides for 532-900 nm wavelength window fabricated within a CMOS pilot line". *IEEE Photonics Journal*, 5(6):2202809, December 2013.

[103] A. Gorin, A. Jaouad, E. Grondin, V. Aimez, and P. Charette. "Fabrication of silicon nitride waveguides for visible-light using PECVD: a study of the effect of plasma frequency on optical properties". *Optics Express*, 16(18):13509–13516, August 2008.

[104] Sin etching recipe in icp rie ucsb. https://www.nanotech.ucsb.edu/wiki/images/0/06/Panasonic2-ICP-Plasma-Etch-SiN-nanoscale-rev1.pdf. Accessed: 2019.

[105] A. Yariv. "Photonics". *Oxford University Press*, October 2009.

[106] V.R. Almeida, R.R. Panepucci, and M. Lipson. "Nanotaper for compact mode conversion". *Optics Letters*, 28(15):1302–1304, August 2003.

[107] D. Taillaert, P. Bienstman, and R. Baets. "Compact efficient broadband grating coupler for silicon-on-insulator waveguides". *Optics Letters*, 29(23):2749–2751, October 2004.

[108] Ch.R. Doerr, L. Chen, Y.-K. Chen, and L.L. Buhl. "Wide bandwidth silicon nitride grating coupler". *IEEE Photonics Technology Letters*, 22(19):1461–1463, October 2010.

[109] A.Z. Subramanian, S. Selvaraja, P. Verheyen, A. Dhakal, K. Komorowska, and R. Baets. "Near-infrared grating couplers for silicon nitride photonic wires". *IEEE Photonics Technology Letters*, 24(19):1700–1703, October 2012.

[110] A. Yariv. "Universal relations for coupling of optical power between microresonators and dielectric waveguides". *Electronics Letters*, 34(4):321–322, February 2000.

[111] P. Rabiei, W.H. Steier, Ch. Zhang, and L.R. Dalton. "Polymer micro-ring filters and modulators". *Journal of Lightwave Technology*, 20(11):1968–1975, November 2002.

[112] J.K.S. Poon, J. Scheuer, S. Mookherjea, G.T. Paloczi, Y. Huang, and A. Yariv. "Matrix analysis of microring coupled-resonator optical waveguides". *Optics Express*, 12(1):90–103, January 2004.

[113] J.E. Sharping, K.M. Lee, M.A. Foster, A.M. Turner, B.S. Schmidt, M. Lipson, A.L. Gaeta, and P. Kumar. "Generation of correlated photons in nanoscale silicon waveguides". *Optics Express*, 14(25):12388–12393, December 2006.

[114] H. Takesue, Y. Tokura, H. Fukuda, T. Tsuchizawa, T. Watanabe, K. Yamada, and S.-I. Itabashi. "Entanglement generation using silicon wire waveguide". *Applied Physics Letters*, 91:201108, November 2007.

[115] S. Clemmen, K. Phan Huy, W. Bogaerts, R.G. Baets, Ph. Emplit, and S. Massar. "Continuous wave photon pair generation in silicon-on-insulator waveguides and ring resonators". *Optics Express*, 17(19):16558–16570, November 2007.

[116] H. Jin, F.M. Liu, P. Xu, J.L. Xia, M.L. Zhong, Y. Yuan, J.W. Zhou, Y.X. Gong, W. Wang, and S.N. Zhu. "On-chip generation and manipulation of entangled photons based on reconfigurable lithium-niobate waveguide circuits". *Physical Review Letters*, 113(10):103601, November 2014.

[117] S. Ten. "The Optical Fiber Communications Conference and Exhibition". *(OFC)*, (1–3), March 2016.

[118] Y.R. Shen. "Principles of Nonlinear Optics". *Wiley-Interscience*, 2003.

[119] Q. Lin, O.J. Painter, and G.P. Agrawal. "Nonlinear optical phenomena in silicon waveguides: Modeling and applications". *Optics Express*, 15(25):16604–16644, December 2007.

[120] L.G. Helt, Z. Yang, M. Liscidini, and J.E. Sipe. "Spontaneous four-wave mixing in microring resonators". *Optics Letters*, 35(18):3006–3008, September 2010.

[121] F. Martini and A. Politi. "Linear integrated optics in 3C silicon carbide". *Optics Express*, 25(10):10735–10742, May 2017.

[122] C. Lacava, S. Stankovic, A.Z. Khokhar, T. Dominguez Bucio, F.Y. Gardes, G.T. Reed, D.J. Richardson, and P. Petropoulos. "Si-rich Silicon Nitride for Nonlinear Signal Processing Applications". *Scientific Reports*, 7(22), February 2017.

[123] A. Dhakal, P. Wuytens, A. Raza, N. Le Thomas, and R. Baets. "Silicon Nitride Background in Nanophotonic Waveguide Enhanced Raman Spectroscopy". *Materials*, 10(2):140, February 2017.

[124] H. Takesue and K. Inoue. "1.5-m band quantum-correlated photon pair generation in dispersion-shifted fiber: suppression of noise photons by cooling fiber". *Optics Express*, 13(20):7832–7839, October 2005.

[125] X. Zhang, Y. Zhang, Ch. Xiong, and B.J. Eggleton. "Correlated photon pair generation in low-loss double-stripe silicon nitride waveguides". *Journal of Optics*, 18(7):074016, October 2016.

[126] Ch. Reimer, L. Caspani, M. Clerici, M. Ferrera, M Kues, M. Peccianti, A. Pasquazi, L. Razzari, B.E. Little, S.T. Chu, D.J. Moss, and R. Morandotti. "Integrated frequency comb source of heralded single photons". *Optics Express*, 22(6):6535–6546, March 2014.

[127] S.L. Braunstein and P. van Loock. "Quantum information with continuous variables". *Review of Modern Physics*, 77(2):513–577, June 2005.

[128] U. Andersen, J.S Neergaard-Nielsen, P. van Loock, and A. Furusawa. "Hybrid discrete- and continuous-variable quantum information". *Nature Physics*, 11:713–719, September 2015.

[129] S. Takeda and A. Furusawa. "Optical Hybrid Quantum Information Processing". *Principles and Methods of Quantum Information Technologies*, 911:439–458, 2016.

[130] N.C. Menicucci, P. van Loock, M. Gu, Ch. Weedbrook, T.C. Ralph, and M.A. Nielsen. "Universal Quantum Computation with Continuous-Variable Cluster States". *Physical Review Letters*, 97(11):110501, September 2006.

[131] R. Raussendorf and H.J. Briegel. "A One-Way Quantum Computer". *Physical Review Letters*, 86(22):5188–5191, May 2001.

[132] R. Ukai, N. Iwata, Y. Shimokawa, A. Armstrong, S.C. Politi, J. Yoshikawa, P. van Loock, and A. Furusawa. "Demonstration of Unconditional One-Way Quantum Computations for Continuous Variables". *Physical Review Letters*, 106(24):240504, June 2011.

[133] D. Gottesman, A. Kitaev, and J. Preskill. "Encoding a qubit in an oscillator". *Physical Review A*, 64(1):012310, June 2001.

[134] N. Menicucci. "Fault-Tolerant Measurement-Based Quantum Computing with Continuous-Variable Cluster States". *Physical Review Letters*, 112(12):120504, March 2014.

[135] W. Asavanant, Y. Shiozawa, S. Yokoyama, B. Charoensombutamon, H. Emura, R.N. Alexander, S. Takeda, J.-I Yoshikawa, N.C. Menicucci, H. Yonezawa, and A. Furusawa. "time-domain multiplexed 2-dimensional cluster state: Universal quantum computing platform ". *arXiv:1903.03918*, March 2019.

[136] C. Fluhmann, T.L. Nguyen, M. Marinelli1, V. Negnevitsky, K. Mehta, and J.P. Home. "Encoding a qubit in a trapped-ion mechanical oscillator". *Nature*, 566(513-517), February 2019.

[137] H.M. Vasconcelos, L. Sanz, and S. Glancy. "All-optical generation of states for Encoding a qubit in an oscillator". *Optics Letters*, 35(19):3261–3263, October 2010.

[138] M. Eaton, R. Nehra, and O. Pfister. "gottesman-kitaev-preskill state preparation by photon catalysis ". *arXiv:1903.01925*, March 2019.

[139] D. Ahn, Ch.-y. Hong, J. Liu, W. Giziewicz, L.C. Beals, M. Kimerling, and J. Michel. "High performance, waveguide integrated Ge photodetectors". *Optics Express*, 15(7):3916–3921, April 2007.

[140] P. Marek, R. Filip, and A. Furusawa. "Deterministic implementation of weak quantum cubic nonlinearity". *Physics Review A*, 84(5):053802, November 2011.

[141] B.Q. Baragiola, G. Pantaleoni, R.N. Alexander, A. Karanjai, and N.C. Menicucci. "all-gaussian universality and fault tolerance with the gottesman-kitaev-preskill code ". *arXiv:1903.00012*, February 2019.

[142] B.W. Walshe, L.J. Mensen, B.Q. Baragiola, and N.C. Menicucci. "robust fault tolerance for continuous-variable cluster states with excess anti-squeezing ". *arXiv:1903.02162*, March 2019.

[143] S. Takeda and A. Furusawa. "Universal Quantum Computing with Measurement-Induced Continuous-Variable Gate Sequence in a Loop-Based Architecture". *Physical Review Letters*, 119(12):120504, September 2017.

[144] R.N. Alexander, S. Yokoyama, A. Furusawa, and N.C. Menicucci. "Universal quantum computation with temporal-mode bilayer square lattices". *Physical Review A*, 97(3):032302, March 2018.

[145] R. Slusher, L. Hollberg, B. Yurke, Mertz J., and J. Valley. "Observation of Squeezed States Generated by Four-Wave Mixing in an Optical Cavity". *Physics Review Letters*, 55(22):2409–2412, November 1985.

[146] S. Machida, Y. Yamamoto, and Y. Itaya. "Observation of amplitude squeezing in a constant-currentdriven semiconductor laser". *Physics Review Letters*, 58(10):1000–1003, March 1987.

[147] Kimble H.J. Wu, L.-A, J.L. Hall, and H. Wu. "Generation of Squeezed States by Parametric Down Conversion". *Physics Review Letters*, 57(20):2520–2523, November 1986.

[148] U.L. Andersen, T. Gehring, Ch. Marquardt, and G. Leuchs. "30 years of squeezed light generation". *Physica Scripta*, 91(053001):11–22, April 2016.

[149] U.B. Hoff, B.M. Nielsen, and U.L. Andersen. "Integrated source of broadband quadrature squeezed light". *Optics Express*, 23(9):12013–12036, April 2015.

[150] M. Shirasaki and H.A. Haus. "Squeezing of pulses in a nonlinear interferometer". *Journal of the Optical Society of America B*, 7(1):30–34, January 1990.

[151] . Bergman and H.A. Haus. "Squeezing in fibers with optical pulses". *Optics Letters*, 16(9):663–665, ay 1991.

[152] K. Bergman. "Quantum Noise Reduction with Pulsed Light in Optical Fibers". *PhD Thesis*, Massachusetts Institute of Technology 1994.

[153] Ralph T.C. and A.G. White. "Retrieving squeezing from classically noisy light in second-harmonic generation ". *Journal of the Optical Society of America B*, 12(5):833–839, May 1995.

[154] A. Peruzzo, A. Laing, A. Politi, T. Rudolph, and J.L. O'brien. "Multimode quantum interference of photons in multiport integrated devices". *Nature communications*, 2(224), March 2011.

[155] M.H.P. Pfeiffer, J. Liu, M. Geiselmann, and Kippenberg T.J. "Coupling Ideality of Integrated Planar High- Q Microresonators ". *Physical Review Applied*, 7(2):024026, February 2017.

[156] K.H. Wanser. *Electronics Letters, title = "Fundamental phase noise limit in optical fibres due to temperature fluctuations"*, 28(1):53–54, January 1992.

[157] N.L. Thomas, A. Dhakal, A. Raza, F. Peyskens, and R. Baets. "Impact of fundamental thermodynamic fluctuations on light propagating in photonic waveguides made of amorphous materials ". *Optica*, 5(4):328–336, March 2018.

[158] V. Annovazzi-Lodi, S. Donati, and S. Merlo. "Thermodynamic phase noise in fibre interferometers". *Optical and Quantum Electronics*, 28(1):43–49, March.

[159] G. Skolianos, H. Wen, and M.J.F. Digonnet. "Thermal phase noise in Fabry-Prot resonators and fiber Bragg gratings". *Physical Review A*, 89(3):033818, March 2014.

[160] G. Huang, E. Lucas, J. Liu, A.S. Raja, G. Lihachev, M. L. Gorodetsky, N. J. Engelsen, and T. J. Kippenberg. "Thermo-refractive noise in silicon nitride microresonators ". *arXiv:1901.07112*, January 2019.

[161] W.P. Bowen, R. Schnabel, N. Treps, H.-A. Bachor, and P.K. Lam. "Recovery of continuous wave squeezing at low frequencies ". *Journal of Optics B: Quantum and Semiclassical Optics*, 4:421–424, November 2002.

[162] T. J. Kippenberg, A. Schliesser, and M.L. Gorodetsky. "Phase noise measurement of external cavity diode lasers and implications for optomechanical sideband cooling of GHz mechanical modes". *New Journal of Physics*, 15(015019), January 2013.

[163] A.S. Villar. "The conversion of phase to amplitude fluctuations of a light beam by an optical cavity". *American Journal of Physics*, 76(10), October 2008.

[164] T.C. Zhang, J.Ph. Poizat, P. Grelu, J.F. Roch, P. Grangier, F. Marin, A. Bramati, V. Jost, M.D. Levenstone, and E. Giacobino. "Quantum noise of free-running and externallystabilized laser diodes ". *Quantum and Semiclassical Optics: Journal of the European Optical Society Part B*, 7(601–613), 1995.

[165] F. Mondain, T. Lunghi, A. Zavatta, E. Gouzien, F. Doutre, M.D. Micheli, S. Tanzilli, and V. DAuria1. "Chip-based squeezing at a telecom wavelength". *arXiv*, November 2018.

[166] C.M. Wilkes, X. Qiang, J. Wang, R. Santagati, S. Paesani, X. Zhou, D.A.B. Miller, G.D. Marshall, M.G. Thompson, and J.L. OBrien. "60 dB high-extinction auto-configured MachZehnder interferometer ". *Optics Letters*, 41(22):5318–5321, November 2016.

[167] S.M. Chakkalakkal Abdulla, L.J. Kauppinen, M. Dijkstra, M.J. de Boera, J.W. Berenschot, R.M. de Ridder, and G.J.M. Krijnen. "Mechanical tuning of optical race-track ring resonators". *Procedia Engineering*, 5:424–427, November 2010.